Title
Functional Super-Resolution Microscopy and Its Applications in Biophysics and Cell Biology

Author
Yan, Rui

Publication Date
2021

Peer reviewed|Thesis/dissertation

Functional Super-Resolution Microscopy and Its Applications in Biophysics and Cell Biology

by

Rui Yan

A dissertation submitted in partial satisfaction of the

requirements for the degree of

Doctor of Philosophy

in

Chemistry

in the

Graduate Division

of the

University of California, Berkeley

Committee in charge:

Professor Ke Xu, Chair
Professor Gerard Marriott
Professor Graham R. Fleming
Professor Phillip Geissler

Spring 2021

Abstract

Functional Super-Resolution Microscopy and Its Applications in Biophysics and Cell Biology

by

Rui Yan

Doctor of Philosophy in Chemistry

University of California, Berkeley

Professor Ke Xu, Chair

Conventional fluorescence microscopy, despite its high sensitivity, lacks resolution at a scale comparable to biomacromolecules due to the diffraction of light. Single-molecule-based super-resolution microscopy (SRM), developed in the past 15 years, has enabled researchers to visualize the structural organization of the cell at molecular resolution with high specificity. Nevertheless, the power of single-molecule measurement in resolving inter-molecular heterogeneities has not been fully explored by the SRM field. There is plenty of room for expanding the scope of SRM to access measurement domains beyond biomolecular structures, such as the heterogeneity of physicochemical properties within the cell, a conceptual framework named "functional super-resolution microscopy" (f-SRM). This dissertation describes the efforts by the author and colleagues in developing f-SRM for living cells and applying f-SRM to discover previously unknown physicochemical heterogeneities within the cell. Part I of this dissertation describes the design, development, and application of f-SRM, which has revealed novel nanoscale properties of the cell invisible to conventional SRM. Specifically, I elaborate on the experiments of fluorescence emission spectrum-encoded single-molecule measurements of chemical polarity and molecular diffusivity at nanoscale resolution. Part II concerns a fluorescence excitation-based strategy for functional imaging, which led to the unexpected discovery of a tubular ER-Golgi intermediate compartment (t-ERGIC) in transporting a specific group of soluble proteins. In-depth biochemistry and cell biology analyses elucidated the biogenesis mechanism of the t-ERGIC involving the cargo receptor.

Table of Contents

List of Figures iii

List of Tables v

Acknowledgements vi

Introduction vii

Part I: Development of Functional Super-Resolution Microscopy (f-SRM) 1

Chapter 1: Multiplexed single-molecule detection for f-SRM 2
1.1 Fluorescence readouts as functional reporters 2
1.1.1 The mechanism of molecular fluorescence 2
1.1.2 Fluorescence intensity 2
1.1.3 Emission spectrum 3
1.1.4 Excitation spectrum 4
1.1.5 Fluorescence lifetime 4
1.1.6 Fluorescence polarization and anisotropy 4
1.2 Potentials of different fluorescence readouts for single-molecule-based f-SRM 5

Chapter 2: Experimental design of spectrally resolved SMLM 7
2.1 Introduction 7
2.2 Spectrally resolved super-resolution microscopy via ultrahigh-throughput single-molecule spectroscopy 9

Chapter 3: Spectrally resolved f-SRM reveals nanoscale compositional heterogeneity in live-cell membranes 13
3.1 Introduction 13
3.2 Results and discussion 14
3.3 Conclusion 23
3.4 Materials and methods 23

Chapter 4: Single-molecule diffusivity mapping (SM*d*M): another dimension of f-SRM 25
4.1 Introduction 25
4.2 Results and discussion 27
4.3 Conclusion 31
4.4 Materials and methods 31

Chapter 5: Multiplexed f-SRM reveals hidden properties of membrane contact sites 34
5.1 Introduction 34
5.2 Results and discussion 34
5.3 Conclusion 43
5.4 Materials and methods 43

Chapter 6: Future directions for f-SRM 45
6.1 Introduction 45
6.2 Review of relevant work 46
6.3 Outlook 49

Part II: Microscopy-Driven Discovery of a Novel Trafficking Organelle 51

Chapter 7: Excitation spectral microscopy for highly multiplexed fluorescence imaging and quantitative biosensing 52
7.1 Introduction 52
7.2 Results and discussion 53
7.2.1 Frame-synchronized AOTF scanning of the excitation wavelength 53
7.2.2 Unmixing 6 fluorophores through the excitation spectrum 54
7.2.3 Fast multi-target imaging of live cells 54
7.2.4 Absolute pH imaging in live cells via unmixing and quantifying two fluorescent species 56
7.2.5 FRET imaging in live cells via resolving the excitation spectrum 58
7.2.6 Discussion 59
7.3 Conclusion 60
7.4 Materials and methods 61

Chapter 8: Microscopy-driven discovery of a novel trafficking organelle 64
8.1 Introduction 64
8.2 Results and discussion 64
8.2.1 Identification of a highly elongated tubular organelle through mislocalized DsRed2-ER-5 64
8.2.2 The t-ERGIC mediates ER-to-Golgi trafficking, and is formed through both de novo generation and fusion 67
8.2.3 Fast ER-to-Golgi trafficking via the t-ERGIC is determined by the N-termini of soluble cargoes 70
8.2.4 The biogenesis and cargo selectivity of t-ERGIC both depend on SURF4 73
8.2.5 Co-clustering of SURF4 and cargo expands the ERES for t-ERGIC biogenesis 75
8.2.6 Antagonism between SURF4 and KDEL receptors regulates the steady-state location of cargo proteins 78
8.2.7 Discussion 82
8.3 Conclusion 85
8.4 Materials and methods 85

Concluding remarks 92

References 93

List of Figures

Figure 1: Jablonski diagram of the states and transitions in fluorescence. 2
Figure 2: Solvatochromism of Nile Red 3
Figure 3: The spatial, temporal, and spectral dimensions of single-molecule fluorescence..... 9
Figure 4: Wide-field fluorescence spectroscopy for single molecules 10
Figure 5: Concurrent positional and spectral measurement of single molecules..... 11
Figure 6: Variation in single-molecule fluorescence spectra..... 12
Figure 7: SR-STORM for four-color SRM……13
Figure 8: SR-STORM/SR-PAINT with Nile Red 16
Figure 9: Nile Red-based 3D-PAINT of a live COS-7 cell. 16
Figure 10: Spectrally resolved f-SRM visualizes polarity differences between organelle and plasma membranes in live cells 17
Figure 11: Comparison of Nile Red-based SR-STORM results on live and fixed cells..... 18
Figure 12: Distribution of the measured spectral means of single Nile Red molecules at different membranes 18
Figure 13: The observed heterogeneity in cellular membrane polarity is driven by cholesterol.. 20
Figure 14: Distribution of the apparent sizes of low-polarity nanodomains in COS-7 cells..... 21
Figure 15: Functional SR-STORM examination of the low-polarity phase 22
Figure 16: CTB treated live cells 22
Figure 17: SM*d*M for single mEos3.2 FP molecules freely diffusing in the cytoplasm of live mammalian cells 28
Figure 18: SM*d*M of free mEos3.2 in the mammalian cytoplasm and correlated SMLM of the actin cytoskeleton..... 29
Figure 19: SM*d*M of free mEos3.2 in the nucleus, and correlated SMLM of DNA 30
Figure 20: BDP-TMR-alkyne for stroboscopic PAINT and SM*d*M of cellular membranes..... 35
Figure 21: Spectral properties of BDP-TMR-alkyne in different solvents..... 36
Figure 22: Concurrent 3D-SMLM and SM*d*M diffusion mapping of cellular membranes through stroboscopic PAINT of BDP-TMR-alkyne 37
Figure 23: Principal-direction SM*d*M (pSM*d*M) analysis..... 38
Figure 24: Concurrent SM*d*M and 3D-SMLM, together with fluorescent protein markers, indicate reduced membrane diffusivity at ER-PM contact sites..... 40
Figure 25: Concurrent SM*d*M and SR-SMLM of Nile Red indicate that the reduced diffusivity at ER-PM contacts is not associated with significant changes in lipid order 41
Figure 26: f-SRM explores the possibility to transcend the structural (shape) information offered by existing super-resolution methods and unveil multidimensional information of diverse intracellular functional parameters, like those shown in this diagram, with nanoscale spatial resolution and ultimate sensitivity down to single molecules 46
Figure 27: f-SRM through fluorescence intensity and lifetime detections..... 47
Figure 28: f-SRM through ratiometric color detection..... 48
Figure 29: Excitation spectral microscopy. 53
Figure 30: Fast multi-target imaging of live cells..... 55
Figure 31: Absolute pH imaging in live cells via unmixing and quantifying two fluorescent species..... 57
Figure 32: FRET imaging in live cells via resolving the excitation spectrum..... 59

Figure 33: DsRed2-ER-5 mislocalizes to an extremely slender, Rab1-positive tubular organelle 65
Figure 34: Localization of DsRed2-ER-5 compared to various organelle markers..... 66
Figure 35: DsRed2-ER-5 TOs are labeled by Rab1A/B and exist between the ER and the Golgi 67
Figure 36: The t-ERGIC mediates ER-to-Golgi trafficking, and is formed through both de novo generation and fusion 68
Figure 37: Design of SBP-DsRed2-ER-5 for RUSH and single-particle tracking in RUSH 69
Figure 38: Dynamics of t-ERGIC for ER-to-Golgi trafficking 70
Figure 39: The N-terminus of the cargo determines its transport with the t-ERGIC and ER-to-Golgi trafficking efficiency..... 71
Figure 40: The N-terminus rule of ER-to-Golgi transport by t-ERGIC applies to different cargoes 73
Figure 41: SURF4 recognizes the N-terminus of the cargo and enables t-ERGIC formation for expedited ER-to-Golgi trafficking 74
Figure 42: The efficacy of SURF4 siRNA treatment 75
Figure 43: SURF4 co-clusters with its cargo to expand the ERES..... 76
Figure 44: ERES expansion diminishes with SURF4 siRNA 77
Figure 45: SURF4 and its cargo condensates on the ER membrane. 78
Figure 46: Distinct steady-state localizations of different FP-ER-5 constructs..... 79
Figure 47: Distinct behavior of APV-DsRed2-mEmerald-ER-5 and APV-mEmerald-DsRed2-ER-5 80
Figure 48: C-terminal extension of KDEL enhances ER retrieval 81
Figure 49: C-terminal truncation of APV-EGFP-ER-5 reduces ER retrieval..... 81
Figure 50: Enhanced ER retrieval is independent of t-ERGIC biogenesis 82
Figure 51: Overexpression of SURF4 overrides KDEL-mediated ER retrieval..... 82
Figure 52: SURF4-mediated t-ERGIC transport leads to differential protein trafficking rates and steady-state localizations 83
Figure 53: Calumenin localizes to the t-ERGIC 85

List of Tables

Table 1: Summary of different fluorescence readouts for f-SRM 7
Table 2: Spectroscopic approaches for SMLM 11

Acknowledgements

Throughout my PhD program, I have received a lot of support, help, and encouragement from many people, to whom I would like to express my sincere gratitude. Firstly, my heartfelt thanks go out to my advisor Prof. Ke Xu, who taught me the basic skills for scientific research. His curiosity to the unknowns and elegant approaches to science inspired me to choose a research career. He never hesitates to offer support and advice to me when I encounter difficulties in research as well as in life.

I am also deeply grateful for my former and current colleagues in the group, without whom I could not have achieved as much as I have now. I appreciate the help from Dr. Wan Li, Dr. Meghan Hauser, Dr. Sam Kenny, Dr. Seonah Moon, Dr. Limin Xiang, Dr. Kun Chen, and Dr. Jeongmin Kim in a lot of the projects I participated in. I also enjoy the sparking discussions on science with Bowen Wang, Ha Park, and Alex Choi. Former undergraduate student trainees, Yennie Shyu, Manni He, and Helen Min Yang greatly helped me learn how to be a good mentor through our interaction.

I would also like to thank Prof. Graham Fleming, whose Spectroscopy class transformed my understanding about my research and inspired me to explore new research directions. I am indebted to him, as well as my previous collaborators Prof. Li Gan and Prof. Chaolin Zhang, for their kind support to my pursuit of a career in research. I also appreciate the thoughtful suggestions from Prof. Gerard Marriott, Prof. Phillip Geissler, and Prof. Alexander Pines.

A lot of work in this dissertation could not have been accomplished with the technical support from the research facilities run by UC Berkeley. I would like to thank the staff at the Cell Culture Facility, the DNA Sequencing Facility, and the Cell and Tissue Analysis Facility for their exceptional service.

Lastly, I want to thank my family and my friends who are supportive in every aspect of my life.

Introduction

The reductionist approach, whereby one aims to explain the properties of a complex system by the behavior of its components, lies at the heart of modern science. The capability of observing and understanding the microscopic constituents of a system is enabled by microscopy. Invented in the late 16th century and improved by Robert Hooke and Anton van Leeuwenhoek, optical microscopy helped lay the foundation of modern biology by revealing the cell as the basic unit of all living forms.[1] However, such microscopy based on detecting the difference in transmission of white light due to light-object interactions often fails to further unveil the working mechanisms within the cell. The reason is twofold. Firstly, the cell is a highly complex system on the molecular level, which makes it challenging to dissect the function of each component without specifically labeling it. Secondly, a typical cell does not absorb or scatter white light very strongly, leading to low contrast against the background.

The discovery of molecular fluorescence and the ensuing development of fluorescence microscopy overcome the two limitations of the transmission-type optical microscopy.[2] The wavelength difference between the incident light and emission light in fluorescence and the low amount of intracellular fluorescent biomolecules in the visible range allow observation of the emission signal with little background noise. With fluorescent molecules conjugated to antibodies against a certain component of the cell, one can specifically interrogate its distribution and abundance within the cell. The surge of molecular biology techniques during the past few decades has made it now possible to study essentially any type of biomacromolecules in living or fixed cell samples by fluorescence microscopy.[3]

Despite the success of fluorescence microscopy in studying a specific type of molecule in the cell, there remains a gap from seeing one type at a time to seeing one molecule at a time. The latter situation is desired because an ensemble should be explainable by its components, but not vice versa as some single-molecule-level heterogeneities may be averaged out in bulk measurements.[4] Although most biomacromolecules, including proteins and nucleic acids, are smaller than 10 nanometers (nm) in size, their image on the camera after the microscope is enlarged due to diffraction of light. The image of a light-emitting point source, also known as the point spread function (PSF), measures approximately half the wavelength of emission, a value that falls in the range of 200-300 nm for conventional fluorescence microscopy.[5,6] This effect blurs the image of a protein by 10-100 fold and severely compromises the capability of resolving single molecules by fluorescence microscopy, and is thus called the “diffraction limit”.

Another concern about seeing single molecules is the signal-to-noise ratio. Whereas the fluorescence signal is predominantly attributed to the dye-labeled molecule, there are several sources of noise within the visible range.[2] Even when the molecules are highly sparse so that discerning them apart is no longer precluded by the diffraction limit, fluorescence microscopy with wide-field illumination still cannot visualize them individually because of the low signal-to-noise ratio. Theoretical treatment predicts an illumination volume of ~1 femtoliter (fL) to obtain a sufficient signal-to-noise ratio for single-molecule detection in biological samples.[2]

The first true single-molecule fluorescence microscopy was achieved in the late 1980s, by virtue of technological advances of confocal[7] and total internal reflection (TIR)[8] illumination schemes

that can reach sub-fL excitation volume to suppress the noise. It was later established that the position of imaged individual molecules could be estimated at a precision of ~10 nm by fitting the PSF with theoretical or semi-empirical models, more than 10-fold beyond the diffraction limit.[9,10] However, in the crowded cellular environment where the same type of protein has 10^3 to 10^6 copies within the ~1,000 fL volume[11], it was impossible to acquire such single-molecule PSFs because the images of neighboring molecules would overlap. Therefore, early single-molecule microscopy was restricted to studying sparsely distributed fluorescent molecules in vitro.[12–14]

Around 2006, single-molecule microscopy was transformed for studying biomolecular distribution in intact cells independently by several groups.[15–18] The key concept is to separate spatially overlapping fluorescent molecules in the temporal domain by harnessing the photochemical properties of dye molecules. At any moment during image acquisition, only a small fraction of labeled molecules, typically <1 per square microns (μm^2), is lightened up to avoid spatial overlapping of the PSF. Different fractions of molecules are switched on and off at different times, the sum of which recovers the original distribution of molecules but with much higher precision as a result of the >10-fold enhancement by fitting single-molecule PSF. Betzig et al and Hess et al achieved this by using photoactivatable fluorescent proteins as labels and called their method Photoactivated Localization Microscopy (PALM).[15,16] Rust et al used photoswitchable organic dyes and named the method Stochastic Optical Reconstruction Microscopy (STORM).[17] In addition to photoactivation and photoswitching, reversible dye-target binding can be used to separate different molecules in the temporal domain, which underlies the development of Points Accumulation in Nanoscale Topography (PAINT) pioneered by Sharonov and Hochstrasser.[18] The capability of resolving intracellular structures at ~10-nm resolution opened the chapter of super-resolution microscopy (SRM). PALM, STORM, and PAINT are often summarized as single-molecule localization microscopy (SMLM), featuring their direct addressing the positions of single molecules for SRM.[19]

It is noteworthy that there is another class of methods to SRM by patterned illumination. Structured Illumination Microscopy (SIM)[20] uses the addition of striped excitation patterns of low spatial frequency to retrieve sample information of higher spatial frequencies, thus achieving image resolutions down to ~100 nm. Stimulated Emission Depletion (STED) Microscopy,[21] by contrast, shrinks the diffraction-limited confocal excitation volume with a ring-shaped depletion pattern. Although these methods are also widely used in research, they do not directly observe individual molecules, which is the focus of this dissertation.

The past 15 years since the invention of SMLM have seen numerous discoveries of previously unknown cellular structures enabled by the >10-fold improvement in image resolution.[6,19] Most exciting findings include the highly periodic, membrane-associated cytoskeleton across cells of the nervous system,[22] and the *in situ* visualization of organization of genes and other genetic elements within the cell nucleus.[23,24] Some of my work at the beginning of my graduate research focused on the use of STORM for resolving membrane-associated cytoskeleton in neural stem cell differentiation[25], in pathological neuronal models[26,27], and in red blood cells[28]. Nevertheless, besides the structures formed by biomacromolecules, one would readily recognize that the abundant small molecules and their physicochemical properties are also critical to shaping the cell.[29,30] Notable properties include the hydrophobicity of the membrane which determines its permeability to solutes, the viscosity of the cytoplasm which defines the probabilities of molecular

encounter, and the acidity (pH) of the cytoplasm which modulates the charges on biomacromolecules. Mapping these physicochemical properties at nanoscale resolution as what has been achieved for macromolecule-based structures would immensely deepen our understanding of the organizing principles of the cell.

Plotting a subcellular map of physicochemical properties requires such properties to be reported by fluorescent signals. Environment-sensitive fluorophores are thus crucial to accomplish the goal.[31–33] In fact, environment-sensitive fluorophores have been noticed even before the emergence of fluorescence microscopy. For example, the lipophilic dye Nile Red was synthesized in the 1960s and its spectral shift with solvent polarity (solvatochromism) was spectroscopically characterized.[34] So far, many environment-sensitive fluorophores have been published who report the physicochemical environment in their vicinity by various fluorescent readouts, including fluorescence intensity, emission or excitation spectrum, fluorescence lifetime, and polarization.[35] Accordingly, microscopy techniques have been developed to detect different types of fluorescence change, which are collectively called "functional microscopy" or "functional imaging", with "functional" indicating physiologically relevant physicochemical parameters.[36] Yet at the time I began my graduate research, few designs could achieve sub-diffraction resolution.

This dissertation aims to establish connections between single-molecule microscopy and functional imaging, which are conventionally studied by biophysicists and chemical biologists, respectively, to achieve super-resolution mapping of intracellular physicochemical properties. We named this class of methods "functional super-resolution microscopy" (f-SRM).[36–38] I focus on the design, instrumentation, and novel biological findings by mapping membrane hydrophobicity and membrane/cytosolic diffusivity at ~100-nm spatial resolution.

In Part I, we start with a more thorough examination of different types of fluorescent signals for environmental sensing and explain why we considered the emission spectrum as most realistic for f-SRM (Chapter 1). Then we dive into the experimental design of spectrally resolved (SR) single-molecule microscopies, including SR-STORM and SR-PAINT, with the solvatochromic fluorophore Nile Red (Chapter 2). These novel techniques led us to single-molecule polarity mapping (SM*p*M) for cellular membranes, revealing the role of cholesterol in membrane lipid packing and the elusive organization of lipid rafts (Chapter 3). Closer inspection of single-molecule data inspired us to exploit the diffusional behavior of dye molecules for single-molecule diffusivity mapping (SM*d*M), another mode of f-SRM (Chapter 4). Combining SM*p*M and SM*d*M, we unveiled the nanoscale diffusional heterogeneities within the endoplasmic reticulum (ER) due to its contact with the plasma membrane, which is likely a result of local protein crowding (Chapter 5). We conclude by proposing new feasible modalities for f-SRM and their potentials in discovering the unknowns of the cell (Chapter 6).

In Part II, we first introduce the excitation-based multi-color microscopy as an alternative to currently prevailing emission-based multiplexed imaging. Although being diffraction-limited, it offers several advantages for imaging live-cell dynamics (Chapter 7). The unexpected finding of an extremely thin tubular organelle in the cell prompted us to further investigate its identity and formation mechanism. We found that the tubular organelle is an underappreciated carrier for certain soluble cargoes from the ER to the Golgi apparatus, and named it "tubular ER-Golgi intermediate compartment (t-ERGIC)" (Chapter 8). The biogenesis of t-ERGIC relies on the cargo

receptor SURF4, which recognizes an N-terminal motif of the cargo protein and phase separates at the ER exit sites. Our results establish a link between cargo receptors and the diversity of ERGIC and provide practical guidelines for targeting proteins to the secretory pathway.

Publications reproduced in this dissertation are listed below. Permission has been granted by all critical co-authors for the reproduction of the work in this dissertation.

*S. Moon[||], R. Yan[||], S. J. Kenny, Y. Shyu, L. Xiang, W. Li, and K. Xu. "Spectrally resolved, functional super-resolution microscopy reveals nanoscale compositional heterogeneity in live-cell membranes." Journal of the American Chemical Society **139**, (2017): 10944-10947.*

*R. Yan[||], S. Moon[||], S. J. Kenny[||], and K. Xu. "Spectrally resolved and functional super-resolution microscopy via ultrahigh-throughput single-molecule spectroscopy." Accounts of Chemical Research **51**, (2018): 697-705.*

*R. Yan, B. Wang, and K. Xu. "Functional super-resolution microscopy of the cell." Current Opinion in Chemical Biology **51**, (2019): 92-97.*

*L. Xiang[||], K. Chen[||], R. Yan, W. Li, and K. Xu. "Single-molecule displacement mapping unveils nanoscale heterogeneities in intracellular diffusivity." Nature Methods **17**, (2020): 524-530.*

*R. Yan, K. Chen, and K. Xu. "Probing nanoscale diffusional heterogeneities in cellular membranes through multidimensional single-molecule and super-resolution microscopy." Journal of the American Chemical Society **142**, (2020): 18866-18873.*

K. Chen, R. Yan, L. Xiang, and K. Xu. "Excitation spectral microscopy for highly multiplexed fluorescence imaging and quantitative biosensing." Light: Science & Applications (2021) DOI: 10.1038/s41377-021-00536-3.

R. Yan, K. Chen, and K. Xu. "Tubular ERGIC (t-ERGIC): a SURF4-mediated expressway for ER-to-Golgi transport." bioRxiv (2021): 438517.

[||] denotes equal contribution.

Part I: Development of Functional Super-Resolution Microscopy (f-SRM)

In this section, the conceptualization, design, and experimentation of f-SRM will be comprehensively discussed. We start with an analytical chemist's perspective, comparing different types of fluorescence readouts, or observables, that can be potentially integrated with single-molecule microscopy. We then dive into the proposal of using the emission spectrum for f-SRM, as it is instrumentally feasible and there has been a lot of reporter dyes whose emission shifts as the local environment changes. By realizing spectrally resolved SMLM (SR-SMLM), we survey biomembrane polarity at the nanoscale through detecting both the localization and the emission spectrum of each Nile Red molecule, the latter of which reports local solvent polarity. Another mode of f-SRM focusing on the diffusion of probe molecules is derived from further examination of Nile Red data. This additional parameter permits nanoscale mapping of diffusivity in both the membrane and the cytoplasm. More importantly, the polarity and diffusivity sensing mechanisms are orthogonal, enabling multiplexed f-SRM by simultaneously probing the two parameters. We summarize and discuss the rich information about the organization of cellular membranes revealed by multiplexed f-SRM. We conclude with an outlooking chapter envisioning novel modes of f-SRM, including those based on SMLM and other types of super-resolution approaches, for uncovering more previously invisible properties of the cell.

Chapter 1: Multiplexed single-molecule detection for f-SRM

1.1 Fluorescence readouts as functional reporters

To achieve f-SRM, we first need to consider how to encode the environmental property of interest in the fluorescence signal detected by fluorescence microscopy. Here we review the photochemistry of fluorescence and explain how changes in the relevant processes can be reflected in different fluorescence readouts. Specifically, we focus on the intensity, emission spectrum, excitation spectrum, lifetime, and polarization (or anisotropy) of fluorescence, and we omit nonlinear phenomena as incorporating the latter with single-molecule sensitivity would be arduous.

1.1.1 The mechanism of molecular fluorescence

Relevant processes in molecular fluorescence are summarized in the Jablonski diagram (Figure 1).[2] Starting from the equilibrium ground state, a molecule absorbs the excitation light and transitions to the Franck-Condon excited state with a timescale of femtoseconds (fs). This instant excited state soon (~picoseconds, ps) decays through vibrational relaxation and interaction with the solvent, to the equilibrium excited state. Several fates of the equilibrium excited state exist. For a typical fluorescent dye, the emission process is predominant, where a photon is emitted due to the transition to the Franck-Condon ground state in a few nanoseconds (ns), which then relaxes to the equilibrium ground state. Alternatively, the molecule can go back to the equilibrium ground state via nonradiative decay. A third route called inter-system crossing brings the singlet excited state to a usually long-lived triplet state, which decays to the ground state in microseconds (μs) to milliseconds (ms) by nonradiative processes or phosphorescence.

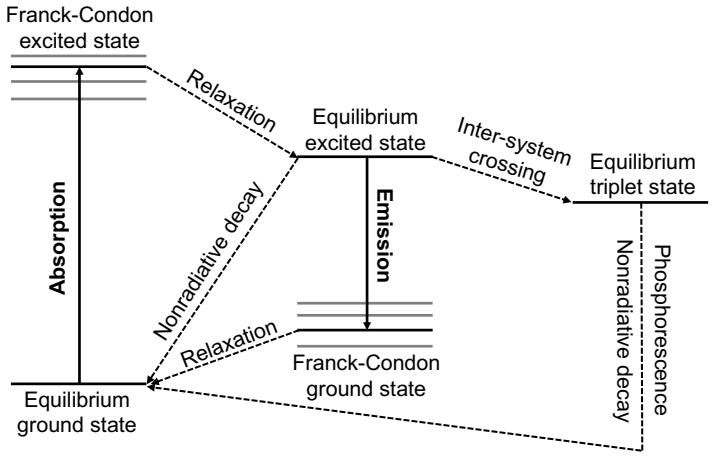

Figure 1: Jablonski diagram of the states and transitions in fluorescence. The heights of different states show the relative energy levels. See text for details.

1.1.2 Fluorescence intensity

Based on the Jablonski diagram (Figure 1), we can define the quantum yield (QY) by:

$$QY = \frac{k_e}{k_e + k_{nr} + k_{isc}} \tag{1.1}$$

where k_e, k_{nr}, k_{isc} denotes the rate constate of fluorescence emission, nonradiative decay, and inter-system crossing, respectively. The fluorescence intensity of a molecule is proportional to its brightness, which is defined as:

$$Brightness = QY * \varepsilon \quad (1.2)$$

where ε is the molar extinction coefficient.

Using a fluorophore that changes its QY or extinction coefficient according to the environment, one would then be able to sense spatiotemporal variation of the environment by monitoring its fluorescence intensity changes. Indeed, intensity-based environment-sensitive dyes have been the most widely studied type.[35] The QY of a dye can be modulated by changes in molecular structure (ground-state or excited-state) or alteration of the excited state kinetics. The commonest design of intensity-based probes employs the "turn-on" mode, where the QY increases from near zero to a considerable value in the presence of a specific analyte.[39] This leads to a dramatic increase in fluorescence signal at the detector under constant excitation power. Less commonly, the absorption of the dye may change to alter brightness. For example, some BODIPY fluorophores exhibit significant decreases in extinction coefficients in polar solvents (especially water) due to molecular aggregation.[40] We will see an indirect benefit of this phenomenon in Chapter 5.

1.1.3 Emission spectrum

The emission spectrum of a fluorophore reflects the energy gaps between the equilibrium excited state and its Franck-Condon ground states (Figure 1). Therefore, environmental properties affect the excited-state structure or dynamics. For example, Nile Red is such a dye whose emission spectrum changes with solvent polarity, known as a solvatochromism.[33,41] The electron of its tertiary amine is transferred to the distal oxygen in the excited state, rendering a large electric dipole of the molecule, which reorients with its neighboring solvent molecules to reach the equilibrium excited state (Figure 2A).[42–44] The amount of relaxed energy depends on solvent polarity, as more polar solvents lead to larger relaxation, or redder emission (Figure 2B). Nile Red thus serves as a reporter of solvent polarity, which will be useful in Chapter 3 and Chapter 5.

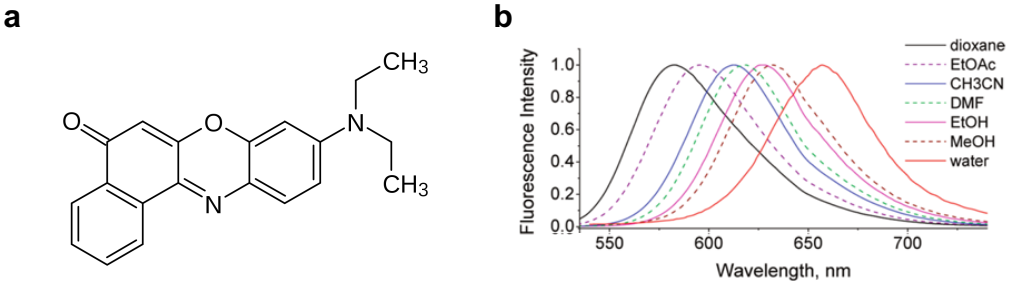

Figure 2: Solvatochromism of Nile Red. (a) Structure of Nile Red. (b) Normalized emission spectra of Nile Red in different solvents. Adapted with permission from Kucherak et al[44]. Copyright 2010 American Chemical Society.

The emission spectrum is typically recorded with a monochromator, such as the gratings and the prism. Its implementation on a confocal microscope is straightforward. The diffraction-limited confocal illumination spot functions as a pinhole, from which the emission light can be dispersed and recorded on a camera chip or an array of photomultiplier tubes (PMTs).[45,46] By contrast, it is

challenging for wide-field illumination because the spectra from different sources will substantially overlap in space. Although there has been progress in decomposing the emission spectra from a spectrally dispersed wide-field image, complex instrumentation and careful calibration are often required to rid spectral distortions.[47] For sensing purposes, however, the full emission spectrum is not necessarily required. It is plausible to draw a division line to separate the full spectrum into short-wavelength and long-wavelength channels, and when the line is appropriately placed, the ratio between the two channels will monotonically change with the spectral shift. Such so-called "ratiometric" imaging scheme has been widely used for wide-field, emission-based sensing with the addition of a dichroic mirror and another detector.[48]

1.1.4 Excitation spectrum

The excitation spectrum shows the variation of fluorescence intensity in a fixed spectral range of emission with the change of excitation wavelengths. Similar to the absorption spectrum, it probes the energy levels between the equilibrium ground state and the Franck-Condon excited states. In addition, as it convolves with fluorescence emission, it is also sensitive to excited-state dynamics, which shifts the energy level of the equilibrium excited state. The excitation spectrum can be mathematically described as:

$$I_{ex}(\lambda) = I_{il}(\lambda)\varepsilon(\lambda)QY(\lambda)\int_{em} I_{em}(\Lambda)\, d\Lambda \tag{1.3}$$

Where $I_{ex}(\lambda)$, $I_{il}(\lambda)$, $I_{em}(\Lambda)$ indicates the spectrum of excitation, illumination, and emission, respectively.

Instrumentally, the excitation spectrum is typically obtained by using a monochromator to select different spectral ranges of a continuum light source for excitation.[2] It is not commonly applied in modern fluorescence microscope designs, probably because the interpretation of the excitation spectrum is less intuitive than the emission spectrum, for the former involves more processes. We will discuss more about the excitation spectrum in Chapter 7.

1.1.5 Fluorescence lifetime

Although the name "fluorescence lifetime" may suggest its concern of the rate of photon emission from the excited state, what is experimentally measured is the excited-state lifetime:

$$\tau = \frac{1}{k_e + k_{nr} + k_{isc}} \tag{1.4}$$

It is apparent from Equation (1.4) that fluorescence lifetime is very sensitive to excited-state dynamics. Historically, fluorescence lifetime has been a standard measure for intracellular reactive oxygen species, which quenches the excited states of fluorophores.[49,50]

Fluorescence lifetime microscopy (FLIM) typically measures the lifetime in the time domain, using a confocal microscope with a pulsed laser and a time-correlated single-photon counting (TCSPC) detector.[2,49] The TCSPC detector counts the time of each photon reaching the camera, thus recovering the lifetime by fitting:

$$I(t) = I(0)e^{-\frac{t}{\tau}} \tag{1.5}$$

where $I(t)$ denotes fluorescence intensity at time t.

1.1.6 Fluorescence polarization and anisotropy

The fluorescence emission of a fluorophore is polarized along the direction of its emission dipole. With a polarizing beam splitter in the emission path, one can define the polarization ratio as:

$$P = \frac{I_{\parallel} - I_{\perp}}{I_{\parallel} + I_{\perp}} \tag{1.6}$$

where $I_{\parallel}$ and $I_{\perp}$ indicate fluorescence intensity parallel and perpendicular to the direction of the polarizer, respectively. A more convenient measure is the anisotropy:

$$r = \frac{I_{\parallel} - I_{\perp}}{I_{\parallel} + 2I_{\perp}} \tag{1.7}$$

The anisotropy is more commonly used because of the following relationship discovered by Perrin[51]:

$$r = \frac{r_0}{1 + \frac{\tau}{\theta}} \tag{1.8}$$

where r_0 is the intrinsic anisotropy in the absence of rotational diffusion, and θ is the rotational diffusion lifetime, which is proportional to the solvent viscosity and the size of the diffuser. For single-photon excitation of a randomly oriented ensemble of dye molecules, the intrinsic anisotropy is given as:

$$r_0 = \frac{2}{5}\left(\frac{3\cos^2\beta - 1}{2}\right) \tag{1.9}$$

where β is the angle between the molecule's excitation and emission dipoles.[2] The possible value of r_0 in this case is within the range [-0.2, 0.4].

As fluorescence polarization and anisotropy are sensitive to the dipole orientation and rotational diffusion of fluorophores, environmental effects on these parameters can be obtained by measuring the polarization of emission.[35] A wealth of fluorescence anisotropy data has been collected for understanding the geometry of dye-biomolecule interaction.[52] When the rotational diffusion lifetime is comparable to the fluorescence lifetime, fluorescence anisotropy can also report solvent viscosity and size change of the fluorophore, which has been particularly useful in characterizing ligand-protein interactions.[52,53]

1.2 Potentials of different fluorescence readouts for single-molecule-based f-SRM

In this section, we analyze different fluorescent readouts for their potentials in wide-field, single-molecule-based f-SRM. This imaging scheme is selected for its single-molecule sensitivity as well as its high throughput in measuring single molecules for super-resolution mapping, as opposed to scanning-based imaging.

Single-molecule sensing based on fluorescence intensity is both conceptually and instrumentally straightforward, but its accuracy is undermined by the uncertainty of single-molecule brightness under strong illumination and photoswitching.[54,55] It is well known for STORM and PALM, the brightness of the same dye follows an exponential distribution.[56] Such broad distribution is presumably due to the photoswitching and inter-system crossing which affects the on-off kinetics, namely the duty cycle of the dye.[56] A typical imaging frame in wide-field single-molecule microscopy takes 1 ms to 100 ms, which involves thousands to millions of excitation-emission cycles on the scale of ns, and stochastic digression into other long-lived states could contribute to the large variation in single-molecule intensity. PAINT suffers less from photoswitching, but the uncertainty in the timing of binding and unbinding events adds more complexity.[18,57] An

adequately large change in fluorescence intensity is thus required for reliable sensing. Fluorescence "turn-on" mechanism is suitable in this sense, which, nevertheless, has so far been limited to mapping environmental parameters in binary (0-or-1) than continuous (0-to-1) signals.[58,59]

Emission-based single-molecule f-SRM requires moderate modification of the emission path, which is similar to the design in a fluorometer. Different from confocal microscopy, where the fluorophore localization is determined by the position of the stage, a reference image (non-dispersed) is necessary for accurate localization of the spectra. In principle, spectrally resolved STORM/PALM/PAINT should achieve higher precision than intensity-based measurements, because the shape of the spectrum is insensitive to blinking effects. In 2015 and 2016, we and others reported different emission-resolved designs, which later turned out to be powerful tools for f-SRM.[60–62] We will discuss them in more detail in the following chapters.

By contrast, excitation-based single-molecule f-SRM is technically challenging, if not infeasible. The major obstacle comes from the relatively low brightness of single molecules. A typical environment-sensitive dye may continuously emit ~1,000 photons in a single-molecule event,[56] which will then be divided by the number of excitation channels. The resultant photon count in each spectral channel can be too low for accurate determination of the excitation spectrum. During the emission of these ~1,000 photons, the dye may transiently enter some relatively long-lived (μs) nonradiative states. The spectrum thus can have artifacts if an excitation channel coincides with these nonradiative states. On the other hand, the light source needs to be powerful so that in each narrow excitation spectral channel, it still provides enough illumination to observe single molecules. Current state-of-the-art light sources, such as supercontinuum lasers, are still 1 to 2 orders of magnitude lower in power for each ~10-nm spectral channel compared to single-wavelength lasers used for single-molecule microscopy.[63]

For fluorescence lifetime measurement, it is still challenging for wide-field microscopy due to the framerate limitation for commercial detectors.[64,65] The commonly used electron multiplying charge-coupled device (EMCCD) can only achieve ~1-ms framerate at its best for a meaningfully sized field of view,[66] which is far from what is required for time-domain FLIM (sub-ns). The scientific complementary metal oxide semiconductor (sCMOS) sensor is appreciably faster, reaching the μs domain at the expense of photon sensitivity,[66] yet it is still unsuitable for FLIM. Custom-designed, streak camera-based detection is recently used for wide-field FLIM, which transforms the temporally inaccessible lifetime information into the spatial domain by a fast-switching electric field.[67] However, this setup demands complex instrumentation, and for single-molecule measurement, such a strategy may not be promising for the low photon counts.[67] Wide-field FLIM with single-molecule sensitivity has been recently demonstrated with electro-optic modulation at frequencies comparable to the lifetime of common fluorophores.[68]

Similar to emission-based strategies, single-molecule polarization/anisotropy experiments are made plausible by modifying only the emission light path.[52,69] As the measurement is ratiometric, it is also insensitive to the intensity fluctuations for single molecules. Unlike the ensemble measurement, single-molecule anisotropy can fall in a larger range of [-0.5, 1], which potentially increases the dynamic range of sensing. There have been some fruitful results from single-

molecule anisotropy measurements, revealing nanoscale variation of cell membrane organization.[70,71]

Lastly, we briefly discuss the possibility of quantifying environmental viscosity or crowdedness by measuring the translational motion of single molecules. Although the velocity or diffusivity is not a fluorescence-specific property, it can be easily obtained from typical SMLM datasets, thus being an add-on functionality. For molecules that move relatively slowly (D < 1 μm^2/s), no additional instrumentation is required as at the typical SMLM recording rate of ~100 Hz, the motion blur caused by diffusion is smaller than the diffraction limit. For fast-moving molecules (D ~ 10-100 μm^2/s), stroboscopic illumination[72,73] can effectively reduce the motion blur at the expense of reduced single-molecule photon counts. More quantitative analysis will be presented in Chapter 4 and Chapter 5.

The discussion in this chapter is summarized in Table 1. Out of all types of fluorescence readouts, we think the emission spectrum, polarization/anisotropy, and velocity/diffusivity are most promising for single-molecule-based f-SRM. In the following chapters, we will focus on the experimental design and demonstration of emission-resolved f-SRM.

Table 1: Summary of different fluorescence readouts for f-SRM

Signal type	Mechanism	Compatibility with wide-field single-molecule microscopy
Intensity	QY or ε	Instrumentally simple but with uncertainty due to blinking
Emission spectrum	Excited-state structure or excited-state dynamics	Feasible with monochromator in the detection path
Excitation spectrum	Ground-state structure or excited-state dynamics	Instrumentally feasible with monochromator in the excitation path, but needs powerful light source
Lifetime	Excited-state dynamics	Requires complex instrumentation
Polarization (Anisotropy)	Dipole orientation or rotational diffusion	Feasible with polarizer in the detection path
Velocity/Diffusivity	Translational diffusion	Feasible without additional instrumentation (slow motion) or with stroboscopic illumination (fast motion)

Chapter 2: Experimental design of spectrally resolved SMLM

The work in this chapter was conducted in collaboration with Seonah Moon, Samuel J. Kenny, and Ke Xu. It is reproduced in part here from Yan et al[38] with permission from all co-authors. Copyright 2018 American Chemical Society.

2.1 Introduction

Tapping into the informative dimension of the fluorescence emission spectrum, we have previously realized spectrally resolved SRM for highly multiplexed imaging. By encoding functional information into this new spectral dimension with environment-sensing probes, f-SRM further enables the interrogation of local physicochemical parameters at the nanoscale. These

remarkable results are achieved by integrating the spatial, temporal, and spectral dimensions of single-molecule fluorescence.

Fluorescence detection provides a non-invasive and target-specific means to probe single molecules.[74–77] Figure 3a shows a typical wide-field fluorescence image of single Alexa Fluor 647 (AF647) molecules. Due to diffraction, single molecules appear as ~300 nm-sized spots. However, it is recognized that the position of a single molecule can be determined with nanometer-precision by fitting the intensity distribution of its image (Figure 3b) to known functions.[9,78] The ability to thus "super-localize" the position of a molecule is crucial for experiments that utilize the spatial information of single molecules.

Time trajectories of intensity represent another important aspect of single-molecule fluorescence. In particular, the integration of on-off intensity dynamics (fluorescence switching; Figure 3c,d) with the aforementioned ability to super-localize single molecules has led to the invention of SMLM,[15–17] a major class of SRM methods. In one such implementation, STORM, fluorescent molecules are first photoswitched to a non-emitting state. Small, random subsets of the non-emitting molecules are then photoswitched (Figure 3c) back to the emitting state and super-localized over different camera frames to construct an SRM image. In another SMLM approach called PAINT, the reversible binding/unbinding of fluorescent molecules to the sample (Figure 3d) is utilized to achieve single-molecule localization. Chemical reactions can also achieve on-off switching via the *in situ* generation of fluorescent molecules; super-localizing the product molecules enables super-resolution mapping of local reactivity.[77,79,80]

Spectrum measurement is another key component of single-molecule fluorescence, but one that is also highly challenging. Whereas the recording of total light intensity suffices for examining the spatial and temporal dimensions of single-molecule fluorescence, to scrutinize the spectral dimension would necessitate the wavelength-dependent detection of light. The use of a dichroic mirror to split fluorescence into long- and short-wavelength components offers a facile way to estimate the emission wavelength of single molecules by calculating the intensity ratio of the two components,[81,82] and this "ratiometric" approach has been successfully incorporated with SMLM.[83–85] However, actual spectra are not obtained, and the result is subject to sample background and performance of the dichroic mirror (Table 2).

To truly resolve single-molecule spectra, previous work has often employed spatially confined illumination and detection for spectral dispersion of the fluorescence from a single spot of the sample.[74,75,86–90] Sample scanning then enables the mapping of the positions and spectra of sparsely distributed molecules at different locations with limited throughput (Figure 3e). Although multiplexed arrays of confined illumination and detection spots have enabled the parallel measurement of single-molecule spectra with high throughput,[91] such approaches are difficult to apply to imaging and still rely on the sparse distribution of molecules.

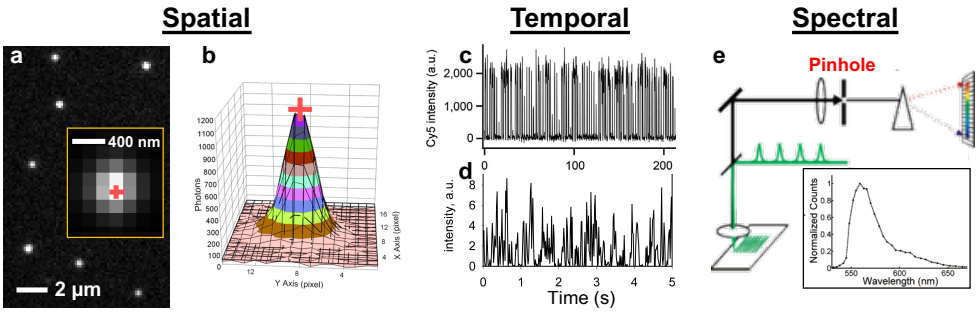

Figure 3: The spatial, temporal, and spectral dimensions of single-molecule fluorescence. (a) Wide-field fluorescence image of single AF647 molecules. (b) Intensity distribution of a Cy3 molecule as recorded by a camera. Red crosses in (a,b) mark peak positions. Adapted with permission from Yildiz et al.[78] (c) Laser-induced reversible fluorescence photoswitching of a Cy3-Cy5 dye pair. Adapted with permission from Rust et al.[17] (d) Fluorescence bursts due to the binding/unbinding of single Nile Red molecules to a lipid vesicle. Adapted with permission from Sharonov and Hochstrasser.[18] (e) Scanning-based single-location spectroscopy for single molecules. Adapted with permission from Luong et al.[90]

2.2 Spectrally resolved super-resolution microscopy via ultrahigh-throughput single-molecule spectroscopy

To overcome these limits in the context of SMLM, we reasoned that sparsely distributed single fluorescent molecules are discrete, self-confined point sources (Figure 4a).[60] Consequently, to collect their spectra, it appears unnecessary to impose further spatial confinement in illumination or detection as done in previous studies. Instead, using a prism, the emission of many molecules in the same field of view may be simultaneously dispersed into spectra and recorded with a camera (Figure 4b). Although analogous wide-field spectroscopy approaches are occasionally used in astronomy for stellar spectra,[92] their direct application to single-molecule experiments has been limited to sparse systems.[93,94] We found that by integrating SMLM with our wide-field spectroscopy scheme, a few-ms snapshot could readily capture the emission spectra of ~10^2 randomly distributed single molecules. Via photoswitching (for STORM) or reversible labeling (for PAINT), we then stochastically lit up different populations of molecules over consecutive camera frames, and obtained the spectra of ~10^6 single molecules in a densely labeled sample within minutes. In contrast with previous scanning-based single-location imaging/spectroscopy approaches in which a few molecules are probed per minute, we deem this wide-field approach "ultrahigh-throughput".

A hidden pitfall of the above wide-field scheme is that the spatial and spectral information of a randomly located molecule is coupled: the dispersed spectrum of a redder molecule may appear identical to that of a bluer molecule physically located further to the right. An independent reference image is thus necessary to decouple the spatial and spectral dimensions and produce the final result of SR-SMLM (including SR-STORM and SR-PAINT).

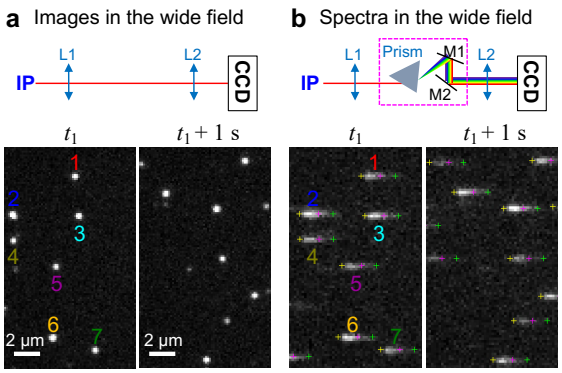

Figure 4: Wide-field fluorescence spectroscopy for single molecules. (a) Top: Wide-field image is relayed through lenses L1 and L2. IP: intermediate image plane of microscope. Bottom: A small part of the acquired images of single immunolabeled AF647 molecules in a fixed cell in two 9-ms camera frames separated by 1 s. (b) Top: A prism is placed at the Fourier plane between L1 and L2. Bottom: The dispersed spectra for the same molecules in (a), recorded in the wide-field concurrently with the images in (a). Yellow, magenta, and green crosses: spectral positions of 647, 700 and 750 nm for each molecule, mapped based on calibration obtained using narrow bandpass filters and lasers of known wavelengths. Adapted with permission from Zhang et al.[60]

In our initial work,[60] we employed a dual-objective scheme in which the sample is sandwiched between two opposing objective lenses, so that separate objectives are dedicated to the positional (Figure 5a, Path 1) and spectral (Figure 5a, Path 2) measurements of the same single molecules. This design achieves excellent light efficiency: the image channel of Path 1 is unmodified when compared to regular SMLM setups, whereas the spectral information from Path 2 is added on "for free". The major drawback is that samples need to be thin and transparent to allow imaging from the backside, and the mounting geometry is unfavorable for live-cell experiments.
Mlodzianoski et al reported an SR-SMLM system based on an inverted microscope with a single objective lens.[62] A beam splitter divided the fluorescence collected by the objective lens into two paths for separate positional and spectral detections of single molecules. We employed a similar strategy (Figure 5b) in our recent work on live cells in Chapter 3.[37] Although dividing the signal into two paths reduces the available photons for each path, this system imposes fewer sample constraints and is simpler in design.

Recent work has also reported SR-SMLM through concurrent positional and spectral recording via the zeroth and first diffraction orders of a grating,[61,95] a strategy used in earlier single-molecule/single-particle studies.[93,94] Although gratings could in principle provide higher resolving power over prisms and offer the benefit of linear dispersion, they achieve limited light efficiency, which could be a concern given the restricted photon budget for single molecules. Their strong dispersion also reduces the signal-to-noise ratio of each pixel and exacerbates overlapping between the dispersed spectra of different molecules, making it difficult to probe densely labeled two-dimensional structures.

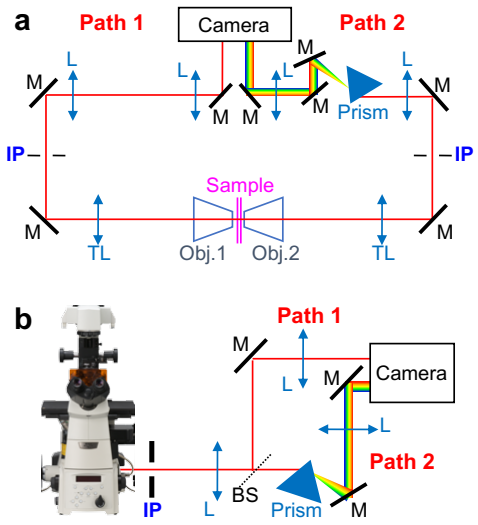

Figure 5: Concurrent positional and spectral measurement of single molecules. (a) System based on two opposing objective lenses. (b) System based on an inverted microscope with a single objective lens. Obj., objective lens; TL, tube lens; M, mirror; L, lens; BS, beam splitter; IP, intermediate image plane. For both schemes, Paths 1 and 2 provide unmodified images and dispersed spectra of single molecules, respectively.

Another strategy encodes the spectral information of single molecules into the shape of single-molecule images (PSFs).[96–98] Although such approaches remove the need for a reference image, they do not provide actual spectra. The spatial light modulator or phase mask involved also limits light-use efficiency. Color separation is thus only demonstrated for large wavelength differences. See Table 1 for a summary of different approaches and their major limitations.

Table 2: Spectroscopic approaches for SMLM

Method	Demonstrated multicolor SMLM	Major limitations	Ref
Ratiometric detection	4 fluorophores at ~20 nm separation	spectra not obtained; results subject to dichroic mirror	Bossi[83]/Testa[84]/ Gunewardene[85]
Dual-objective + prism	4 fluorophores at ~10 nm separation	thin, transparent samples only	Zhang[60]/Kim[99]
Beam splitter + prism	3 fluorophores at ~20 nm separation	photons split over two channels	Mlodzianoski[62]/ Moon[37]
Diffraction grating	2 fluorophores at ~20 nm separation	low light efficiency; signal spread over too many pixels	Dong[61]/ Bongiovanni[95]
PSF engineering	2 fluorophores at >100 nm separation	spectra not obtained; low light efficiency	Shechtman[96]

One immediate application of SR-SMLM is multiplexed SRM. To determine how well different fluorophores can be distinguished, we first characterized the intrinsic spectral variation between individual molecules of the same fluorophore.[60] Previous studies reported substantial spectral variation (standard deviation ~10 nm) for single dye molecules immobilized at solid surfaces (e.g.,

Figure 6a).[74,86–88] Meanwhile, ratiometric SMLM of dye-labeled biological samples found relatively high uncertainty in fluorophore identification (~20% crosstalk for 4 dyes at ~20 nm spectral separation),[83,84] and it was unclear how much of the uncertainty is due to intrinsic spectral variation between single molecules.

Remarkably, with SR-STORM, we found that in typical buffers, single immunolabeled dye molecules exhibit highly uniform fluorescence emission in cells (Figure 6bc).[60] Statistics of the spectral mean, calculated as the intensity-weighted average of wavelengths of each molecule,[88] gave a standard deviation of 2.6 nm for the ~6×10^5 individual AF647 molecules detected in the sample shown in Figure 4, with the brighter molecules (>10,000 detected photons) converging to an extremely small standard deviation of 1.4 nm (Figure 6c). Notably, a previous study measured the emission spectra of 220 single AF647 molecules electrokinetically trapped in an aqueous buffer, and it also noted a narrow distribution of emission wavelength (standard deviation ~3.5 nm).[100] Together, these results suggest that in aqueous buffers, single dye molecules may be characterized by much narrower emission distributions when compared to surface-trapped molecules. To generalize this finding, we investigated fourteen 647-nm-excited far-red dyes and found homogeneous single-molecule spectra for all (standard deviations of 2.5-4.5 nm in single-molecule spectral mean; Figure 6d). Meanwhile, substantial spectral differences were detected for different dyes (Figure 6d).

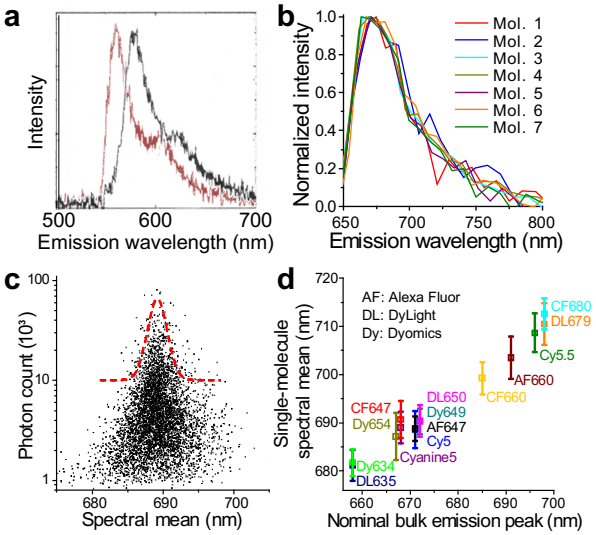

Figure 6: Variation in single-molecule fluorescence spectra. (a) Spectra of two $DiIC_{12}(3)$ molecules at a PMMA-air surface. Adapted with permission from Macklin et al.[87] (b) Spectra of the individual AF647 molecules labeled as 1-7 in Figure 4. (c) Measured spectral mean vs. photon count for 6,406 single AF647 molecules detected within 3 s. (d) Single-molecule spectral mean distribution of 14 different dyes, each obtained through SR-STORM from ~10^6 molecules. Error bars represent standard deviation between single molecules. (b-d) Adapted with permission from Zhang et al.[60]

The resolution of spectrally overlapping fluorophores by SR-STORM enables multiplexed, emission-spectrum-based super-resolution imaging. By color-coding each detected single molecule according to its measured spectral mean on a continuous scale, we found that in the resultant "true-color" SR-STORM images, molecules of different dyes were readily distinguishable, so that distinct colors showed up for the four differently labeled subcellular

structures (Figure 7a). Classification of the spectrum of each single molecule into the four dyes gave excellent separation (Figure 7b) and negligible (<~1%) misidentification (Figure 7c). Meanwhile, locally averaged single-molecule spectra for the different sub-diffraction-limit structures showed good agreement with corresponding dyes (Figure 7d). It is also apparent from Figure 7d that as the emission spectra are so heavily overlapping between the four dyes, color separation would not have been possible with conventional approaches using bandpass filters.

The excellent sensitivity of SR-STORM for common dyes suggests its usability for f-SRM with environment-sensitive fluorophores. In the next chapter, we focus on the application of Nile Red, a solvatochromic lipophilic dye, to revealing unexpected polarity differences between cellular membranes.

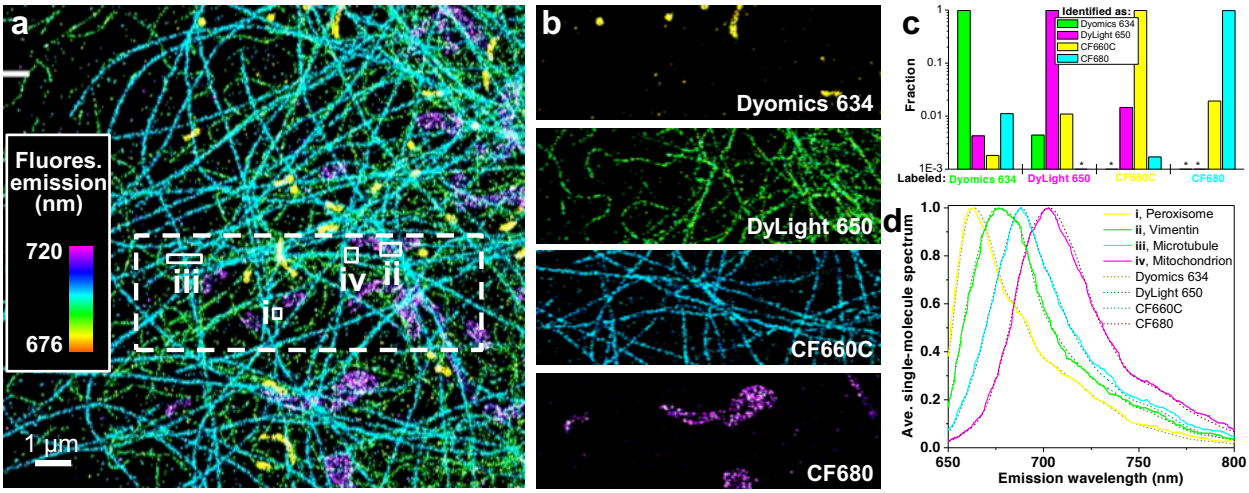

Figure 7: SR-STORM for four-color SRM. (a) "True-color" SR-STORM image of 4 subcellular targets immunolabeled by four far-red dyes at 10 nm spectral separation. Color presents the measured spectral mean of each molecule on a continuous scale (inset). (b) Separation of the four dye channels for the dash-boxed area in (a). (c): Identification/misidentification of the four dyes based on the measured single-molecule spectra (asterisks: $<10^{-3}$) (d) Averaged single-molecule spectra for the different nanoscale subcellular structures (i-iv) marked in (a), compared to that individually measured for the four dye molecules. Adapted with permission from Zhang et al.[60]

Chapter 3: Spectrally resolved f-SRM reveals nanoscale compositional heterogeneity in live-cell membranes

The work in this chapter was conducted in collaboration with Seonah Moon, Samuel J. Kenny, Yennie Shyu, Limin Xiang, Wan Li, and Ke Xu. It is reproduced in part here from Moon et al[37] with permission from all critical co-authors. Copyright 2017 American Chemical Society.

3.1 Introduction

Being chemically interconnected by diffusion and vesicular transport, cellular membranes are nevertheless compositionally and functionally heterogeneous.[101,102] Biochemical studies indicate remarkable compositional differences between the isolated plasma membrane and organelle membranes,[101,103,104] but their native organization in living cells is difficult to visualize[105–107] given the nanoscale dimensions of organelles. For the plasma membrane per se, research over the past two decades has debated the possible coexistence of liquid-ordered (Lo) and liquid-disordered (Ld) membrane domains, but this proposed phase separation at the nanoscale remains indeterminate.[108–111]

The difficulty of probing nanoscale heterogeneity in live-cell membranes arises from a lack of means to visualize it in an unbiased manner.[110–113] Labeling specific membrane components or phases with fluorescent probes is subject to labeling specificity and may shift the native equilibrium by stabilizing or disrupting the target being labeled. Environment-sensitive fluorescent probes,[35,114] in particular solvatochromic fluorophores that exhibit spectral shifts in media of varied chemical polarity,[33,41] provide a possibility to sense membrane heterogeneity without the need to label (and so potentially disturb) a specific target. Instead, the fluorophore may indiscriminately sample the membrane and reports local polarity through spectral changes: a lower local polarity corresponds to less membrane hydration and thus more orderly packed lipids.[31,113] With conventional detection methods, however, the diffraction of light limits spatial resolution to ~300 nm, and it is still difficult to obtain the full fluorescence spectra for every pixel. The low spatial resolution also limits polarity sensitivity as local differences in spectrum are averaged over all probes in the diffraction-limited volume.

The ultimate sensitivity of environment-sensitive probes may be reached if each probe molecule is individually examined, thus avoiding the averaging of potentially distinct spectra of different molecules. Taking advantage of stochastic fluorescence blinking, SRM techniques[115–117] like STORM[17] and PAINT[18,118] localize single molecules with high spatial resolution. A recent study[95] combined Nile Red, a solvatochromic dye, with SR-PAINT to enable surface hydrophobicity mapping.

By achieving Nile Red-based SR-STORM and SR-PAINT for live-cell membranes, we here detected local variations in membrane chemical polarity with single-molecule sensitivity and ~30 nm spatial resolution. This functional (as opposed to conventional, shape-only) SRM approach enabled us to directly visualize nanoscale compositional heterogeneity in the membranes of live mammalian cells.

3.2 Results and discussion

We use the single-objective design of SR-STORM (Figure 8a). Single-molecule positions and spectra in the wide-field were concurrently recorded on two different areas of an EM-CCD at 110-220 frames per second (4.5-9 ms integration per frame; Figure 8bc for representative raw data at a supported lipid bilayer and a live cell, respectively). With ~30 molecules detected in each frame (probe density <0.1 molecules/μm^2), we obtained the emission spectra and super-resolved locations of $>10^6$ single Nile Red molecules in a few minutes, thus enabling the reconstruction of super-resolution SR-STORM/SR-PAINT images that carried functional information on local chemical polarity. Concurrent positional and spectral recording may also be achieved via the

zeroth and first diffraction orders of a grating,[61,93,95] but gratings achieve low light efficiency, and the strong dispersion makes it difficult to probe densely labeled two-dimensional structures like cellular membranes.

We first applied Nile Red-based SR-PAINT to supported lipid bilayers of different compositions. Averaged spectra of the measured single Nile Red molecules (Figure 8d) showed the reddest spectrum for a bilayer of the unsaturated lipid 1,2- dioleoyl-sn-glycero-3-phosphocholine (DOPC), a model system for the Ld phase of the plasma membrane.[44] A bilayer of a 1:1 mixture of DOPC and sphingomyelin (SM), a more saturated lipid, showed a modest (~5 nm) blue-shift. Further addition of cholesterol (Chol) led to a substantial (~20 nm) blue-shift. These results are consistent with previous measurements on model lipid vesicles:[31,44,113] Nile Red exhibits fluorescence blueshifts in media of reduced polarity; the DOPC-only bilayer is the least orderly packed and so the most hydrated and polar, whereas cholesterol assists the packing of sphingolipids into more ordered and less hydrated membrane phases.

We next achieved Nile Red-based STORM and PAINT for membranes in live mammalian cells. For STORM, cells were labeled with 100 nM Nile Red, and imaged in a buffer containing ascorbic acid to assist photoswitching. For PAINT, unlabeled cells were imaged in a buffer containing 3 nM Nile Red for reversible binding to the membrane during imaging. For both approaches, the cell plasma membrane and the membranes of intracellular organelles were well labeled and visualized at the nanoscale [Figure 8e; arrows point to example ER (elongated tubular structures), mitochondria (thicker lumps), and plasma membrane]. With 50% fluorescence split to the image channel, we detected ~800 photons per molecule. This value is comparable to that of several known membrane STORM dyes, and translates to a spatial resolution of ~30 nm (localization precision in full width at half maximum [FWHM]).[119] Consistent with this resolution, the thinner ER tubules appeared 50-100 nm in width in our images, in agreement with previous results.[119] Three-dimensional (3D) STORM/PAINT indicated that for the plasma membrane, it was typically the top (apical) membrane that was imaged, which went out of the focal range for thicker parts of the cell (Figure 9). STORM/PAINT image sequences were obtained at ~30 s time resolution, which allowed us to track the morphological evolution of cellular membranes far beyond the diffraction limit (Figure 8e).

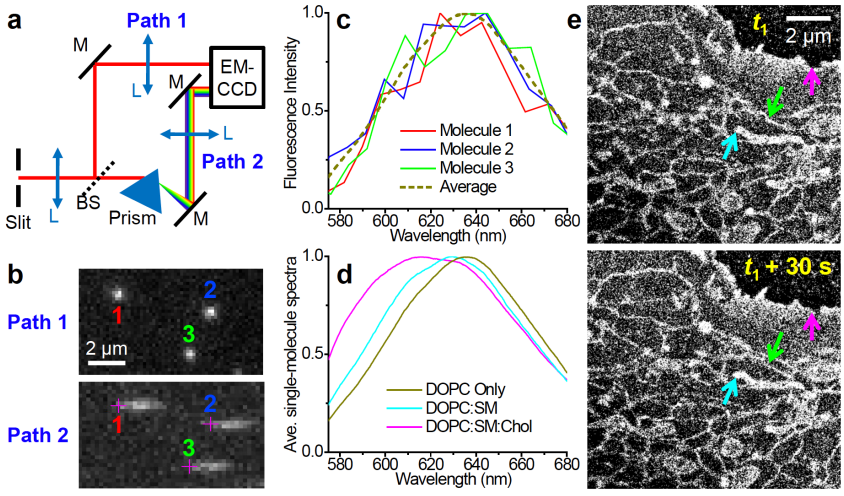

Figure 8: SR-STORM/SR-PAINT with Nile Red. (a) Schematic of setup. Slit is at the camera port of an inverted microscope. L, lens; BS, beam splitter; M, mirror. (b) A small region of the concurrently acquired images and spectra of single Nile Red molecules in a DOPC bilayer, obtained in a 6-ms snapshot. Crosses denote the mapped spectral positions of 590 nm for each molecule. (c) Spectra of the 3 molecules in (b), compared to that averaged from 280,898 single molecules from the same sample. (d) The averaged spectra for single Nile Red molecules labeled to supported lipid bilayers of different compositions (DOPC, DOPC:SM 1:1, and DOPC:SM:Chol 1:1:1). (e) Sequential STORM images of a Nile Red-labeled live COS-7 cell at 30 s separation. Magenta, green, and cyan arrows point to structural changes in the plasma, ER, and mitochondrial membranes, respectively.

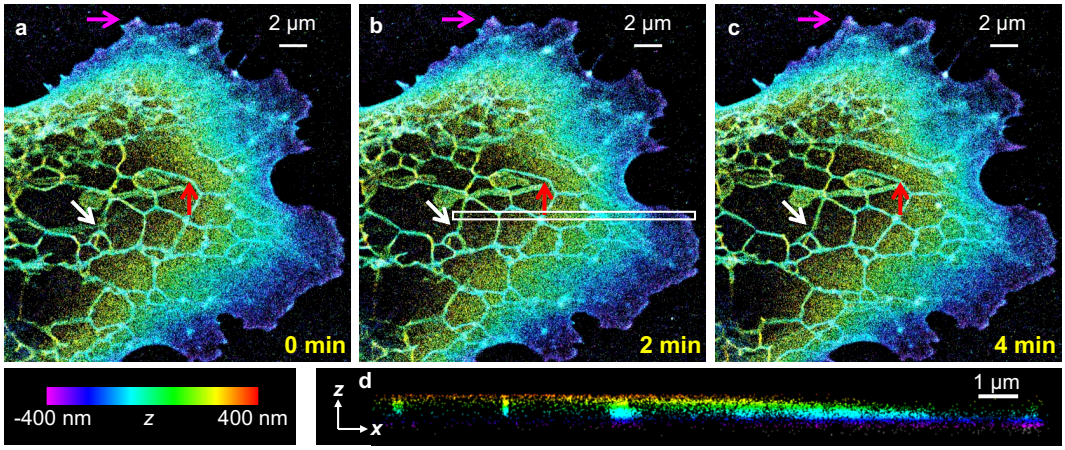

Figure 9: Nile Red-based 3D-PAINT of a live COS-7 cell. Note here color is used to represent height (*z*), with purple/blue being closest to the coverglass and red/yellow being farthest away, respectively [color scale below (a)]. (a-c) Sequential 3D-PAINT images at 2 min time separation. Magenta, white, and red arrows point to notable structural changes in plasma, ER, and mitochondrial membranes, respectively. (d) A vertical cross-section in the *xz*-plane along the boxed region in (b), showing that the top (apical) plasma membrane is imaged together with the membranes of intracellular organelles, and that this apical plasma membrane goes out of the focal range when far from cell edges, thus leaving only organelle membranes in the view.

Integrating Nile Red-based cell-membrane imaging with SR-STORM/SR-PAINT, we next asked whether the lipid composition-sensing capability we demonstrated for supported bilayers could reveal possible heterogeneities in the membrane composition of live mammalian cells. Remarkably, we observed significant spectral differences between Nile Red molecules at the plasma membrane and at the intra-cellular membranes of nanoscale organelles.

To present both the spectral and spatial information of every detected Nile Red molecule (~10^6 total for a typical image), we calculated the spectral mean of each molecule as the intensity-weighted average of wavelength,[60,88] and used this value to assign a color on a continuous scale (612-648 nm) as we plotted the position of each molecule. The resultant "true-color"[60] SRM images showed strikingly different colors for the plasma membrane (blue) and organelle membranes (yellow) (Figure 10a-c). Image sequences further showed that as the plasma and organelle membranes underwent dynamic structural rearrangements at the nanoscale, their respective spectral characteristics were maintained (Figure 10bc). Highly similar results were

obtained from SR-PAINT and SR-STORM (Figure 10a-c), and across different cell types (Figure 10a: PtK2, rat kangaroo epithelial cell; Figure 10bc: COS-7, monkey fibroblast). Fixed cells exhibited similar spectral characteristics as live cells (Figure 11), indicating that the membrane compositions are stable upon chemical fixation. The locally averaged single-molecule spectra, as computed from nanoscale subareas of the SR-STORM/SR-PAINT data, were nearly identical for mitochondrial and ER membranes, but showed a strong blueshift of ~20 nm for the plasma membrane (Figure 10d). Distribution of the measured single-molecule spectral means (Figure 12) showed similar standard deviations for the mitochondrial and plasma membranes over a DOPC bilayer (~6 nm), likely limited by our spectral precision. A slightly larger standard deviation of 7 nm was observed for the ER membrane.

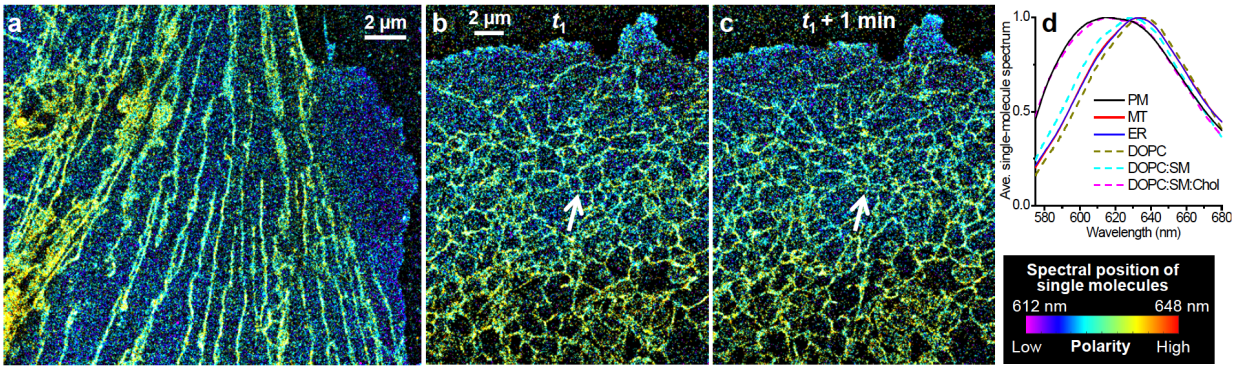

Figure 10: Spectrally resolved f-SRM visualizes polarity differences between organelle and plasma membranes in live cells. (a) True-color SR-PAINT image of a Nile Red-labeled live PtK2 cell. Each detected single molecule is color-coded according to its spectral mean [color bar below (d)]. (b,c) Sequential true-color SR-STORM images of a Nile Red-labeled live COS-7 cell at 1 min separation. Arrows point to notable structural changes in ER. (d) Averaged spectra of single Nile Red molecules from different nanoscale regions in live cells at the plasma membrane (PM), mitochondria (MT), and ER, compared to that at model supported lipid bilayers of different compositions.

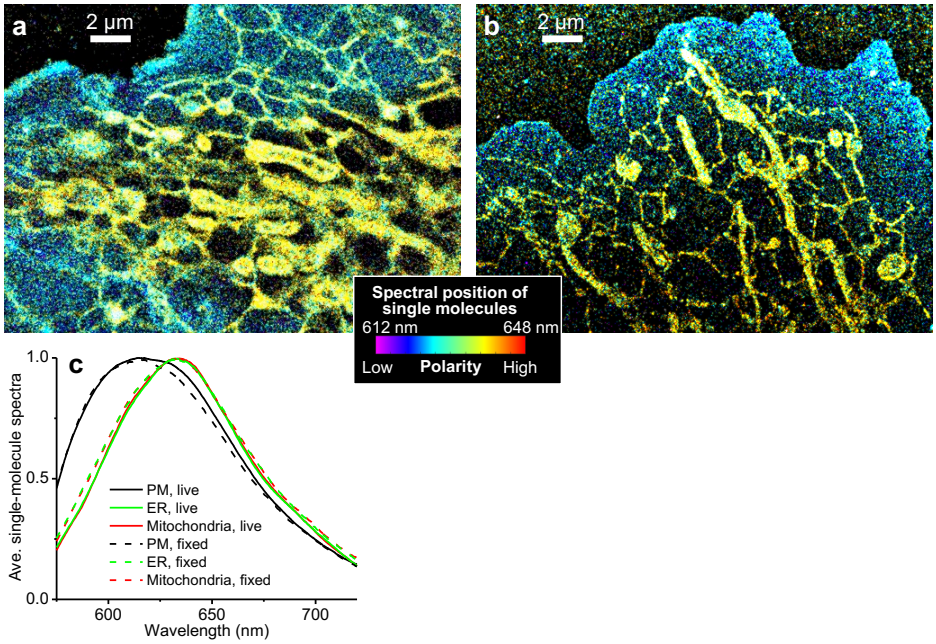

Figure 11: Comparison of Nile Red-based SR-STORM results on live and fixed cells. (a,b) True-color SR-STORM images of Nile Red-labeled live (a) and fixed (b) COS-7 cells. (c) Locally averaged Nile Red single-molecule spectra at the plasma membrane (PM) and mitochondrial and ER membranes, for the live (solid curves) and fixed (dotted curves) cells.

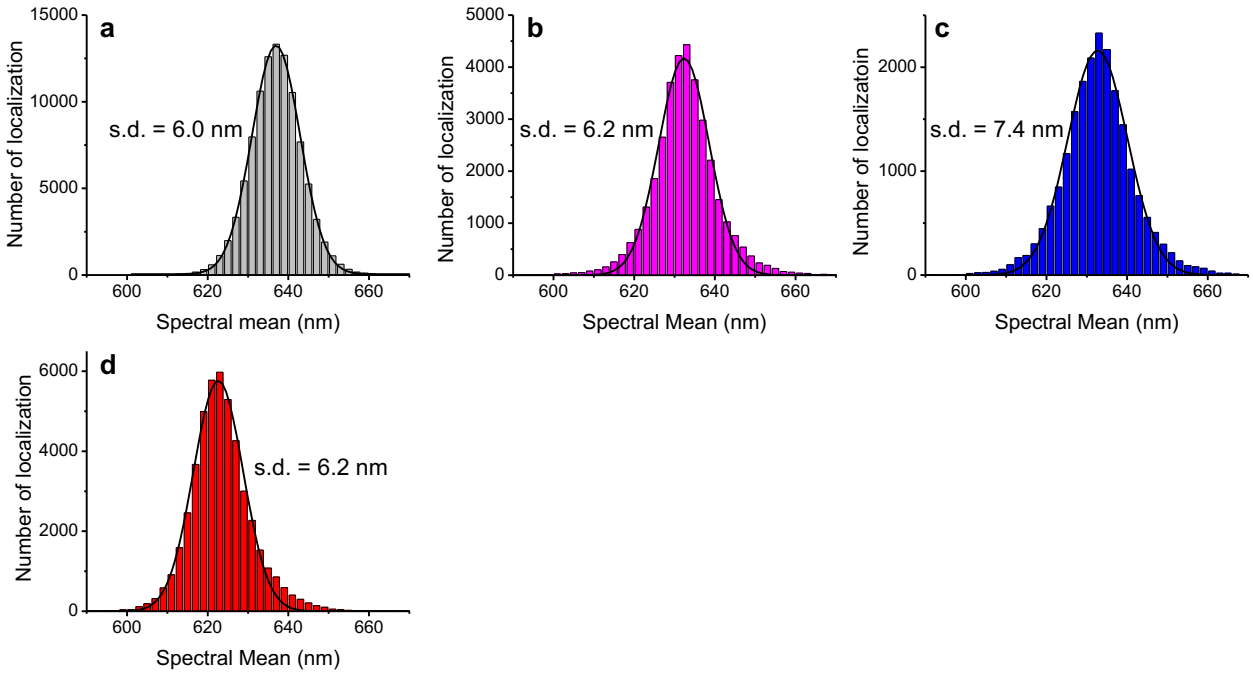

Figure 12: Distribution of the measured spectral means of single Nile Red molecules at different membranes. (a) Supported lipid bilayer of DOPC. (b) Mitochondrial membrane. (c) ER membrane. (d) Plasma membrane. Black lines are Gaussian fits with standard deviations (s.d.) labeled in each subfigure. The standard deviation of 6.0 nm in the (relatively homogenous) DOPC bilayer is likely limited by our measurement precision of single-molecule spectra. The similar standard deviations of 6.2 nm observed for the mitochondrial membrane and the plasma membrane suggest that they

are not significantly more heterogeneous than the DOPC bilayer at the spectral precision of our experiments. The ER membrane showed a slightly larger standard deviation of 7.4 nm, which may be related to its active lipid dynamics.

Together, these results reveal fundamental differences between the organelle and plasma membranes: the redder spectra of organelle membranes suggest that they are physically more polar, structurally less ordered, and functionally more flexible and permeable to water, consistent with their intracellular functions.[101,103]

Bulk measurements on isolated organelle and plasma membranes indicate that the former and latter are characterized by low (<~5%) and high (~30-40%) cholesterol levels,[101,103,104] respectively. As cholesterol assists the packing of lipid bilayers into more ordered and less hydrated membrane phases,[31,101,103] it may explain the significant differences in single-molecule spectra we observed between organelle and plasma membranes. Indeed, a comparison of our SR-STORM/SR-PAINT results on live-cell membranes and supported lipid bilayers showed that the organelle membranes are spectrally similar to cholesterol-free bilayers, whereas the plasma membrane is spectrally similar to the DOPC:SM:Chol (1:1:1) bilayer (Figure 10d).

To understand whether cholesterol is indeed the driving force behind the membrane polarity differences we observed, we next combined Nile Red-based SR-STORM with cholesterol manipulation via methyl-β-cyclodextrin (MβCD).[120] Depleting cholesterol with MβCD led to a strong redshift of Nile Red single-molecule spectra at the plasma membrane but little change at organelle membranes, as evidenced by both true-color SRM images and locally averaged single-molecule spectra (Figure 13ab).

In contrast, upon addition of 1 mM water-soluble cholesterol (cholesterol–MβCD), the organelle membrane spectra blue-shifted markedly to become closer to that of the plasma membrane as the latter remained spectrally unchanged (Figure 13ce). Substantial blue-shifts were observed for both the plasma and organelle membranes with 5 mM water-soluble cholesterol, so that both became bluer than that of the untreated plasma membrane (Figure 13de). A portion of the organelle membranes, however, appeared resistant to cholesterol addition, as indicated by nanoscale regions with redder colors in true-color SRM images and a shoulder peak in the locally averaged single-molecule spectra. Together, these results indicate that cellular cholesterol levels were responsible for the polarity differences we found for the plasma and organelle membranes.

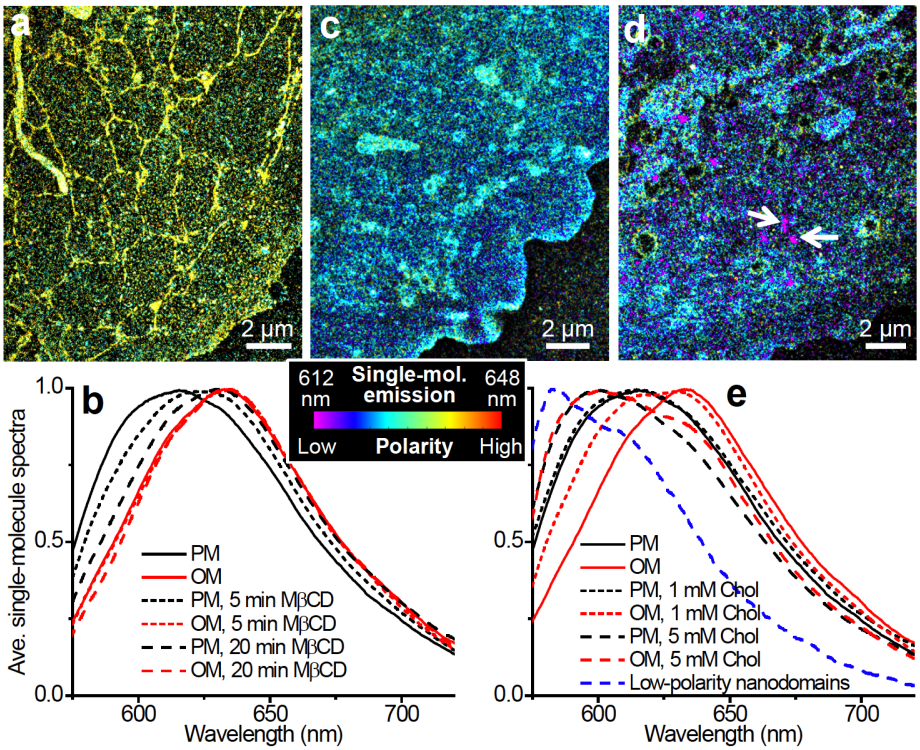

Figure 13: The observed heterogeneity in cellular membrane polarity is driven by cholesterol. (a) True-color SR-STORM image of a Nile Red-labeled fixed COS-7 cell after depletion of cholesterol with 5 mM MβCD for 20 min. (b) Averaged single-molecule spectra at the plasma membrane (PM) and organelle membrane (OM) after 5 and 20 min treatment of 5 mM MβCD, compared to that of untreated cells. (c,d) True-color SR-STORM images of Nile Red-labeled fixed COS-7 cells after cholesterol enrichment with 1 mM (c) and 5 mM (d) water-soluble cholesterol. Arrows in (d) point to low-polarity nanodomains. (e) Averaged single-molecule spectra at the plasma membrane (PM) and organelle membrane (OM), as well as at the low-polarity nanodomains, after cholesterol enrichment, compared to that of untreated cells.

Intriguingly, for fixed cells treated with 5 mM water-soluble cholesterol, in addition to an overall blueshift, SR-STORM further revealed nanoscale (apparent size ~100 nm; Figure 14) domains (arrows in Figure 13d) of strongly blue-shifted spectra (Figure 13e) dispersed across the plasma membrane. This finding, enabled by the unbiased sensing of local polarity by single Nile Red molecules, provides direct visual evidence of nanoscale phase separation of the plasma membrane. The strongly blue-shifted local spectra (Figure 13e) indicate highly nonpolar, orderly packed membrane domains, reminiscent of the long-hypothesized cholesterol-rich, raft-like liquid-ordered (Lo) nanodomains in the cell plasma membrane.[108–111]

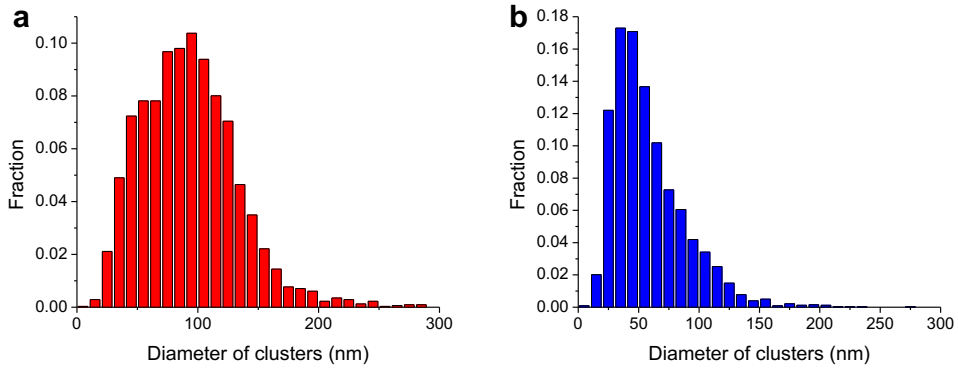

Figure 14: Distribution of the apparent sizes of low-polarity nanodomains in COS-7 cells induced by (a) addition of 5 mM water-soluble cholesterol and (b) application of CTB. Diameter of each nanodomain was defined by the smallest circle that could enclose 90% of the single-molecule localizations of the nanodomain. The resultant circle diameters are inflated by possible non-circular geometry of the nanodomains, as well as our localization uncertainty of ~30 nm in FWHM. The generally larger sizes observed with cholesterol addition (average: 90 nm) when compared to the CTB treatment (average: 60 nm) may be related to the different available amounts of cholesterol in the plasma membrane.

To further examine this possibility and elucidate whether raft-like nanodomains can also be observed in cells without cholesterol addition, we next attempted to stabilize Lo domains with cholera toxin B-subunit (CTB), a common lipid-raft marker and stabilizer[112,121] that crosslinks ganglioside GM1. Indeed, the application of CTB to cells induced blue-shifted nanoscale domains (Figure 15a and Figure 16 for fixed and live cells, respectively) that partly co-localized with CTB (Figure 15b and Figure 16), and the local single-molecule spectra (Figure 15c) were similar to those in cells with cholesterol addition (Figure 13e). Interestingly, we also observed a slight redshift for the rest of the plasma membrane (Figure 15c), attributable to global lowering of cholesterol levels as cholesterol was sequestered to the CTB-induced raft-like nanodomains. Meanwhile, no change in spectrum was observed for organelle membranes.

Our finding that raft-like, low-polarity nanodomains were only observed in cholesterol-added or CTB-treated cells suggests raft-like Lo domains may be absent in native cells. To examine if this interpretation is limited by our spatial resolution (~30 nm), we next employed a unique advantage of SR-STORM/SR-PAINT owing to its nature as ultrahigh-throughput single-molecule spectroscopy: without using any spatial information, individual molecules residing in phases of different polarities should show up as different subpopulations in single-molecule statistics. Indeed, for cholesterol-added and CTB-treated cells, the Lo phase is readily identified as a subpopulation of single molecules that are bluer in spectrum and brighter[122] in intensity (arrows in Figure 15de and Figure 16). Such a subpopulation is absent in untreated cells (Figure 15f). This observation suggests that in untreated cells, Lo nanodomains do not exist as a significant fraction of the membrane at time scales longer than our spectral integration time (5-9 ms), a result in line with evidence from recent single-molecule diffusion experiments.[123,124] However, we do not rule out the possibility that even a single Nile Red molecule could perturb the lipid dynamics in its immediate vicinity.

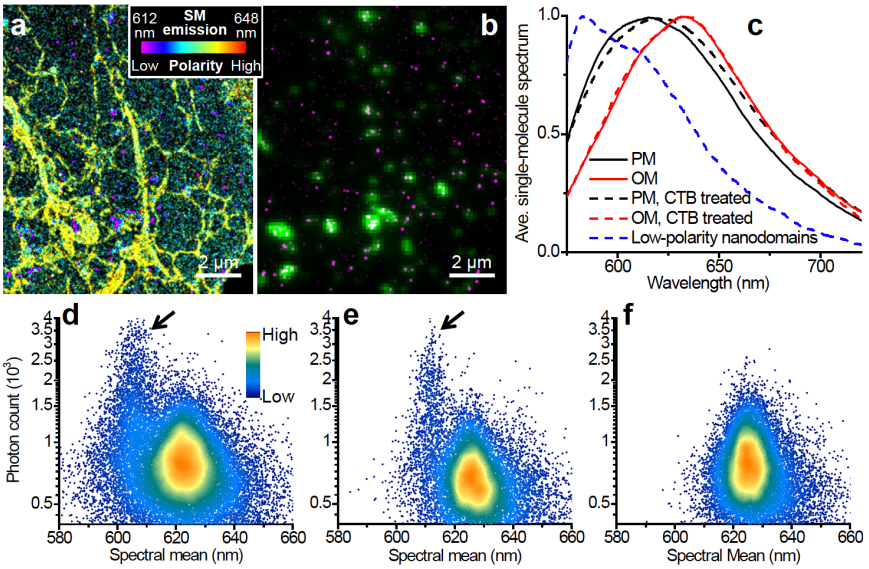

Figure 15: Functional SR-STORM examination of the low-polarity phase. (a) True-color SR-STORM image of a Nile Red-labeled COS-7 cell after CTB treatment and fixation. (b) The low-polarity nanodomains (magenta) overlaid with epifluorescence of the dye-tagged CTB (green). (c) Averaged single-molecule spectra at the plasma membrane (PM), organelle membrane (OM), and the induced low-polarity nanodomains after CTB treatment, compared to that of control cells. (d-f) Distributions of the measured spectral mean and photon count for single Nile Red molecules at the plasma membranes of cholesterol-enriched (d), CTB-treated (e), and control (f) COS-7 cells.

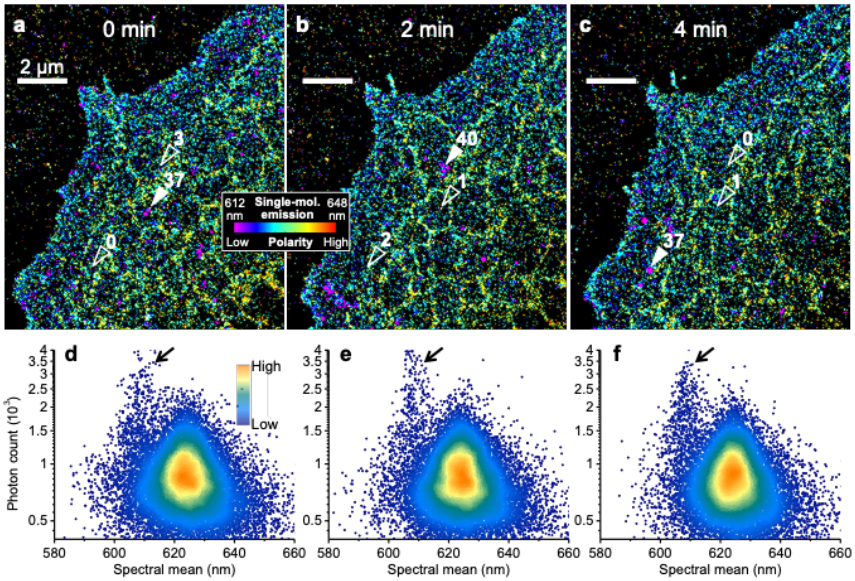

Figure 16: CTB treated live cells. (a-c) Sequential true-color SR-STORM images of a Nile Red-labeled live COS-7 cell after CTB treatment, at 2 min separation. Low-polarity nanodomains appeared (solid arrowheads) and disappeared (hollow arrowheads) at different locations over time. The number next to each arrowhead gives the count of blue-shifted single-molecule spectra (spectral mean < 612 nm) at the indicated position in each image. Low-polarity nanodomains were characterized by >30 blue-shifted local single-molecule spectra, whereas the <3 blue-shifted single-molecule spectra found for the same areas at other time points represent the background.

The time resolution of SR-STORM/SR-PAINT appeared too slow to follow the dynamics of the nanodomains. (d-f) Distributions of the measured spectral mean and photon count for single Nile Red molecules at the plasma membrane, for the corresponding time points.

3.3 Conclusion

By obtaining the fluorescence spectra and super-resolved positions of ~10^6 polarity-sensing single molecules per experiment, our functional SRM approach allowed for the unbiased visualization of nanoscale heterogeneity in live-cell membranes. The ultimate sensitivity we achieved through examining the spectra of individual molecules also opens the door to future interrogations of other parameters in live cells, including local pH, viscosity, and protein activity, at the nanoscale. The identification of suitable fluorescent probes for such applications, either independent of or in tandem with Nile Red, as well as the combination of functional SRM with traditional structural SRM experiments, represents immediate challenges.

3.4 Materials and methods

Optical setup

SR-STORM and SR-PAINT were achieved on a home-built setup (Figure 8a) based on a Nikon Ti-E inverted fluorescence microscope. A 561-nm laser (Coherent) was introduced to the back focal plane of an oil-immersion objective lens (Nikon CFI Plan Apochromat λ 100×, NA 1.45) via a dichroic mirror (ZT561rdc, Chroma). A translation stage was used to shift the laser beams toward the edge of the objective lens such that the excitation light reached the sample at incidence angles slightly smaller than the critical angle of the coverglass-water interface, illuminating ~1 μm into the sample. Emission was filtered by a long-pass (ET575lp, Chroma) and a short-pass (FF01-758/SP or FF01-715/SP, Semrock) filter, and cropped at the image plane of the microscope camera port to a width of ~4 mm. The cropped intermediate image was collimated by an achromatic lens (f = 80 mm) for splitting into two perpendicular paths at a 50:50 beam splitter (BSW10, Thorlabs). In Path 1, emission was focused by an achromatic lens (f = 75 mm) onto one-half of an electron-multiplying charge-coupled device (EM-CCD) camera (iXon Ultra 897, Andor) to achieve an effective magnification of ~94×. In Path 2, emission was dispersed by an equilateral calcium fluoride (CaF_2) prism (PS863, Thorlabs) before being focused by an achromatic lens (f = 60 mm) onto the other half of the same camera, thus resulting in an effective magnification of ~75×. Wavelength calibration was performed using fluorescent beads and narrow bandpass filters, as described previously.[60] Briefly, 100-nm diameter, four-color fluorescent beads (T7279, Life Technologies) were adsorbed to a glass coverslip at low density. The sample was mounted and imaged on the setup with 405 nm, 561 nm, or 647 nm excitation. Beads appeared as diffraction-limited spots in Path 1, and as dispersed 1D spectra in Path 2. Bandpass filters with ~10 nm bandwidths were used to determine the spectral positions of different known wavelengths in Path 2 relative to the bead positions in Path 1. 3D STORM/PAINT microscopy was achieved through cylindrical lens-based astigmatism.[125]

Supported lipid bilayers

Supported lipid bilayers were prepared via vesicle fusion of small unilamellar vesicles (SUVs). 1,2-dioleoyl-sn-glycero-3-phosphocholine (DOPC) and sphingomyelin were purchased from Avanti Polar Lipids (850375 and 860062). Cholesterol was purchased from Sigma (C8667). Each

lipid was separately dissolved in chloroform at concentrations of ~10 mg/mL. To prepare SUVs, the chloroform solutions of lipids were mixed in a pre-cleaned flask at designated ratios. After evaporation of chloroform with nitrogen flow, the flask was filled with ~55°C mili-Q water to form a 2 mg/mL lipid-water mixture. The mixture was sonicated at 60°C for ~40 min to form a clear SUV suspension. To form supported lipid bilayers on glass, hydrophilic glass coverslips were prepared by treatment with hot piranha solutions (H_2SO_4:H_2O_2 at 3:1). The coverslip was incubated in a 1:4 mixture of the SUV suspension and a buffer solution (10 mM HEPES, 150 mM NaCl, 3 mM $CaCl_2$) at 60°C for 15 min. After incubation, excess SUVs were rinsed away thoroughly with Dulbecco's phosphate-buffered saline (DPBS).

Cell culture

COS-7 and PtK2 mammalian cells were maintained in Dulbecco's Modified Eagle's Medium (DMEM) with 10% fetal bovine serum (FBS), 1× non-essential amino acids (NEAA) and 1% penicillin/streptomycin in 5% CO_2 at 37°C. For imaging, cells were plated at a density of ~10,000/cm^2 on 12-mm diameter glass coverslips, 35 mm glass-bottomed dishes (P35G-1.5-14-C, MatTek), or chambered coverglass (Thermo Scientific Nunc Lab-Tek II) to achieve a confluency of ~50% after growth of two days. For the fixed-cell SR-STORM/SR-PAINT experiments, cells were fixed with 3% paraformaldehyde and 0.1% glutaraldehyde in DPBS for 20 min, followed by a rinse with 0.1% $NaBH_4$ solution in DPBS for 5 min and three washes with DPBS.

Cholesterol depletion and addition

For cholesterol depletion, live or fixed cells were treated with a 5 mM solution of methyl-β-cyclodextrin (MβCD; Sigma C4555) in Leibovitz's L-15 medium (for live cells) or DPBS (for fixed cells) for 5−20 min. For cholesterol addition, live or fixed cells were treated with 1 mM or 5 mM solutions of water-soluble cholesterol (cholesterol–MβCD; Sigma C4951) in L-15 medium (for live cells) or DPBS (for fixed cells) for 30 min−2 h. Cells were then gently washed twice with L-15 medium (for live cells) or DPBS (for fixed cells).

Cholera toxin B-subunit treatment

Cholera Toxin Subunit B-Alexa Fluor 647 conjugate (CTB-AF647) was purchased from Invitrogen (C34778). Cells were briefly rinsed with Leibovitz's L-15 medium, and then incubated in 1 μg/mL CTB-AF647 in L-15 medium for 5-10 min at room temperature. Cells were washed twice with L-15, and immediately imaged as live cells or fixed as described above.

Nile Red staining

Nile Red (Acros Organics 415711000) was dissolved in dimethyl sulfoxide (DMSO) to a 3 mM stock solution. For live-cell experiments, cells were briefly rinsed with 37°C L-15 medium. For SR-STORM, cells were incubated with 100 nM Nile Red in L-15 medium for 20-30 min at 37°C, and then washed with 37 °C L-15 medium for two or three times before imaging. For fixed samples, cells were stained with 100 nM Nile Red solutions in DPBS, and then washed with DPBS for two or three times. For SR-PAINT, cells were not stained before imaging, and Nile Red was introduced in the imaging buffer (below).

SR-STORM and SR-PAINT imaging

SR-STORM and SR-PAINT were carried out on the optical setup described above. For SR-STORM, imaging buffer was L-15 medium (for live cells) or DPBS (for fixed cells) containing

100−200 μM ascorbic acid.[126] For SR-PAINT, imaging buffer was 3 nM Nile Red in either L-15 medium (for live cells) or DPBS (for fixed cells and supported bilayers). The sample was illuminated with the 561 nm laser at an intensity of ~2 kW/cm^2, which led to sparsely distributed images (Path 1) and spectra (Path 2) of single molecules in the wide-field due to the photoswitching (in STORM) or the dynamic binding/dissociation (in PAINT) of individual Nile Red molecules. The EM-CCD concurrently recorded the single-molecule spectra and images at 110 frames per second for a frame size of 512×256 pixels, or at 160-220 frames per second for a frame size of 512×128 pixels, and typically recorded 30,000−100,000 frames for each experiment. With ~30 molecules detected across each frame, the emission spectra and images of >10^6 single molecules were thus obtained within a few minutes. To map[60] the spectral and spatial coordinates of Path 1 and Path 2, a narrow bandpass filter centered at 590 nm (FF01-590/10, Semrock) was placed before the beam splitter for the final ~5,000 frames of the recorded movie. Comparison of the single-molecule images in Path 1 and the 590 nm-filtered single-molecule spectra in Path 2 thus enabled the generation of a mapping function between the spatial positions in Path 1 and the spectral positions of the 590 nm wavelength for Path 2. To analyze the SR-STORM/SR-PAINT data, the super-localized positions of single molecules in Path 1 were projected to Path 2 based on this mapping function. Single-molecule spectra were thus obtained based on the mapped position of 590 nm for each molecule and the aforementioned calibration curve obtained from fluorescent beads. Overlapping spectra were excluded from analysis. The spectral mean of each molecule was calculated as the intensity-weighted average of wavelengths for the measured single-molecule spectrum, and presented on a continuous color scale as "true-color" super-resolution images.[60] For live-cell results, time sequences of (SR-)STORM/PAINT images were generated using all the single-molecule localizations and spectra collected between the indicated time point (e.g., t_1) and the next time point in the sequence (e.g., t_1 + 30 s). Local averages of single-molecule spectra were calculated from nanoscale regions of the SR-STORM/SR-PAINT data for plasma membrane, mitochondrial membrane, and ER membrane of well-defined morphologies. Note that for thinner parts of the cell, the presence of the top plasma membrane confuses the local spectra of mitochondrial and ER membranes (c.f. Figure 9). Such regions were avoided in our analysis of the local spectra of organelle membranes.

Chapter 4: Single-molecule diffusivity mapping (SM*d*M): another dimension of f-SRM

The work in this chapter was conducted in collaboration with Limin Xiang, Kun Chen, Wan Li, and Ke Xu. It is reproduced in part here from Xiang et al[73] with permission from all co-authors.

4.1 Introduction

In the progress of the work on Nile Red in Chapter 3, when we looked more closely at the raw data showing the blinking of dye molecules, we noticed that they were also moving in the membrane. This is due to the liquid nature of membranes, in which molecules randomly swim. The motion of molecules is characterized by the diffusion coefficient, which is inversely proportional to the viscosity of the medium:

$$D = \frac{k_B T}{6\pi\eta R} \tag{4.1}$$

where η is the viscosity of the medium and R is the hydrodynamic radius of the diffuser. Therefore, if we could retrieve the local diffusion coefficient from the motion of dye molecules, we can map the environmental viscosity or crowdedness at super-resolution, too.

Starting from the law of diffusion, we derived formulas for the inference of the diffusion coefficient from molecular displacements between two camera frames. The Fickian diffusion law says the probability of finding a molecule at its original position decays over time as a result of:

$$\nabla^2 P - \frac{1}{D}\frac{\partial P}{\partial t} = 0 \tag{4.2}$$

We explicitly solve P in two-dimensional (2D) projection, which is more relevant to our TIRF-like illumination volume:

$$P(\vec{r}, t) = \frac{1}{4\pi D t} e^{-\frac{|\vec{r}|^2}{4Dt}} \tag{4.3}$$

where $\vec{r} = (x, y)$ can be the vectoral displacement between two camera frames. Assuming isotropy, we can simplify the measurement to scalars:

$$P(|\vec{r}|, t) = \frac{|\vec{r}|}{2Dt} e^{-\frac{|\vec{r}|^2}{4Dt}} \tag{4.4}$$

Equation (4.4) indicates that if we fix t, which is the time between two camera frames, and measure $|\vec{r}|$, which is the molecular displacement between two camera frames, we would be able to construct a histogram of $|\vec{r}|$ from measurements of many molecules in a small area. The shape of the histogram then contains the diffusion coefficient as the only fitting parameter. It should not be neglected that the abovementioned model is based on free and homogenous diffusion, with the presumption of ergodicity. It has been experimentally shown that this assumption is realistic for the ms timescale measured in f-SRM.[127,128]

It is also necessary to compare our approach with previous methods for evaluating diffusivity. Photobleaching and photoactivation-based techniques[129,130] enable single-location diffusion measurements but are unamicable to spatial mapping. Fluorescence correlation spectroscopy (FCS) and related methods[131–134] infer diffusivity from spatiotemporal fluctuations in intensity, but are sensitive to experimental conditions[132,135] and achieve limited resolution and sensitivity in live cells. Recent advances in STED-FCS offer new opportunities for high spatiotemporal resolutions, but are often limited to membrane-bound molecules and one-dimensional (1D) mapping of local diffusivity.[136,137]

Single-molecule tracking (SMT) has been highly successful for tracking the movements of membrane- and chromosome-bound molecules and for monitoring molecules diffusing inside the small volumes of bacteria.[138–143] However, it remains challenging to apply SMT to unbound molecules freely diffusing inside the eukaryotic cell. For an average-sized protein with an intracellular diffusion coefficient D of ~20-30 $\mu m^2/s$,[129,144] the ~10 ms frame time in typical wide-field single-molecule experiments results in ~700 nm of diffusion in each dimension, hence severe motion-blur. Although stroboscopic illumination overcomes motion-blur,[72,145] tracking between frames remains difficult for the eukaryotic cell: with ~700 nm axial displacement, a molecule initially in focus readily diffuses out of the focal range (~±400 nm for a high-NA objective) in the subsequent frame.

Our approach can potentially overcome these limits by determining the nanoscale displacements of freely diffusing single molecules in short (~1 ms) time windows through the application of a pair of closely timed excitation pulses. By repeating such pulse pairs ~10^4 times and locally accumulating the resultant single-molecule displacements, we can next construct super-resolution maps of diffusion rate, and hence uncover nanoscale diffusivity heterogeneities in live mammalian cells. We name this strategy single-molecule displacement/diffusivity mapping (SM*d*M).

4.2 Results and discussion

We started by expressing free mEos3.2[146], a photoswitchable, monomeric fluorescent protein (FP) commonly used in SMLM, in the cytoplasm of mammalian cells. Along with a short cloning-site sequence, the expressed protein (mEos3.2-C1) contained 252 amino acids (AA) (~28 kDa), close to the medium size of human proteins (248 AA by abundance[144]). As with typical SMLM experiments, we illuminated several micrometers into the coverslip-adhered live cells with a 561 nm excitation laser, and used a weak 405 nm laser to photoswitch a small fraction of the expressed mEos3.2 molecules to the 561 nm-excitable, "red" state, hence a means to control the amount of fluorescent single molecules in the view.[15,138] As expected, at a typical 109 Hz framerate (camera frame time T = 9.16 ms), freely diffusing single mEos3.2 molecules appeared blurry (Figure 17a). The application of stroboscopic illumination,[72,145] in which excitation pulses τ = 500 μs in duration were synchronized to the center of each camera frame, provided clear single-molecule images (Figure 17b). However, in the succeeding frame, after the frame time of T = 9.16 ms, molecules detected in the first frame already diffused out of the focal range and so could not be tracked (Figure 17b).

To overcome this issue, we reduced the temporal separation between the pair of captured images by placing two excitation pulses towards the end of the first frame and the beginning of the second frame, respectively (Figure 17c). Thus, at a Δt = 1 ms center-to-center separation between the two pulses, molecules being detected in the first frame (due to the first pulse) had only traveled moderately (to stay within focus) at the time of the second pulse (captured in the second frame) (Figure 17c). Comparing the super-localized positions of the molecules in the two frames thus yielded their nanoscale displacements (d) in the Δt = 1 ms time window.

We next repeated ~10^4 of the above paired frames to enable statistics (Figure 17d). The temporal proximity of the paired excitation pulses (Δt) left ample time between the unpaired pulses ($2T-\Delta t$) for different molecules to diffuse into the focal range as independent reporters of local diffusivity. The resultant, accumulated d values were spatially binned to evaluate local D. Fig. 1e-h show statistics for two spots ~400 nm apart (Figure 17j below), for bins 300×300 nm^2 (Figure 17ef) and 100×100 nm^2 (Figure 17gh) in size, respectively, that exhibited notably different local distributions. Fitting the distributions using a modified 2D random-walk model (see Materials and Methods for detail) through maximum likelihood estimation (MLE) yielded D with reasonable uncertainties for both bin sizes (Figure 17e-h). Color-plotting the D values from MLE of each 100×100 nm^2 spatial bin thus rendered a super-resolution map of local D across the full view (Figure 17ij).

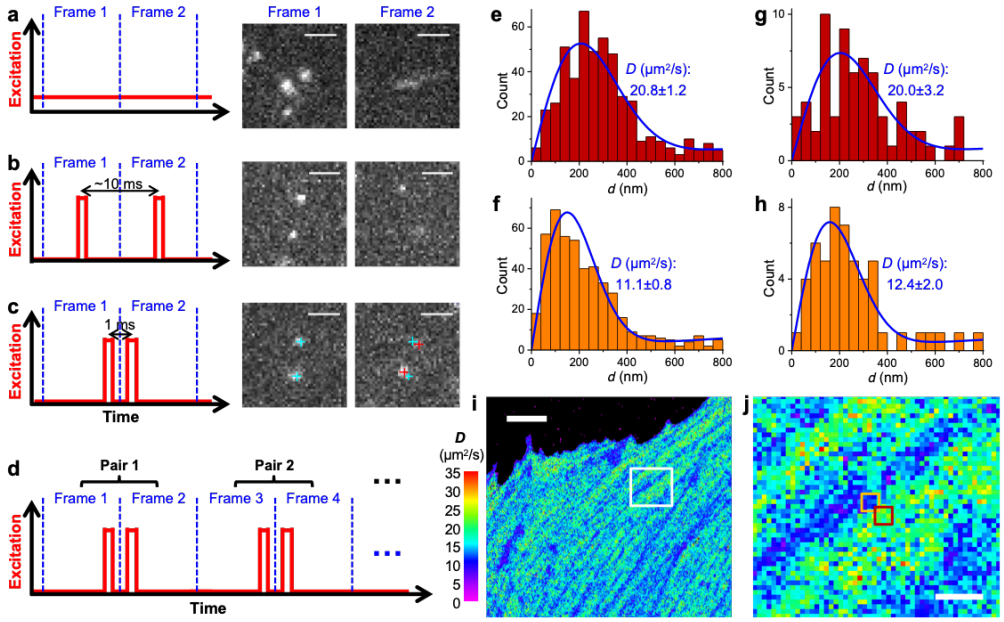

Figure 17: SM*d*M for single mEos3.2 FP molecules freely diffusing in the cytoplasm of live mammalian cells. (a) Conventional imaging with continuous laser illumination and a recording framerate of 109 Hz. (b) Stroboscopic illumination, with excitation pulses τ = 500 μs in duration synchronized to the center of each camera frame. (c) Placing two excitation pulses towards the end of the first frame and the beginning of the second frame, respectively, so that the center-to-center time separation between the two recorded images is reduced to 1 ms. Cyan and red crosses mark the super-localized positions of two detected molecules in Frame 1 and Frame 2, respectively. (d) Such paired frames are repeated ~104 times to enable statistics. (e,f) Distribution of the 1-ms single-molecule displacement d for two adjacent 300×300 nm^2 areas [red and orange boxes in (j)]. (g,h) Distribution of d for two 100×100 nm^2 areas at the centers of (e,f), respectively. Blue curves in (e-h) give MLE results using Equation (4.6) in Materials and methods with resultant diffusion coefficient D and uncertainty σ labeled in each panel. (i,j) Map of intracellular diffusivity constructed through MLE of the d distribution in every 100×100 nm^2 spatial bin. (j) is a zoom-in of the white box in (i). Scale bars: 2 μm (a-c), 5 μm (i), 1 μm (j). (i) and (j) were independently repeated 11 times with similar results.

For mEos3.2 molecules freely diffusing in the cytoplasm of live mammalian cells, SM*d*M showed typical D of 20-25 μm^2/s for the high-D regions (Figure 18ac), comparable to previous, spatially unresolved results on FPs obtained using FCS and photobleaching techniques.[129,144] Treating the cells with a 2× hyperosmotic medium led to substantially reduced D down to ~8 μm^2/s for the high-D regions (Fig. 17b), consistent with increased macromolecular crowding owning to water loss.[147,148]

Meanwhile, the spatial mapping capability of SM*d*M revealed substantial diffusivity heterogeneities at the nanoscale. For the flat, spread parts of cells, SM*d*M D maps often showed continuous, linear features where D reduced markedly down to ~10 μm^2/s (Figure 17i, 18ac). As these linear structures are reminiscent of actin cytoskeleton bundles, we fixed the cells and achieved correlated SMLM for actin using a dye-tagged phalloidin stain.[149] The low-D regions revealed by SM*d*M corresponded well with the SMLM-visualized actin bundles (Figure 18cd).

Plotting the SM*d*M-measured *D* values across an actin bundle 230 nm in FWHM gave an FWHM of 400 nm (Figure 18ef).

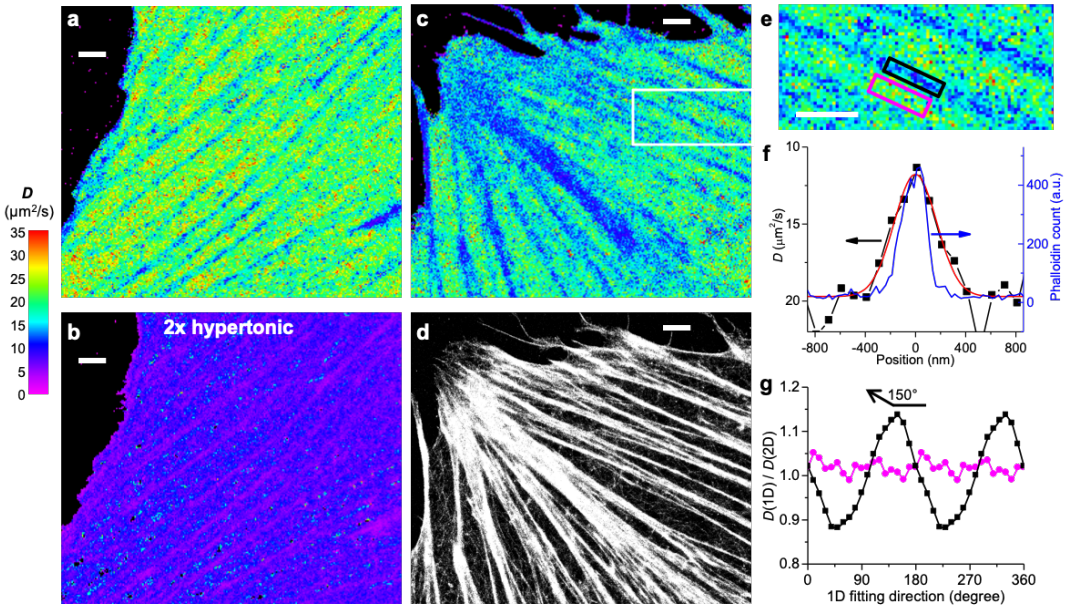

Figure 18: SM*d*M of free mEos3.2 in the mammalian cytoplasm and correlated SMLM of the actin cytoskeleton. (a) SM*d*M diffusivity map of mEos3.2-C1 in the cytoplasm of a live PtK2 cell. (b) The same cell in a 2× hyperosmotic medium. (a) and (b) were independently repeated 3 times with similar results. (c,d) Correlated SM*d*M diffusivity map of mEos3.2 in another live PtK2 cell (c), vs. SMLM image of Alexa Fluor 647 phalloidin-labeled actin in the fixed cell (d). (e) Zoom-in of the white box in c. (c), (d) and (e) were independently repeated 5 times with similar results. (f) Variations in the SM*d*M-measured *D* value (black squares on a flipped y-axis; red line: Gaussian fit with an FWHM of 400 nm) and the SMLM-detected phalloidin density (blue curve; FWHM is 230 nm; see y-axis on the right) across the black-boxed region in e. (g) Ratio of the *D* values obtained from the direction-dependent 1D diffusion models over that from the 2D isotropic model, for the black- and magenta-boxed regions in e, respectively. The *D* values from the 2D isotropic model are 12.4 and 21.8 μm^2/s for the two regions, respectively. Scale bars: 2 μm (a-e).

To examine whether the linear diffusivity features induced by the actin bundles could be characterized by diffusivity anisotropy, we fitted the SM*d*M-accumulated single-molecule displacements to 1D diffusion models in different directions (Materials and methods). For the actin-bundle region, the direction-dependent 1D diffusion models yielded *D* values that oscillated around the *D* value from the isotropic 2D model (Figure 18g), with a ~±14% difference achieved for the maximal and minimal values in directions along (e.g., ~150°) and perpendicular to the actin bundle, respectively. In comparison, for a region outside the actin bundle, the 1D diffusion models yielded little directional dependence, and the *D* values obtained were within a few percent of that obtained from the 2D model (Figure 18g).

By setting the focal plane a few micrometers into the cell, we next performed SM*d*M at the center of the nucleus (Figure 19a). *D* of ~20 μm^2/s was thus found for the fastest regions of the nucleus (red arrows in Figure 19a), consistent with the view that the nucleosol shares similar diffusion properties as the cytosol.[150] Meanwhile, micrometer-sized nucleoli were noted, which are expected

to be crowded with proteins and nucleic acids,[151] where the local D dropped substantially to ~6 $\mu m^2/s$ (asterisk in Figure 19a).

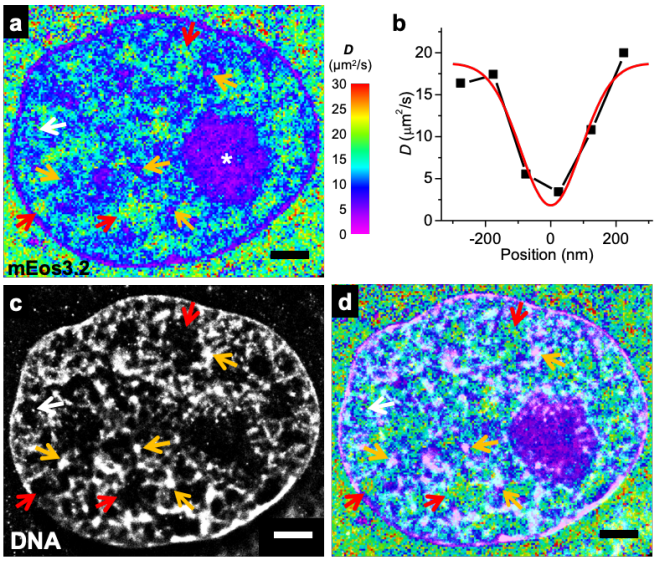

Figure 19: SM*d*M of free mEos3.2 in the nucleus, and correlated SMLM of DNA. (a) SM*d*M diffusivity map of mEos3.2-C1 at the central depth of the nucleus of a live PtK2 cell. (b) Variation in the SM*d*M-determined D along the horizontal direction for a spot-like structure marked by the white arrow in a. Red line: Gaussian fit with an FWHM of 220 nm. (c) SMLM image of the fixed cell using the DNA stain NucSpot Live 650. (d) Overlay of (a) and (c). Scale bars: 2 μm. These experiments were independently repeated 23 times with similar results.

Close examination of the SM*d*M data further revealed semi-structured, fractal-like nanoscale features of lowered D (~10 $\mu m^2/s$), which sporadically evolved into tight foci of very low D of <~5 $\mu m^2/s$ (orange arrows in Figure 19a). The white arrow points to one example in which SM*d*M resolved a diffusion slow-down region with an apparent FWHM of 220 nm (Figure 19b). Correlated SMLM on the fixed cell using a DNA stain (Figure 19c) showed that the highest D values were consistently observed for regions devoid of DNA (red arrows in Figure 19acd), whereas the low D regions corresponded to DNA structures, with the slowest foci often corresponding to clusters of high local DNA density (orange and white arrows in Figure 19acd), a structure indicative of densely packed structures as the heterochromatin. The spatial patterns of diffusivity correlated well with diverse chromatin ultrastructures.

By eliminating the need to track each molecule over consecutive frames but instead locally accumulating the instantaneous displacements of single molecules that stochastically entered the focal plane, SM*d*M successfully maps out how unbound proteins diffuse in the eukaryotic cell at the nanoscale. The application of a pair of closely-timed excitation pulses across tandem detection frames allowed access to single-molecule displacements down to 1 ms time windows in the wide-field, and by only detecting each molecule for two frames, relaxed the usual need for highly photostable fluorophores in SMT and FCS experiments.[134,140–142] The relatively long time lapse between the unpaired excitation pulses further facilitated the exchange of probes, so that non-photoactivatable fluorophores could be probed with high throughput inside the cell. The spatial

binning of single-step displacements for fitting to background-tolerant diffusion models may also be generally useful for the construction of high-resolution diffusion maps.

For the cytoplasm, SM*d*M unveiled actin-related local diffusivity heterogeneity and anisotropy. Whereas photobleaching and FCS experiments with actin disrupting agents have suggested that, at the whole-cell level, the actin cytoskeleton impedes intracellular diffusion,[152,153] imaging with viscosity-sensing dyes detects no distinct intracellular structures.[35,154] In contrast, SM*d*M directly resolved local decrease in *D* at the nanoscale and linked it to the SMLM-visualized actin ultrastructure. Fitting SM*d*M data to 1D diffusion models in different directions further unveiled diffusivity anisotropy, so that maximal and minimal *D* values were respectively observed along and perpendicular to the actin bundles. The moderate, up to ~±14% deviations of *D* values between the angle-dependent 1D and anisotropic 2D models for the actin-bundle region, together with the few-percent deviations for the non-bundle region, allow us to speculate that our 2D diffusion analysis in a fixed plane (due to the lack of axial localization) should largely capture the diffusive behavior in three dimensions. Whereas most previous studies on intracellular diffusion are based on isotropic diffusion models,[129–134] in-plane diffusion anisotropy has been occasionally examined.[155] The possible extension of SMdM to diffusivity anisotropy in 3D awaits future incorporation of reliable 3D localization methods that are immune to single-molecule motion-blur.

For the nucleus, the high resolution and sensitivity of SM*d*M helped establish, at the nanoscale, a direct association between local *D* and the SMLM-resolved chromatin ultrastructure. Although single-location FCS measurements have previously shown chromatin- and nucleolus-related diffusion slowdown,[156] FCS mapping in ~1 μm-spaced arrays finds no correlation between *D* and chromatin structure.[157]

4.3 Conclusion

SM*d*M has unveiled rich, nanoscale heterogeneities and charge effects in intracellular diffusivity. Whereas here SM*d*M has resolved diffusion features down to ~220 nm in FWHM, the ultimately achievable spatial, temporal, and diffusional resolutions depend on the actual system and await future experimental optimizations and theoretical analyses. The further integration of SM*d*M with other emerging super-resolution and single-molecule methods, e.g., SR-SMLM,[38,60] represents additional exciting possibilities. We will see in Chapter 5 how the combination of different f-SRM modalities helped reveal previously invisible properties in the membrane system.

4.4 Materials and methods

Optical setup

Single-molecule experiments were performed on a Nikon Ti-E inverted fluorescence microscope. Lasers at 488 nm (OBIS 488 LX, Coherent, 165 mW, for excitation of the non-photoactivatable GFP mEmerald and the un-photoactivated, “green” form of mEos3.2), 561 nm (OBIS 561 LS, Coherent, 165 mW, for excitation of the photoactivated, “red” form of mEos3.2) and 405 nm (Stradus 405, Vortran, 100 mW, for photoactivation of mEos3.2 to the “red” form) were collinearly combined and focused at the back focal plane of an oil-immersion objective lens (Nikon CFI Plan Apochromat λ 100×, NA 1.45) through a dichroic mirror (ZT488rdc-uf2 or ZT561rdc-uf2, Chroma, for the “green” and “red” channels, respectively). A translation stage shifted the laser beams

toward the edge of the objective lens so that the light reached the sample at an incidence angle slightly smaller than the critical angle of the glass-water interface, thus illuminating a few micrometers into the sample. Fluorescence emission was filtered by a long-pass filter (ET500lp or ET575lp, Chroma, for the "green" and "red" channels, respectively) and an additional band-pass filter (ET535/70m or ET605/70m, Chroma, for the "green" and "red" channels, respectively) in front of the EMCCD camera (iXon Ultra 897, Andor). The excitation and photoactivation lasers were modulated by a multifunction I/O board (PCI-6733, National Instruments), which also read the camera exposure output TTL signal for synchronization.

Plasmid constructs

mEos3.2-C1 was a gift from Michael Davidson & Tao Xu (Addgene plasmid # 54550),[146] and was used without modification as the "free" version of mEos3.2 (+2 net charge). mEos3.2-NLS was constructed by inserting the desired DNA sequence (Integrated DNA Technologies) between the SalI and BamHI restriction enzyme recognition sites within the short sequence at the C-terminus of mEos3.2-C1. Verification of plasmid constructs was confirmed through Sanger sequencing.

Cell culturing and transfection

18-mm diameter glass coverslips were cleaned with a heated piranha solution (sulfuric acid and hydrogen peroxide at 3:1), and then rinsed with Milli-Q water (18.4 MΩ cm). Ptk2 and U2OS cells were cultured in Dulbecco's Modified Eagle's Medium (DMEM) with 10% fetal bovine serum (FBS), 1× GlutaMAX Supplement, and 1× non-essential amino acids (NEAA) in 5% CO_2 at 37°C. 24 hours before imaging, cells were transfected with the Neon Transfection System (ThermoFisher) according to the recommended protocol, and then plated onto the pre-cleaned glass coverslips at a density of ~40,000/cm^2.

SM*d*M of live cells

SM*d*M of live cells was performed in a Leibovitz's L-15 medium containing 20 mM HEPES buffer, except for the hyperosmotic experiment, for which additional glucose was added at 49 mg/mL. For a typical recorded frame size of 256×256 pixels (~41×41 μm^2 sample area), the EMCCD camera exposure time and dead time were 9.0 ms and 157 μs, respectively, hence camera frame time T = 9.16 ms, corresponding to a frame rate of 109.3 frames per second. To access sub-frame temporal resolution, for each paired frames, two excitation pulses of duration τ (500 μs typically) were placed towards the end of the first frame and the beginning of the second frame, respectively (Figure 17c), at a center-to-center separation of Δt (1 ms typically). The wait time between the two excitation pulses was evenly distributed across the EMCCD dead time. The estimated peak and average power densities of the excitation lasers at the sample were ~6 and 0.3 kW/cm^2, respectively. For photoactivation of mEos3.2 to the "red" form, a low level of 405 nm laser was applied during the first half of the first frame in each paired frames to achieve a low density of emitting single molecules across the view. The average power density of the 405 nm laser was usually 0-0.05 W/cm^2, so that a typical single-molecule density of ~0.05-0.1 molecules/μm^2/frame was achieved, corresponding to ~0.1-0.2 molecules/frame in the area defined by the search radius R of 800 nm (below). Free diffusion of fluorophores during the relatively long time lapses between the unpaired excitation pulses helped maintain a useful density of single-molecules over time. The above scheme of paired excitation and photoactivation was repeated many times (5-7×10^4 typical) to generate the final SM*d*M data.

SMLM imaging of fixed cells after live-cell SM*d*M

After the above SM*d*M experiment on live cells, the sample was chemically fixed on the microscope stage for subsequent fluorescent labeling and SMLM imaging. For SMLM of the actin cytoskeleton, the cells were fixed with 0.3% glutaraldehyde and 0.25% Triton X-100 in the cytoskeleton buffer (10 mM MES [2-(N-morpholino)ethanesulfonic acid] buffer, 150 mM NaCl, 5 mM EGTA (ethylene glycol tetraacetic acid), 5 mM glucose, 5 mM $MgCl_2$, pH 6.1) for 1 minute, then fixed with 2% glutaraldehyde in the cytoskeleton buffer for 30 minutes.[149] The sample was then treated with a 0.1% $NaBH_4$ solution in phosphate-buffered saline (PBS) for 5 minutes × 2 times, and then washed with PBS for 10 minutes for 3 times. Actin was labeled with 0.5 μM Alexa Fluor 647-phalloidin (Invitrogen A22287) solution in PBS for 30 minutes, and then washed with PBS for 5 minutes × 2 times. For SMLM of DNA, the cells were fixed with 4% paraformaldehyde in PBS and washed with PBS for 10 minutes × 3 times. Then the DNA was labeled with NucSpot Live 650 (Biotium #40082) in PBS (1:1000) for 20 minutes. The sample was washed with PBS for 5 minutes × 2 times. SMLM was performed on the same microscope setup using a 642 nm laser (Stradus 642, Vortran, 110 mW). The SMLM imaging buffer was PBS containing 5% glucose, 200 mM cysteamine, 0.8 mg/mL glucose oxidase, and 40 μg/mL catalase. The acquired SMLM data were processed as described previously.[17]

Data analysis for SM*d*M

Single-molecule images were first localized as described previously.[17] For each pair of frames, the positions of the molecules identified in the second frame were used to search for matching molecules in the first frame within a cutoff radius R (800 nm typical). Cases in which more than one molecule is found within the search radius were rejected, and the remaining single-molecule mismatches were dealt with through the inclusion of background terms in the fitting models (below). 2D displacements (d) were calculated for the matched molecules, and the process was repeated for all the paired frames. The resultant, accumulated d values were spatially binned onto 100×100 nm^2 grids. The distribution of d in each spatial bin was next individually fitted through maximum likelihood estimation (MLE) to determine local D. The extraction of D from the distribution of single-step displacement has been previously examined,[158–161] typically using frame-to-frame displacements from long trajectories of individual particles. In SM*d*M, fitting is instead for different molecules that visit a given location for just a pair of frames in the very short duration of Δt, and we add one more term to accommodate mismatched molecules.

For fitting to an isotropic 2D random-walk diffusion model (since in our measurements we do not measure the axial position and only calculate the in-plane displacement), the probability density for a particle to move a distance r in the fixed time interval Δt is:[158–160]

$$P(r) = \frac{2r}{a}\exp(-\frac{r^2}{a}) \tag{4.5}$$

where $a = 4D\Delta t$. Assuming the density of background molecules (mismatches in pairing) to be spatially homogeneous within the search radius, the probability of finding a background molecule between r and $r+\mathrm{d}r$ is proportional to the area $2\pi r\mathrm{d}r$, which increases linearly with r. We thus modified Equation (4.5) to account for this background effect:

$$P(r)' = \frac{2r}{a}\exp(-\frac{r^2}{a}) + br \tag{4.6}$$

where b fits to the slope of a linearly increasing background. Using Equation (4.6) to fit the accumulated d values through MLE yielded robust results for experiments carried out at different single-molecule densities.

For fitting to 1D diffusion models in different directions, we first projected the single-molecule displacement d along different directions in the range of 0-360° in 10° steps, and then processed the projected results at each angle separately. In 1D random walk, the probability density for a particle initially at the origin to move to a location of x in the time interval Δt follows the normal distribution. An additional term b' is added to account for a uniform background in the detection of nonspecific (mismatched) single molecules, so that:

$$P(r)' = \frac{1}{\sqrt{a\pi}} \exp(-\frac{x^2}{a}) + b' \tag{4.7}$$

where $a = 4D\Delta t$. Using this equation to fit through MLE the d values projected to different directions gave angle-dependent 1D D values.

Chapter 5: Multiplexed f-SRM reveals hidden properties of membrane contact sites

The work in this chapter was conducted in collaboration with Kun Chen and Ke Xu. It is reproduced in part here from Yan et al[162] with permission from all co-authors. Copyright 2020 American Chemical Society.

5.1 Introduction

In Chapter 4, we present the application of SM*d*M in studying cytoplasmic and nucleoplasmic diffusion. In this chapter, we extend SM*d*M to the membrane system. By eliminating the need to track long trajectories as in single-particle tracking (SPT), SM*d*M is ideal for systems in which fluorophores only emit transiently. PAINT presents such a case for SMLM of the lipid membrane: As single probe molecules randomly enter the membrane phase from the aqueous medium, they turn on fluorescence emission and reside for ~10 ms before exiting,[57] thus allowing unbiased, high-density membrane sampling.[18]

Here we exploit the transient intra-membrane diffusion of single probe molecules in PAINT to achieve SM*d*M diffusivity mapping for cellular membranes. By identifying a bright fluorescence turn-on probe that enables sustained PAINT-type single-molecule imaging for $>10^5$ frames under stroboscopic illumination, we accumulate the super-resolved positions and transient displacements of $>10^6$ molecules in live-cell membranes. We thus achieve continuous fine mapping of the cellular membrane diffusivity to unveil heterogeneities at the nanoscale, and further integrate SR-SMLM to examine the possible roles of lipid packing order and protein crowding in local diffusivity differences.

5.2 Results and discussion

For effective probing of both the topography and diffusion properties of cellular membranes, we started by identifying the commercial BODIPY dye BDP-TMR-alkyne (Figure 20a) as an optimal probe. BDP-TMR has been reported as a water-soluble dye with a high affinity to lipid bilayers.[163] We found that when excited at 560 nm, BDP-TMR-alkyne exhibited ~10-fold fluorescence turn-on in organic phases vs. in the aqueous medium (Figure 20b), owing to substantially reduced and blue-shifted absorption in the aqueous phase (Figure 21). When added into the cell medium at 3.3 nM and excited at 560 nm, it emitted strongly over low backgrounds as single molecules transiently entered cellular membranes (Figure 20c). In comparison to Nile Red, the typical PAINT probe for lipid membranes,[18,37,118] BDP-TMR-alkyne was notably brighter and yielded superior single-molecule images (Figure 20c-e), consistent with its measured higher fluorescence quantum yield (~95%) and extinction coefficient (Figure 21). When excited by stroboscopic pulses of τ = 1 ms duration to minimize motion blur, a substantial fraction of the molecules emitted ~1,000 photons (Figure 20e), thus enabling reliable 3D localization through single-molecule image shape.[125] Similar to Nile Red, BDP-TMR-alkyne dynamically partitioned between the medium and membrane phases so that single molecules stayed in the membrane for ~10 ms,[57] a timescale ideal for the <10 ms displacement time window of SM*d*M (below). The rapid membrane-medium exchange created a steady state, so that continuous imaging was readily achieved for >1.6×10^5 frames with no appreciable drop in the single-molecule count (Figure 20f), from which 10^6–10^7 molecules were accumulated across the view. It is further worth mentioning that these results were achieved in the regular cell media without the need for an oxygen scavenger, other additives, or photoactivation.

For SM*d*M, we implemented two different excitation schemes while continuously recording in the wide-field at 110 frames per second (fps). Whereas the application of asymmetrically timed pulse pairs across tandem frames[73] at a Δt = 2.5 ms center-to-center separation helped limit the transient single-molecule displacement d to <~200 nm (Figure 20g) for more localized statistics, exciting at the middle of each frame (Figure 20h) allowed d in Δt = 9.1 ms time windows to be extracted between consecutive frames. Fitting the d distributions obtained under the two excitation schemes to a modified 2D random-walk model[73] (Materials and methods) gave similar typical diffusion coefficients of ~2.2 μm^2/s for cell plasma membranes (Figure 20gh), comparable to that previously measured by SPT for other lipophilic dyes.[119,164]

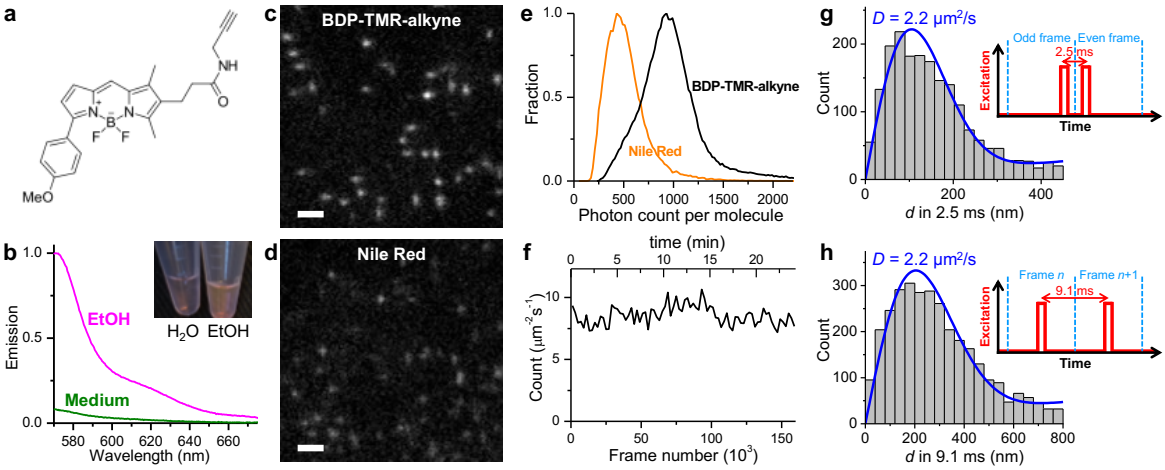

Figure 20: BDP-TMR-alkyne for stroboscopic PAINT and SM*d*M of cellular membranes. (a) Chemical structure of BDP-TMR-alkyne. (b) Fluorescence emission spectra of 3.3 nM BDP-TMR-

alkyne in the aqueous cell medium (green curve) vs. in ethanol (magenta curve), when excited at 560 nm. Inset: photo of 10 μM solutions of BDP-TMR-alkyne in water vs. in ethanol. (c,d) Typical single-molecule images of BDP-TMR-alkyne (c) vs. Nile Red (d) in cell membranes recorded under identical conditions with stroboscopic excitation pulses of τ = 1 ms duration. A cylindrical lens was applied to introduce image elongations in vertical or horizontal directions for molecules of different depths. (e) Distribution of single-molecule photon counts for the two cases. (f) Time-dependent count of the detected BDP-TMR-alkyne single molecules per μm^2 per second at the plasma membrane of a COS-7 cell, showing no noticeable drop over 1.6×10^5 frames (24 min at 110 fps). (g,h) Typical distributions of transient single-molecule displacement d of BDP-TMR-alkyne at the COS-7 cell plasma membrane under two stroboscopic excitation schemes (insets): repeated tandem excitation pulses at a Δt = 2.5 ms center-to-center separation (g), vs. excitation at the middle of every frame at 110 fps (Δt = 9.1 ms) (h). Blue curves: MLE (maximum likelihood estimation) fits to our model, with resultant diffusion coefficient D labeled. Scale bars: 2 μm (c,d).

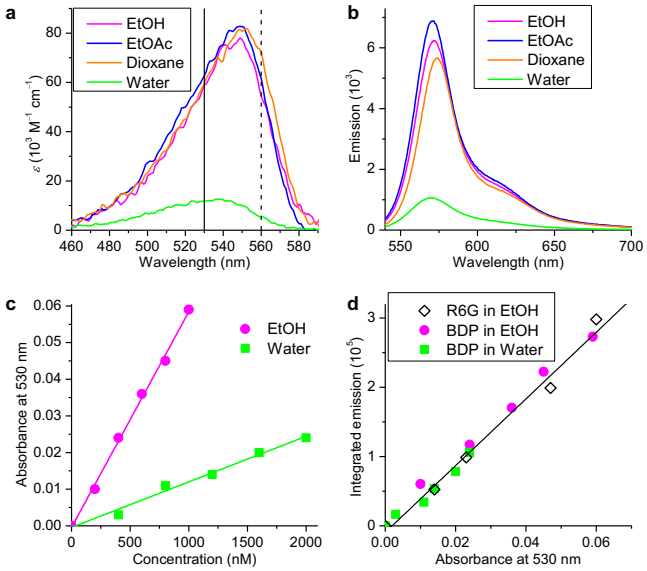

Figure 21: Spectral properties of BDP-TMR-alkyne in different solvents. (a) Absorption spectra of 1 μM BDP-TMR-alkyne in different solvents. Comparable results are found for three organic solvents of varying chemical polarities (ethanol, ethyl acetate, and 1,4-dioxane), yet the absorption in water is noticeably reduced and blue-shifted. The solid and dashed vertical lines correspond to excitation wavelengths used to determine quantum yields below (530 nm), and used in our single-molecule experiments and Figure 20b (560 nm), respectively. (b) Fluorescence emission spectra of 1 μM BDP-TMR-alkyne in different solvents when excited at 530 nm, showing comparable results between the three organic solvents but much lower emission in water. (c) Absorbance of BDP-TMR-alkyne at 530 nm as a function of concentration, in ethanol vs. in water. Lines: linear fits to data. (d) Emission as a function of absorbance at 530 nm, for BDP-TMR-alkyne of varied concentrations in ethanol vs. in water [same absorbance values as shown in (c)], in comparison to that of Rhodamine 6G (R6G) in ethanol. Line: a linear fit to the R6G data. Similar emission-absorbance trends are found for all three systems, indicating that the fluorescence quantum yields (QY) of BDP-TMR-alkyne in ethanol and in water are both comparable to that of R6G in ethanol, which has a known QY of 95%.[165] Thus, the substantially reduced fluorescence emission of BDP-TMR-alkyne in the aqueous phase under 560 nm excitation (Figure 20b) is due to reduced and blue-shifted absorption, rather than due to a significant change in QY. Meanwhile, the measured

higher QY (~95%) and extinction coefficients [ε~80,000 $M^{-1}cm^{-1}$ from (a)] of BDP-TMR-alkyne in organic solvents when compared to Nile Red[34,166] (QY~50-80% and ε~38,000 $M^{-1}cm^{-1}$) justify its superior single-molecule photon counts in cellular membranes.

The possibility to accumulate a large amount of single-molecule data through stroboscopic PAINT of BODIPY-TMR-alkyne enabled continuous fine-mapping of membrane topography and diffusivity. Resultant 3D-SMLM images (Figure 22ab) well resolved how the dorsal (top) plasma membrane raised out of the focal range when far away from the cell edge, as well as how the intracellular organelle membranes, *e.g.*, that of the ER, undulated in height and possibly contacted the plasma membrane (arrowheads in Figure 22b). The ventral (bottom) plasma membrane was lowly labeled owing to its inaccessibility to the probe-containing medium, similar to our observations for other PAINT probes.[37,167] Meanwhile, spatially binning the accumulated transient single-molecule displacement *d* into 100×100 nm^2 bins enabled their individual fitting[73] (Materials and methods) to obtain the local diffusivity *D*, hence color-coded SM*d*M super-resolution maps (Figure 22c). Typical *D* values of 2.0-2.5 $\mu m^2/s$ were thus found for the plasma membrane. Treating the cell with CTB, a cross-linker of the ganglioside GM1, gave rise to ~200 nm-sized nanodomains of substantially reduced local diffusivity down to ~1 $\mu m^2/s$ (Figure 22e), which partially co-localized with CTB (arrows in Figure 22de). This result echoes our recent SR-SMLM results with Nile Red, which showed that CTB induces similarly-sized nanodomains of low chemical polarity in the plasma membrane, attributable to increased lipid packing order due to the local sequestration of GM1 and cholesterol.[37] Cholesterol-induced packing order and reduced membrane fluidity are well documented at the bulk level.[168–171]

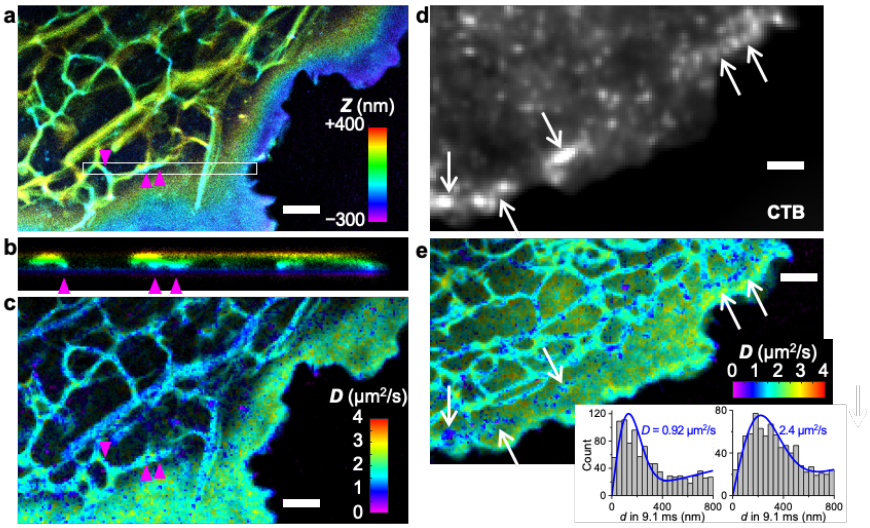

Figure 22: Concurrent 3D-SMLM and SM*d*M diffusion mapping of cellular membranes through stroboscopic PAINT of BDP-TMR-alkyne. (a) 3D-SMLM image obtained in a live COS-7 cell. Color presents depth (*z*); purple/blue: closest to the coverslip; red/yellow: farthest away. (b) Cross-sectional view along the box in (a) in the *xz* direction. Arrowheads point to possible contacts between ER and the ventral plasma membrane. (c) SM*d*M diffusivity map constructed from the same single-molecule data. Color presents local diffusivity *D*. (d) Epifluorescence image of dye-tagged CTB applied to another COS-7 cell. (e) BDP-TMR-alkyne SM*d*M diffusivity map of the same cell. Insets: typical distributions of single-molecule displacements for the low-diffusivity nanodomains (left) versus other parts of the plasma membrane (right), and their MLE fits for *D*

(blue curves). For both cells, stroboscopic excitation of $\tau = 1$ ms duration was applied at the middle of every frame at 110 fps ($\Delta t = 9.1$ ms). Scale bars: 2 μm.

For the ER-tubule membrane, typical D values appeared slightly lower than the plasma membrane (Figure 22ce), apparently against trend with their lower cholesterol level and packing order.[33,37,101] 2D plotting of single-molecule displacements showed a preferred angular distribution along the tubule (Figure 23a), indicating the isotropic 2D fitting model we originally used unsuitable. This observation underscores a geometrical effect that underestimates motion perpendicular to the tubule length: in the extreme case, a molecule that traveled a round trip along the tubule circumference in Δt would give a zero displacement.

We reason that the true diffusivity may still be obtained by examining displacements along the tubule. To this end, we started by determining the local displacement anisotropy α and principal direction θ (Figure 23a; Materials and methods). Projecting single-molecule displacements along and perpendicular to θ gave contrasting distributions: the former (Figure 23b) represents nonrestraint diffusion along the tubule, which could be fitted to a modified 1D random-walk model (Materials and methods) to extract a D value (Figure 23b), whereas the latter (Figure 23c) is convolved with tubule width. In comparison, displacements at the plasma membrane were isotropic (Figure 23d), and comparable D values were obtained when the 1D diffusion model was applied to projections along and perpendicular to the near-arbitrarily defined θ (Figure 23ef). Applying the above analysis to every spatial bin showed well-defined directional preferences along ER tubules in the resultant θ-α color maps (Figure 23g). Projecting the single-molecule displacements in each bin along its θ direction next enabled their individual fitting to the 1D diffusion model.

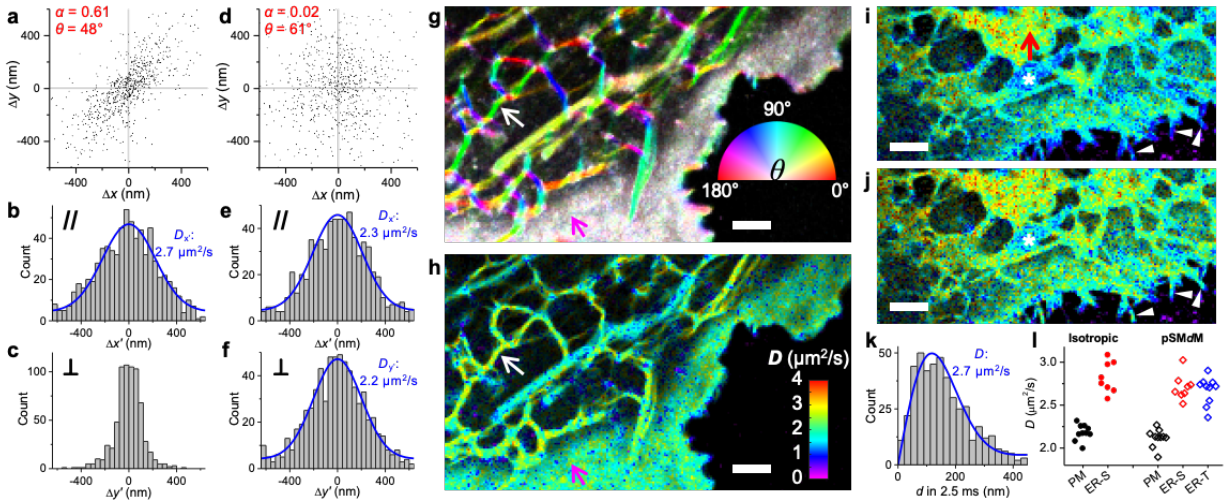

Figure 23: Principal-direction SM*d*M (pSM*d*M) analysis. (a) 2D plot of single-molecule displacements in $\Delta t = 9.1$ ms for BDP-TMR-alkyne at an ER tubule [white arrows in (g,h)]. A principal direction θ of 48° is calculated with an anisotropy α of 0.61. (b,c) 1D distributions of the displacements in (a) projected along (b) and perpendicular (c) to θ. Blue curve in (b): MLE fit to an 1D diffusion model with resultant $D = 2.7$ μm^2/s. (d) 2D plot of single-molecule displacements in $\Delta t = 9.1$ ms for BDP-TMR-alkyne at the plasma membrane [magenta arrows in (g,h)]. $\alpha = 0.02$ and $\theta = 61°$. (e,f) 1D distributions of the displacements in (d) projected along (e) and perpendicular (f) to θ. Blue curves: MLE fits to a 1D diffusion model, with resultant $D = 2.3$ and 2.2 μm^2/s. (g)

Color map presenting the calculated local θ (hue; inset color wheel) and α (color saturation; range 0-0.5) for the same region as Figure 2c. (h) pSM*d*M diffusivity map based on 1D diffusion fits along local principal directions. (i,j) SM*d*M (i) and pSM*d*M (j) diffusivity maps of another cell, acquired with tandem excitation pulses at Δt = 2.5 ms center-to-center separation, and presented on the same D color scale as (h). Asterisks mark a mitochondrion, for which D values are underestimated. (k) Distribution of single-molecule displacements in Δt for a region in the ER sheet [red arrow in (i)]. Blue curve: MLE fit, yielding D = 2.7 μm^2/s. (l) Statistics for D values in the two samples obtained with isotropic SM*d*M (filled circles) and pSM*d*M (open diamonds). Each data point corresponds to an ~0.15 μm^2 area containing signals solely from the plasma membrane (black), an ER sheet (red), or an ER tubule (blue). Scale bars: 2 μm (g,h,i,j).

Resultant principal-direction SM*d*M (pSM*d*M) diffusivity maps (Figure 23h) showed D values higher in the ER-tubule membrane (~2.7 μm^2/s; Figure 23b for typical 1D distribution of projected displacements) than in the plasma membrane (~2.2 μm^2/s; Figure 23ef for typical 1D distributions of projected displacements), in line with their expected lower lipid packing order and hence possibly higher fluidity. To further substantiate this finding, we next compared results on 2D ER sheets, which we observed in a small fraction of the cells. Isotropic SM*d*M (Figure 23i; see Figure 23k for typical distribution of single-molecule displacements) and pSM*d*M (Figure 23j) both showed typical D values of ~2.7 μm^2/s (Figure 23l), comparable to the pSM*d*M results above on the 1D ER tubules, yet substantially higher than the isotropic SM*d*M and pSM*d*M results on the plasma membrane (both at ~2.2 μm^2/s; Figure 23l). Together, these results indicate significantly higher diffusivity in the ER membrane when compared to the plasma membrane. Separately, for the occasionally observed thin cell protrusions, pSM*d*M helped recover D values comparable to the typical plasma membrane, when isotropic SM*d*M yielded artificially reduced D due to the 1D geometry (white arrowheads in Figure 23ij). pSM*d*M, however, did not overcome the complex, cristae geometry of mitochondrial membranes, for which D values were still underestimated (*e.g.*, marked by asterisks in Figure 23ij), awaiting future investigations.

Closer examination of both the isotropic and principal-direction SM*d*M data showed the ER diffusivity sporadically exhibit local reductions in D, often at tubule junctions and termini close to the plasma membrane (Figures 21, 22). To examine the possibility that these low-diffusivity foci corresponded to ER-plasma membrane (ER-PM) contact sites,[172–174] we expressed in the cells green fluorescent protein (GFP)-tagged GRAMD1a or GRAMD2a, which localizes to a subset of the EP-PM contacts.[175] 3D-SMLM through immunolabeling GFP in fixed cells showed GRAMD2a as ~100–500 nm patches at both the dorsal and ventral plasma membranes (Figure 24ab), often of slightly elongated shapes and occasionally with hollow centers (arrowheads). GRAMD1a similarly appeared as nanoscale patches, but with somewhat higher structural heterogeneities (Figure 24c).

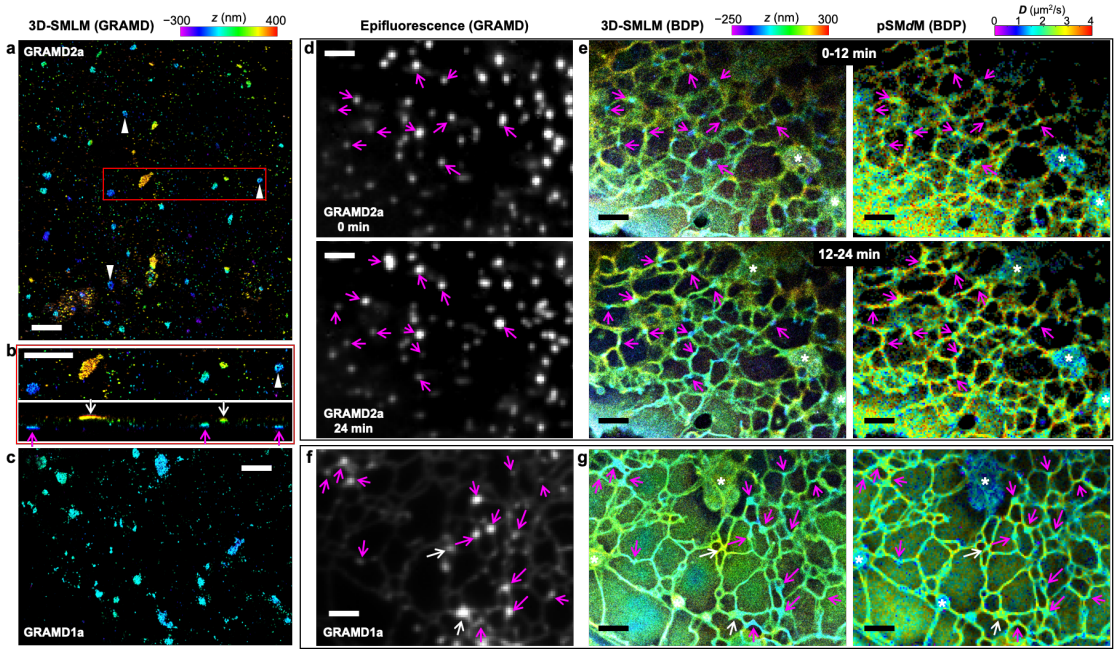

Figure 24: Concurrent SM*d*M and 3D-SMLM, together with fluorescent protein markers, indicate reduced membrane diffusivity at ER-PM contact sites. (a) 3D-SMLM image of immunolabeled GRAMD1a-GFP expressed in a COS-7 cell. Color presents depth (color scale on the top). (b) Zoom-in of the red box in (a) (top) and its vertical view in the *xz* direction (bottom). Magenta and white arrows point to apparent contact sites at the ventral and dorsal plasma membranes, respectively. (c) 3D-SMLM image of immunolabeled GRAMD1a-GFP at the ventral plasma membrane of another COS-7 cell. (d) Live-cell epifluorescence images of GRAMD2a-GFP expressed in a COS-7 cell, taken before (top) and after (bottom) stroboscopic PAINT of BDP-TMR-alkyne. (e) 3D-SMLM (left) and pSM*d*M (right) images (separate color scales on the top) of the same region via stroboscopic PAINT of BDP-TMR-alkyne, for two consecutive 12-min periods. Data were acquired with tandem excitation pulses of τ = 1 ms duration at Δt = 2.5 ms. Arrows in (d,e) point to example GRAMD2a-positive ER-PM contacts. Asterisks mark mitochondria. (f) Epifluorescence image of GRAMD1a-GFP expressed in another live COS-7 cell. (g) 3D-SMLM (left) and pSM*d*M (right) images of BDP-TMR-alkyne of the same region. Data were acquired with excitation pulses of τ = 1 ms duration at the middle of each frame at Δt = 9.1 ms. Magenta and white arrows in (f,g) point to example GRAMD1a-positive contact sites at the ventral and dorsal membranes, respectively. Scale bars: 2 μm.

To co-visualize these EP-PM contact site markers with membrane topography and diffusivity in live cells, we recorded epifluorescence images of GRAMD2a-GFP both before and after a long stroboscopic PAINT recording of BDP-TMR-alkyne over 24 min (Figure 24d). The single-molecule data were divided into two image stacks for the 0-12 min and 12-24 min periods, and each processed into matching 3D-SMLM and pSM*d*M images (Figure 24e). We thus found the GRAMD2a-GFP foci before and after the single-molecule recording separately matched the first and second 3D-SMLM images for ER tubule junctions/termini of low *z* values (arrows), indicative of contacts to the ventral plasma membrane. Notably, the concurrently obtained SM*d*M images showed substantially (~30%) reduced *D* at the same sites (Figure 24e), thus indicating that the ER-PM contacts maintained locally reduced membrane diffusivity as they reorganized in the live cell. In a different experiment on a thinner cell, GRAMD1a-GFP labeling (Figure 24f) and 3D-SMLM

(Figure 24g) helped identify ER-PM contact sites at both the ventral (magenta arrows) and dorsal (white arrows) plasma membranes, and SM*d*M indicated similar diffusion slowdowns for both cases (Figure 24g).

To understand whether the observed diffusion slowdown at ER-PM contact sites could be related to changes in the lipid packing order as we showed above for the CTB treatment, we next integrated SM*d*M with SR-SMLM[38,60] using the solvatochromic membrane probe Nile Red, which detects variations in lipid packing order through shifts in emission spectrum due to changes in the membrane chemical polarity.[33,37,38] Although the lower single-molecule brightness of Nile Red (Figure 20de) was not optimal for 3D localization, it worked well for SM*d*M with stroboscopic excitation pulses of τ = 2 ms duration (Figure 25a). Reduced local diffusivity was thus similarly observed at ER-PM contact sites marked by GRAMD2a-GFP (Figure 25c). Meanwhile, the collected single-molecule emission spectra at these sites were identical to adjacent ER regions (Figure 25bd), indicating no significant changes in the local lipid order.[37,38] In comparison, markedly bluer emission was observed for the plasma membrane (Figure 25bd) accompanying its lower diffusion rate, as expected from cholesterol-associated packing order.[33,37] The ER-PM contact sites are characterized by a wealth of trans-ER-membrane proteins that interact with plasma-membrane components to achieve key functions as lipid exchange and Ca^{2+} regulation,[172–174] and electron microscopy indicates high protein densities.[176,177] It is thus possible that macromolecular crowding in the ER membrane could create a maze that impedes diffusion[178–181] without altering the local lipid packing order.

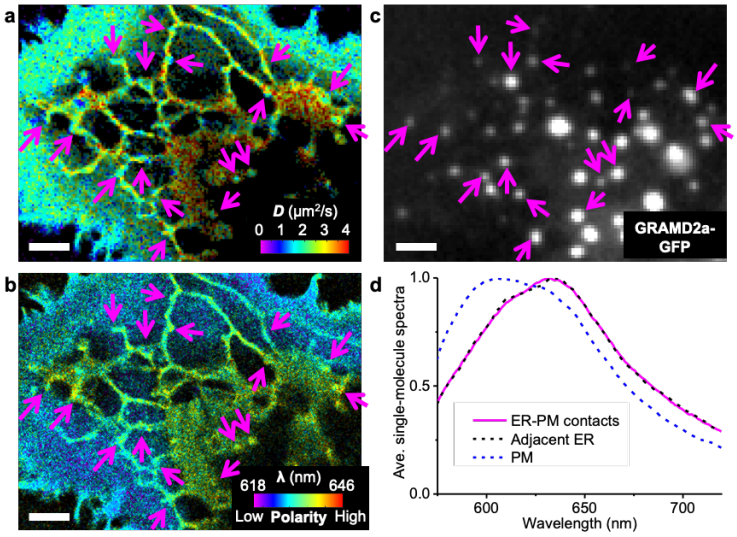

Figure 25: Concurrent SM*d*M and SR-SMLM of Nile Red indicate that the reduced diffusivity at ER-PM contacts is not associated with significant changes in lipid order. (a,b) Concurrently acquired pSM*d*M (a; color presents local diffusivity) and SR-SMLM (b; color presents the spectral mean of locally accumulated single molecules) images of Nile Red in a live COS-7 cell. Data were acquired with tandem excitation pulses of τ = 2 ms duration at Δt = 2.5 ms. (c) Epifluorescence image of GRAMD2a-GFP expressed in this cell. Arrows point to example GRAMD2a-positive ER-PM contact sites where substantial reductions in D are noticed in the pSM*d*M image. (d) Averaged local single-molecule spectra at the ER-PM contacts (magenta line) vs. adjacent ER regions (black dashed line), as well as at the plasma membrane (blue dashed line). Scale bars: 2 μm (a-c).

Although SPT has been valuable in probing diffusion at the nanoscale, its starting point is often to obtain long single-particle trajectories to enable their individual fitting to diffusion models. In contrast, SM*d*M focuses on examining, for every fixed location, how different (yet identical) molecules move within short time windows, with the explicit goal for a continuous, 2D spatial map of local diffusivity. The need to only detect single molecules in short time windows permits the use of probes that only emit transiently, yet at the same time, to obtain good local statistics demands high counts of single molecules. In this work, we thus started by identifying a new probe, BDP-TMR-alkyne, that exhibited excellent fluorescence turn-on and bright emission in the membrane phase while also enabling sustained stroboscopic PAINT experiments over long periods. High densities of single-molecule positions and displacements were thus obtained to achieve nanoscale fine-mapping of membrane topography and diffusivity. While not yet explored in this study, the alkyne functional group of this probe may be further utilized, *e.g.*, click-reactions to specific lipids.

The resultant high-resolution diffusivity maps first resolved locally reduced *D* in CTB-induced nanodomains in the plasma membrane, a result echoing our recent SR-SMLM observation of locally reduced chemical polarities due to CTB-sequestrated GM1 and cholesterol.[37] Whereas by globally altering the cholesterol level, previous work has examined how cholesterol-induced packing order reduces the fluidity of both cell and model membranes at the bulk level,[168–171] SM*d*M helped unveil this effect locally for the nanoscale, presumably more orderly packed phases induced by CTB.

The apparent dependency of diffusivity on the local cholesterol level next prompted us to scrutinize diffusivity in the ER membrane, where a lower cholesterol level and packing order are expected when compared to the plasma membrane. We thus identified a geometrical effect that led to the underestimation of *D* in 1D structures like ER tubules, and devised a new data analysis framework, pSM*d*M, to overcome this issue by projecting single-molecule displacements along local principal directions. By fitting the projected displacements to a modified 1D random-walk model, we thus obtained comparable *D* values for the 1D ER tubules and the occasionally observed 2D ER sheets, while also showing them to be substantially higher than the plasma membrane of the same cells. Together with the CTB results above, we thus determined a trend that the membrane diffusivity drops with increased lipid packing order.

Combining the *D* mapping capability of SM*d*M with 3D localization while further incorporating specific fluorescent protein markers, we next unveiled reduced diffusivity in the ER membrane at ER-PM contact sites. By next integrating SR-SMLM, we showed that this effect was not due to altered local lipid order, hence implicating protein crowding as a possible source of the diffusion slowdown. Experimental work on cells and model lipid bilayers, together with theory, has well addressed how protein crowding impedes membrane diffusion at the bulk level. However, as previous diffusion measurements offer limited mapping capabilities, how such effects might *locally* modulate membrane diffusivity remains elusive. By offering fine maps of local diffusivity, SM*d*M unveiled local diffusion slowdowns at the ER-PM contact sites, consistent with their high protein densities observed in electron microscopy. Such effects may help stabilize the contact sites and assist material exchanges between the ER and the plasma membrane, the potential consequences of which call for future experimental and theoretical investigations. Meanwhile,

future SM*d*M and SR-SMLM studies would benefit from solvatochromic membrane probes that specifically label either the plasma membrane or the ER membrane alone.

Together, as a timely integration of emerging modes of functional single-molecule and super-resolution approaches,[36] our work thus unveiled and differentiated between nanoscale diffusional heterogeneities of different origins in live-cell membranes.

5.3 Conclusion

The work in this chapter demonstrates the usefulness of multiplexed f-SRM in resolving the mechanism of physicochemical heterogeneities in the cell. By combining more detection modalities, e.g., emission spectrum with fluorescence lifetime or anisotropy, more functional properties can be mapped and their mechanisms elucidated using f-SRM.

5.4 Materials and methods

Dye characterization
BDP-TMR-alkyne (A24B0, Lumiprobe) was prepared as a 1 mM stock solution in DMSO, and diluted to 0.2-1.0 μM in different solvents for absorbance and fluorescence quantum-yield measurements (Figure 21), and 3.3 nM in ethanol or the cell imaging buffer (below) for fluorescence measurements under conditions comparable to the single-molecule experiments (Figure 20b). For measurement of quantum yield, Rhodamine 6G (252433, Sigma-Aldrich) was diluted to 0.2-1.0 μM in ethanol as the standard, for its well-characterized quantum yield of 95% under 530-nm excitation.[165] Fluorescence emission was recorded using a Duetta spectrometer (HORIBA Instruments), with excitation at 530 nm (Figure 21bd) or 560 nm (Figure 20b). Absorption spectra were recorded using the same cuvettes on a NanoDrop 2000c spectrometer (Thermo Fisher) in the cuvette mode, with background subtraction at 750 nm.

Cell culture
COS-7 cells (University of California Berkeley Cell Culture Facility) were maintained in Dulbecco's Modified Eagle Medium supplemented with 10% fetal bovine serum and 1% non-essential amino acids. Two days prior to imaging, cells were plated onto 18-mm diameter glass coverslips that were pretreated with hot piranha solutions (H_2SO_4:H_2O_2 at 3:1). Transfection of GRAMD1a-AcGFP and GRAMD2a-AcGFP (kind gifts from Prof. Jodi Nunnari[175]) was performed one day after plating. 300-500 ng plasmid was used per sample with the standard Lipofectamine 3000 protocol (Thermo Fisher). Before imaging, the coverslip was transferred to a holder (CSC-18, Bioscience Tools) compatible with the microscope stage. Imaging medium was Leibovitz's L-15 or a MOPS-based buffer (Hibernate A Low Fluorescence, BrainBits), with similar results observed. BDP-TMR-alkyne or Nile Red (Acros Organics) was diluted into the imaging medium to a final concentration of 3.3 nM. The dye-added imaging medium was added to the sample and remained unchanged throughout imaging. For CTB treatment, cells were incubated with 1 μg/mL Alexa Fluor 488-conjugated CTB (C34775, Invitrogen) in the culture medium for ~5 min, and then washed twice with the imaging medium before imaging.

Concurrent SM*d*M and 3D-SMLM

Concurrent SM*d*M and 3D-SMLM of BDP-TMR-alkyne was achieved *via* a homebuilt system based on a Nikon Eclipse Ti-E inverted optical microscope. Lasers at 488, 560, and 647 nm were independently modulated by an acousto-optic tunable filter (97-03151-01, Gooch & Housego) that was driven by an 8-channel RF synthesizer (97-03926-12, Gooch & Housego). The modulated laser beams were focused onto the back focal plane of an oil-immersion objective lens (Nikon CFI Plan Apochromat λ 100x, numerical aperture: 1.45) toward the edge, thus entering the sample slightly below the critical angle to illuminate a ~1 μm depth. For 3D localization, a cylindrical lens was used to induce elongations of single-molecule images in the vertical and horizontal directions for molecules below and above the focal plane, respectively.[125] The focal plane was set ~200 nm into the sample, so that depth (z) values of ~−200 nm corresponded to the substrate. Single-molecule images due to the transient entrance of individual BDP-TMR-alkyne molecules into the membrane phase[18] were continuously recorded in the wide-field using an EM-CCD camera (iXon Ultra 897, Andor) at a fixed frame rate of 110 fps. A multifunction I/O board (PCI-6733, National Instruments) read the camera exposure timing signal, and accordingly modulated the RF synthesizer to achieve frame-synchronized stroboscopic excitation for the 560 nm laser in two modes. In the first mode, paired pulses of τ = ~1 ms duration and Δt = 2.5 ms center-to-center separation were repeatedly applied across tandem camera frames (Figure 1g inset), so that single-molecule images from the paired odd-even frames captured transient displacements in the Δt time window.[73] In the second mode, pulses of τ = 0.5-2 ms duration were applied at the middle of each frame (Figure 20h inset). Single-molecule displacements were thus assessed between consecutive frames for Δt = 9.1 ms displacement time. The estimated peak and average power densities of the excitation laser at the sample were ~10 and ~1 kW/cm^2, respectively. 90,000-160,000 frames of single-molecule images were recorded under the above stroboscopic excitation schemes, from which 10^6–10^7 molecules were accumulated across the view. The 488 nm laser was separately applied before and/or after the above stroboscopic single-molecule experiments for epifluorescence imaging of AF488-tagged CTB and GFP-tagged GRAMD1a and GRAMD2a.

Concurrent SM*d*M and SR-SMLM

Concurrent SM*d*M and SR-SMLM of Nile Red were achieved on another homebuilt system as described previously.[37,73] Briefly, frame-synchronized stroboscopic excitation was achieved through direct power modulation of the 561 nm laser (OBIS 561 LS, Coherent) using a multifunction I/O board (PCI-6733, National Instruments). Paired pulses of τ = 2 ms duration and Δt = 2.5 ms center-to-center separation were repeatedly applied across tandem camera frames for evaluation of single-molecule displacements from the paired odd-even frames. The estimated peak and average power densities of the excitation lasers at the sample were ~6 and ~1 kW/cm^2, respectively. Single-molecule emission due to the transient entrance of individual Nile Red molecules into the membrane phase was split 50:50 for the concurrent recording of the unmodified images and the dispersed emission spectra in the wide-field. An EM-CCD camera (iXon Ultra 897, Andor) recorded ~120,000 frames at 110 fps.

3D-SMLM of GRAMD1a and GRAMD2a

For 3D-SMLM of GRAMD1a-AcGFP and GRAMD2a-AcGFP, transfected cells were fixed by 3% paraformaldehyde and 0.1% glutaraldehyde in phosphate-buffered saline (PBS) for 20 min, followed by a 5-min wash with freshly prepared 0.1% $NaBH_4$ in PBS. The sample was washed 3 times with PBS, and immunolabeled with a mouse anti-GFP primary antibody (Invitrogen A11120) and an Alexa Fluor 647-labeled secondary antibody (Invitrogen A21236). The labeled samples

were imaged in a photoswitching buffer (100 mM Tris-HCl pH 7.5, 100 mM cysteamine, 5% glucose, 0.8 mg/mL glucose oxidase, and 40 μg/mL catalase) on the 3D-SMLM setup described above. ~50,000 frames of single-molecule images were recorded at 110 fps under continuous 647-nm excitation.

Data analysis

Single-molecule raw images were first localized and rendered into 3D-SMLM images as described.[17,125] SR-SMLM data were processed as described.[37,60] SM*d*M analysis under the isotropic diffusion model was performed as described.[73] Briefly, the accumulated single-molecule displacements were spatially binned into 100×100 nm^2 bins. The displacements in each spatial bin were then separately fitted to a modified isotropic 2D random-walk model with the probability distribution

$$P(r) = \frac{2r}{a}\exp(-\frac{r^2}{a}) + br \tag{5.1}$$

where r is the single-molecule displacement in the fixed time interval Δt, $a = 4D\Delta t$, and b is a background term to account for molecules that randomly enter the view, as rationalized and validated previously[73] with experiments carried out at different single-molecule densities. For the pSM*d*M analysis, for each spatial bin, we first calculated the angular coordinate φ of each single-molecule displacement accumulated in the bin. As we consider molecules traveling in opposite directions to be diffusing along the same axis, we first flipped all displacements with φ in the range of (-180°, 0°) by adding 180°, so that all the resultant φ' values were in the range of [0°, 180°]. We then took the circular mean of $2\varphi'$ (in the range of [0°, 360°]) for all displacements in the spatial bin, and divided this value by 2 to obtain the average direction of diffusion θ (principal direction). Anisotropy α is also assessed in the process by dividing the modulus of the vector sum (in the $2\varphi'$ angle space) over the sum of the moduli of all the displacements, hence a value of 0 and 1 for fully isotropic and fully anisotropic (bidirectional along a line) diffusions, respectively. Results at each spatial bin were converted into a color for color-map presentation (*e.g.*, Figure 23g) *via* the HSV (hue, saturation, value) color space, with hue, saturation, and value corresponding to θ, α, and single-molecule count, respectively. The single-molecule displacements in each bin were next separately projected along and perpendicular to the calculated θ direction (*e.g.*, Figure 23bcef) for fitting to a modified 1D random-walk model[73] with the probability distribution of $P(x) = \frac{1}{\sqrt{a\pi}}\exp(-\frac{x^2}{a}) + b'$, where $a = 4D\Delta t$. The larger resultant D value of the two was picked to generate pSM*d*M color maps.

Chapter 6: Future directions for f-SRM

The work in this chapter was conducted in collaboration with Bowen Wang and Ke Xu. It is reproduced in part here from Yan et al[36] with permission from all co-authors. Copyright 2019 Elsevier.

6.1 Introduction

In previous chapters, we described single-molecule-based f-SRM strategies harnessing the emission spectrum and diffusivity of dye molecules. In this chapter, we discuss emerging new possibilities to f-SRM by different super-resolution modalities and fluorescence readouts (Figure 26).

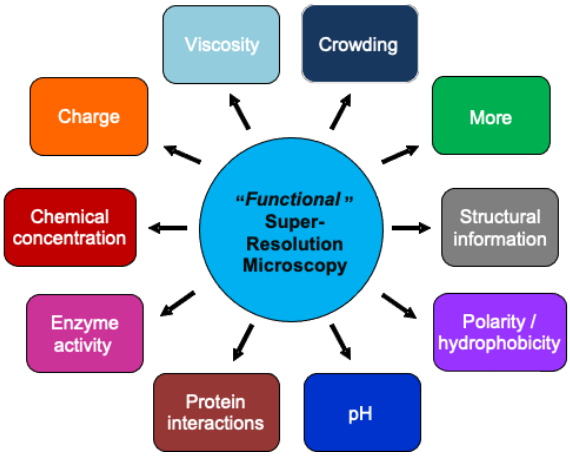

Figure 26: f-SRM explores the possibility to transcend the structural (shape) information offered by existing super-resolution methods and unveil multidimensional information of diverse intracellular functional parameters, like those shown in this diagram, with nanoscale spatial resolution and ultimate sensitivity down to single molecules.

Although multifunctional and multiparametric fluorescence microscopy, often enabled by environment-sensitive and chemical-responsive fluorescent probes,[33,35,114,182–184] long preceded the development of SRM, the relatively low spatial resolution (~300 nm) achieved with conventional, diffraction-limited microscopy limits how localized the microenvironments can be probed. As the probed volume scales cubically with the linear dimension, a 10-fold enhancement in spatial resolution, which is often achieved in SRM, could reduce the probed volume by 1,000 times, hence dramatic reduction of interference from the undesired surrounding signal when compared to the desired local signal. For SMLM-based techniques, the possibility to map local properties by examining the response of each probe molecule one at a time further represent the ultimate sensitivity, effectively removing the interferences between different molecules. The outstanding resolution and sensitivity thus offer exciting potential opportunities to uncover local functional information that would otherwise be averaged out with traditional approaches. Below we summarize emerging f-SRM efforts that start to demonstrate such possibilities, and we group our discussion by how the functional information is optically encoded.

6.2 Review of relevant work

Fluorescence intensity is conceivably one of the most straightforward parameters for encoding functional information. Indeed, many fluorescent reporters for chemical imaging are based on fluorescence turn-on.[33,35,114,183,184]

Mishina et al[185] adopted this strategy to visualize the concertation of H_2O_2 in live cells with STED SRM. By tagging HyPer2, a fluorescence turn-on fluorescent protein (FP) biosensor for H_2O_2, to the cytoskeleton, STED SRM images provided ~3-fold enhancement in spatial resolution when

compared to conventional confocal microscopy. Treatment of the cell with platelet-derived growth factor (PDGF), as well as with H_2O_2, led to modest and substantial increases in the STED-measured HyPer2 intensity (Figure 27a), respectively, attributable to corresponding rises in local intracellular H_2O_2 concentration. In a more sophisticated approach, Mo et al[186] developed biosensors based on the increased fluctuation in fluorescence intensity as two FPs were brought into proximity, and thus, through stochastic optical fluctuation imaging, showed sub-diffraction features of protein kinase A (PKA) activity on the cell plasma membrane.

Although the fluorescence intensity is easy to measure, its limitation for reporting functional information is also apparent. The detected intensity depends on the local concentration of the fluorescent probe, and so it is difficult to quantify for absolute values. Interpretation of time-dependent signal changes is further complicated by photobleaching, which could be significant for the strongly illuminated SRM experiments.

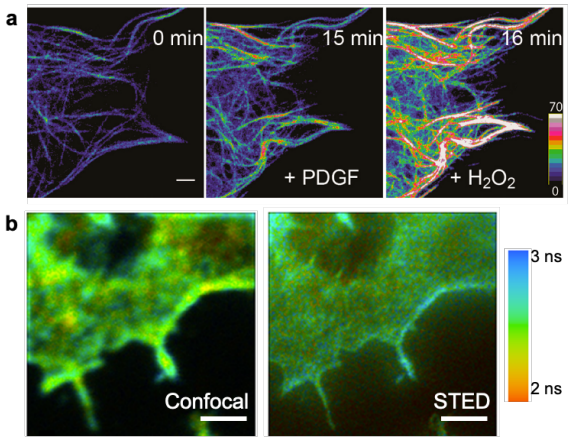

Figure 27: f-SRM through fluorescence intensity and lifetime detections. (a) STED images of EB3−HyPer2 fluorescence intensity change in an NIH 3T3 cell at indicated time points, after stimulation with 10 ng/mL PDGF and subsequent addition of 200 μM H2O2. (b) Comparison of confocal (left) and STED (right) fluorescence lifetime images of a fixed *Drosophila* S2 cell with Alexa Fluor 594-phalloidin-labeled actin. Scale bars: 2 μm. Panel (a) is adapted with permission from Mishina et al[185]. Panel (b) is adapted with permission from Lesoine et al[187].

Fluorescence-lifetime imaging microscopy (FLIM)[50] is a powerful, intensity-insensitive method for probing local environments. The exponential decay rate of fluorescence emission, typically on the time scale of nanoseconds, depends strongly on both the dye identity and dye-environment interactions, thus a valuable reporter.

For SRM, although FLIM has been successfully incorporated with STED,[187–190] the focus has been on the unmixing of different dyes into separate color channels for multi-target SRM.[189,190] Lesoine et al[187] examined Alexa Fluor 594-phalloidin-labeled actin cytoskeleton in fixed cells, and noticed varying local fluorescence lifetime in the STED image (Figure 27b), a result potentially consistent with varied quenching interactions between the tagged dye and the local components of the cell. However, as a rather Gaussian-like distribution was found for the measured lifetime at different locations, it was unclear if the observed local variations merely reflected statistical error.[187] Nonetheless, given the wide usage of FLIM for environment sensing,[50] lifetime-resolved SRM stands as a promising direction for future f-SRM efforts.

Fluorescence polarization and anisotropy measurements provide information on the orientation and rotational mobility of fluorescence molecules.[53] For SRM, polarization-resolved SMLM has been achieved by splitting the fluorescence into polarizations parallel and perpendicular to the excitation laser using either a polarizing beam splitter[191] or a Wollaston prism[192,193], and by modulating the polarization orientation of the excitation laser[194]. Gould et al[191] thus showed, through polarization FPALM, local heterogeneities in the fluorescence polarization anisotropy of overexpressed Dendra2-actin molecules in fixed fibroblasts. Cruz et al[192] performed polarization-resolved dSTORM and found certain, but not all, dyes conjugated to phalloidin exhibited restricted polarization orientations when labeled to actin stress fibers in fixed cells. For *in vitro* samples, polarization-resolved SMLM has also demonstrated preferred orientations for dyes labeled to DNA strands[192,194] and insulin amyloid fibrils[193]. Thus, polarization-resolved SRM provides orientation information of the tagged fluorophores, hence new structural, and potentially functional, insights.

Ratiometric detection is a commonly used, relatively simple strategy to detect the color changes of fluorescence probes. Here, a dichroic mirror splits the fluorescence into long- and short-wavelength components, respectively, and the relative intensities measured for the two components provide the spectral information.

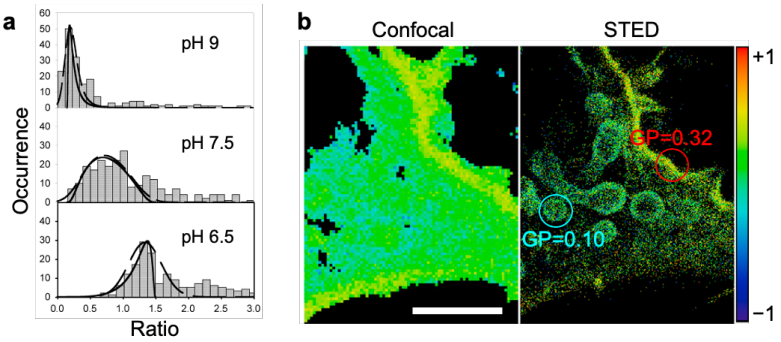

Figure 28: f-SRM through ratiometric color detection. (a) Histograms of the emission ratio R = I_{580nm} / I_{640nm}, I_{580nm} and I_{640nm} being the fluorescence intensities detected at 580 and 640 nm, respectively, for single SNARF-1-dextran molecules immobilized in agarose gels at different pH. (b) Ratiometric confocal and STED images of Di-4-AN(F)EPPTEA in a living CHO cell. Color denotes the generalized polarization (GP), $(I_1 - I_2)/(I_1 + I_2)$, where I_1 and I_2 are the fluorescence intensities detected in the 520-570 nm and 620-700 nm channels, respectively. Endocytic vesicles (blue circle) show smaller GP values than the plasma membrane (red circle). Scale bar: 500 nm. Panel (a) is adapted with permission from Brasselet and Moerner[81]. Panel (b) is adapted with permission from Sezgin et al[195].

For single-molecule imaging, Brasselet and Moerner[81] investigated the local pH in agarose gels by sparsely doping dextran molecules tagged with SNARF-1, a fluorescent pH indicator. The pH-dependent spectral shift was measured as the ratio of single-molecule emission between two wavelengths centered at 580 and 640 nm. Interestingly, although the mean values from single-molecule ensembles matched that of bulk measurements, histograms of emission ratios of individual molecules at different pH revealed more scattered distributions at intermediate pH (Figure 28a). This difference suggests higher spatial heterogeneity of protonation chemistry at

intermediate pH, which could not have been detected with ensemble measurements. Extending related approaches to SMLM-type SRM[83–85] and to cells represents future challenges.

For STED SRM, Sezgin et al[195] achieved ratiometric spectral detection for several polarity-sensitive, solvatochromic membrane probes. The 3-fold enhancement of spatial resolution over confocal microscopy was instrumental in revealing local polarity differences. In particular, for Di-4-AN(F)EPPTEA-labeled live cells, STED detected significantly smaller generalized polarization (GP) values, and thus reduced local molecular order, for endocytic vesicles near the plasma membrane, a nanoscale feature that was obscure under diffraction-limited confocal spectral imaging (Figure 28b). Together with the above-discussed STED-FLIM experiments, it appears f-SRM through combing environment-sensing dyes with STED could lead to great promises.

6.3 Outlook

In conclusion, f-SRM has emerged over the past few years as a new class of powerful methodologies to address the highly intriguing, yet highly challenging, functional aspects of cell biology at the nanoscale. Diverse physicochemical parameters have been examined, and numerous strategies have been invoked to encode the sought functions, in many cases prompting the development of new optical tools that access new dimensions of the SRM readout. We expect future work to expand on existing possibilities by both encoding untested new functions and by further exploring other possible dimensionalities of the SRM signal, including through correlated approaches that tap into the power of other microscopy and spectroscopy techniques.[196] Throughout such endeavors, the development and/or identification of suitable, environmentally sensitive fluorescent probes undoubtedly hold the key. Thus, the multifunctional and multidimensional approach of f-SRM relies on multidisciplinary efforts; its future success demands in-depth discussion and collaboration between researchers across diverse fields.

f-SRM for material chemistry

SRM, by virtue of its molecular resolution, is suitable for characterizing polymeric, supramolecular, or macromolecular structures.[197–199] However, due to historical reasons that SRM has been mainly developed by biophysicists, its application in chemistry lags far behind its popularity in biology. For structural characterization only, electron microscopy seems to be more advantageous than SRM given the higher spatial resolution and the label-free feature of the former. However, if one would like to interrogate the physicochemical properties of materials, instead of bulk spectroscopic methods, f-SRM could be useful to reveal spatial heterogeneities and correlate the measured properties with the spatial information of the sample.

Recently, there have been efforts applying f-SRM to material science questions, including some from our laboratory.[200–202] With environment-sensitive fluorophores, one can use SR-SMLM to map the property of interest in the sample at 10-100-nm spatial resolution. SM*d*M can provide the diffusional information of the sample, which could further reflect different characteristics of the composing material.

f-SRM for developmental biology

Although SRM has been widely used in cell biology, its use in developmental biology has been limited due to the size of sample.[203–206] Embryos and tissues are on the order of 100 μm to 1 mm

in all dimensions, making most classical SRM methods unavailable. Recent developments in light-sheet microscopy and multi-photon microscopy have diminished this inaccessibility issue,[207,208] and there have been a lot of new discoveries in developmental biology enabled by resolving the structures in embryos and tissues.

It would be more exciting to add other dimensions of information to these systems with f-SRM. It has been realized in recent years that proteins and RNAs are not the only determinants of embryonic development, whereas small-molecule metabolites[209], ions (especially H^+ and Ca^{2+})[210–212], and mechanical force[213–215] are also essential cues for various developmental processes. Mapping these properties *in situ* would unveil previously hidden factors that drive the morphogenesis of developmental patterns.

Part II: Microscopy-Driven Discovery of a Novel Trafficking Organelle

In this section, we will present new modalities of conventional, diffraction-limited microscopy for studying cell biology, which led to discoveries of unexpected phenomena of the cell. In Chapter 7, we demonstrate excitation spectrum-resolved wide-field microscopy enabling simultaneous imaging of 6 spectrally overlapped fluorophores in live cells with low crosstalk and high temporal resolution. The capability to quantify the abundances of different fluorophores through spectral unmixing further allows us to devise novel imaging schemes for bi-state and FRET (Förster resonance energy transfer) fluorescent biosensors in living cells. In Chapter 8, we employ live-cell, excitation-resolved microscopy to elucidate the biogenesis mechanism of a special organelle we named t-ERGIC (tubular ER-Golgi intermediate compartment), which facilitates ER-to-Golgi trafficking of soluble proteins that bind with the cargo receptor SURF4 through expansion of the ER exit sites due to protein phase separation.

Chapter 7: Excitation spectral microscopy for highly multiplexed fluorescence imaging and quantitative biosensing

The work in this chapter was conducted in collaboration with Kun Chen, Limin Xiang, and Ke Xu. It is reproduced in part here from Chen et al[216] with permission from all co-authors.

7.1 Introduction

The wide popularity of fluorescence microscopy in biological research[3,217] benefits greatly from its two distinct advantages, namely, target specificity and compatibility with live cells. Yet, both advantages connect to performance limits. For multi-target imaging, owing to the broad spectral width of molecular fluorescence, common approaches based on bandpass filters only accommodate 3-4 spectrally well-separated channels within the visible range. Meanwhile, the urge to image fast dynamics in live cells for multiple targets is often impeded by the slow mechanical switching between filter sets. Quantitative imaging of fluorescent biosensors,[218–221] for which the simultaneous monitoring of two or more spectral channels is often necessary, creates yet another level of challenge for fast imaging, and its integration with additional fluorescent markers is even more difficult.

Spectral imaging offers potential solutions to the above problems.[46,222,223] Although it is conceptually intuitive to detect the fluorescence emission spectrum, in practice, with common pixel array-based cameras, it remains difficult to record spatial and spectral information at the same time for the wide-field.[224,225] Consequently, spectrally resolved images are usually acquired in a point-scanning manner by dispersing the fluorescence from one single spot of the sample at a time. Alternatively, sparse single molecules may be spectrally dispersed in the wide-field to accumulate super-resolution images over many camera frames.[60,226] Both scenarios place substantial constraints on temporal resolution. Tunable bandpass filters provide a possibility to scan through the emission wavelength in the wide-field.[227] However, applying narrow bandpasses to the fluorescence emission results in inefficient use of the scarce signal. In addition, tunable thin-film filters are limited in speed with mechanical scanning,[228] whereas electronically tunable filters, *e.g.*, acousto-optic tunable filter (AOTF), only work for polarized light and introduce distortion to wide-field images.[229,230]

In contrast to the above challenges to resolve the fluorescence emission spectrum at every pixel, it is straightforward to scan the excitation wavelength for the entire imaging field while recording the resultant emission in a fixed passband, hence excitation wavelength-resolved images. Excitation spectral microscopy, however, is conceptually less intuitive and experimentally rarely explored,[222,231–233] especially for examining subcellular structural dynamics in live cells. A recent lattice light-sheet setup has imaged 6 subcellular targets using 6 excitation lasers that span the visible range.[234] However, even with large (~40 nm) spectral separations between the laser lines and between the fluorophore spectra, high (~50%) target-to-target crosstalks are observed.[234] The implementation of 6 lasers with associated notch filters is also technically demanding.

Here we show that using a standard epifluorescence microscope with a single emission band, through frame-synchronized fast scanning of the excitation wavelength from a white lamp at ~10 nm resolution, 6 subcellular targets, labeled by common fluorophores of substantial spectral

overlap, can be simultaneously imaged in live cells in the wide-field with low crosstalks and high spatiotemporal resolutions. The ability to unmix and quantify different fluorescent species in the same sample *via* the excitation spectrum next enables us to devise fast, quantitative imaging schemes for different modes of fluorescent biosensors in live cells, as well as their multiplexing with multiple additional fluorescent tags.

7.2 Results and discussion

7.2.1 Frame-synchronized AOTF scanning of the excitation wavelength

Light from a white lamp was collimated and linearly polarized before entering an AOTF (Figure 29a). The 1st order diffracted beam, with its wavelength and intensity controlled by a radio-frequency (RF) synthesizer and polarization orientation rotated by 90°,[230] was cleaned up with a second polarizer and then coupled into a commercial epifluorescence microscope as the excitation source using a conventional, single-band filter cube. Wide-field images collected from a high-NA oil-immersion objective were continuously recorded using an sCMOS or EM-CCD camera. A multifunction I/O device synchronized the RF synthesizer, so that for each successive frame, the excitation switched between 8 preset wavelength profiles that were ~10 nm apart from each other. The 8 profiles each had a bandwidth of 5-12 nm, and typical intensities were ~6 and ~27 μW for recording at 10 and >200 frames per second (fps), respectively. Full-frame excitation-spectral images were thus obtained every 8 camera frames (Figure 29b).

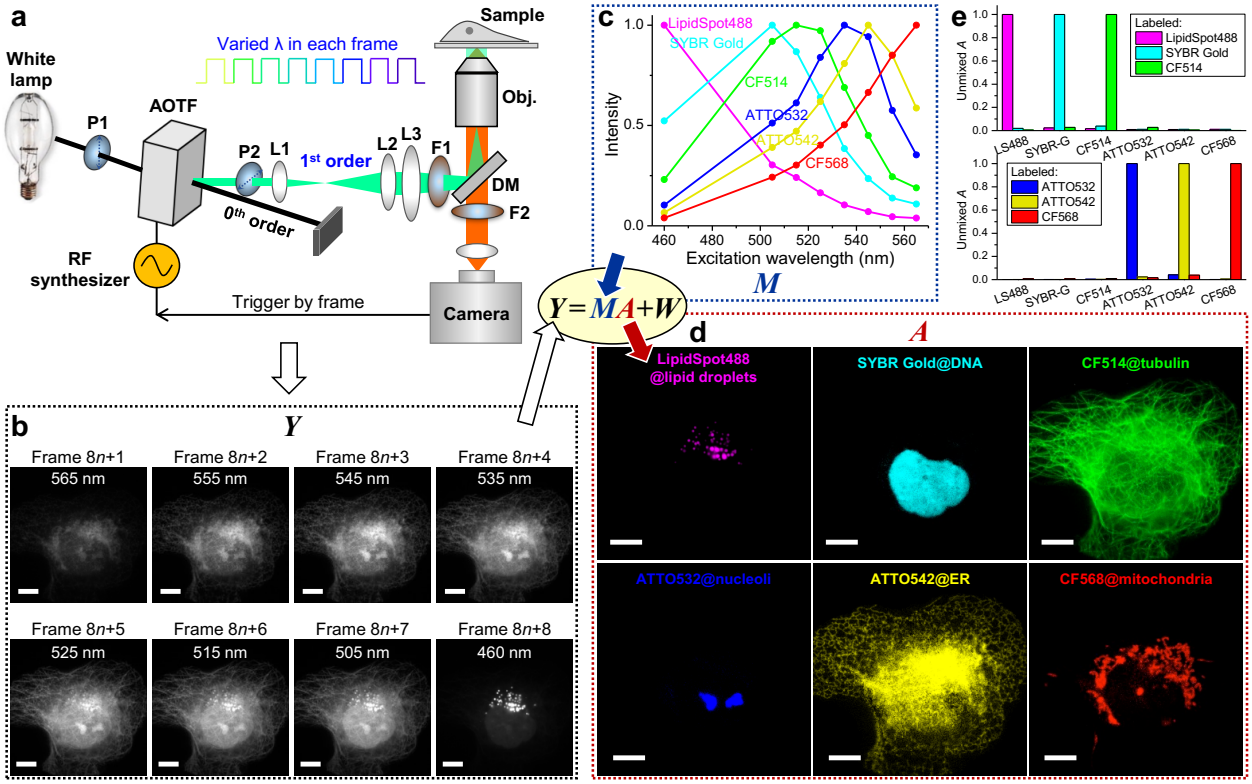

Figure 29: Excitation spectral microscopy. (a) Schematic of the setup. Full-frame spectral micrographs are obtained by the synchronized fast modulation of the excitation wavelength λ in consecutive frames. P, polarizer; L, lens; F, bandpass filter; DM, dichroic mirror. The resultant

excitation spectrum collected at every pixel (*Y*) is linearly unmixed into the abundances (*A*) of different fluorophores based on their pre-calibrated excitation spectrum (*M*) to minimize the residual (*W*). (b) Example images recorded at 8 preset excitation wavelengths in 8 consecutive frames at 10 fps (thus 0.8 s total data acquisition time), for a fixed COS-7 cell labeled by 6 fluorescent dyes for 6 distinct subcellular structures: LipidSpot 488 for lipid droplets, SYBR Gold for nuclear DNA, and CF514, ATTO 532, ATTO 542, and CF568 for immunofluorescence of tubulin, nucleoli, ER, and mitochondria, respectively. (c) Reference 8-wavelength excitation spectra of the 6 fluorophores, separately measured on our setup using singly labeled samples. (d) Decomposed images of the 6 fluorophores, obtained via linearly unmixing the excitation-dependent intensity at each pixel in (b) using the reference spectra in (c). (e) Unmixed abundancy values in different fluorophore channels for samples singly labeled by each of the 6 fluorophores. Scale bars: 10 μm (b, d).

7.2.2 Unmixing 6 fluorophores through the excitation spectrum

As each fluorophore is characterized by its own excitation spectrum, *i.e.*, a fixed profile of how the fluorescence intensity varies as a function of the excitation wavelength (Figure 29c), a sample region containing multiple fluorophores should exhibit an excitation spectrum that is a linear combination of that of its component fluorophores.[222] Thus, by linearly unmixing the above-recorded excitation spectrum of every pixel (*Y*) based on the excitation spectrum of each fluorophore (*M*) pre-calibrated on the same setup using singly labeled samples (Figure 29c), we quantified the local abundance (*A*) of each fluorophore. Rendering the resultant abundance in each pixel as an image thus yielded fluorophore-decomposed micrographs of the sample (Figure 29d).

Figure 29d shows the unmixed images of a fixed COS-7 cell, in which 6 distinct subcellular structures were labeled with 6 fluorescent dyes that overlapped substantially in the excitation spectrum (Figure 29c). Little crosstalk was observed between the 6 unmixed images (Figure 29d) with our 8-wavelength excitation scheme accomplished in 0.8 s (8 frames at 10 fps), even as the raw images at each wavelength (Figure 29b) contained substantial contributions from multiple fluorophores due to heavy spectral overlaps (Figure 29c). Forcing the same 6-fluorophore unmixing procedure onto samples singly labeled by each fluorophore showed an average crosstalk of 1.3% between fluorophores (Figure 29e).

7.2.3 Fast multi-target imaging of live cells

We next applied 8 excitation-wavelength spectral microscopy to live cells. With a combination of fluorescent protein (FP) tags and live-cell stains, 6 distinct subcellular targets were well unmixed (Figure 30a-c) at an averaged 1.3% target-to-target crosstalk. At a moderate camera framerate of 10 fps, a full-frame excitation-spectral image (and thus unmixed 6-target image) was obtained every 0.8 s. We thus visualized that in live COS-7 cells, lysosome and ER both marked the fission site of a mitochondrion (white arrows in Figure 30d), and that the mitochondrial DNA was also divided in this process, consistent with previous, separate observations.[235–237]

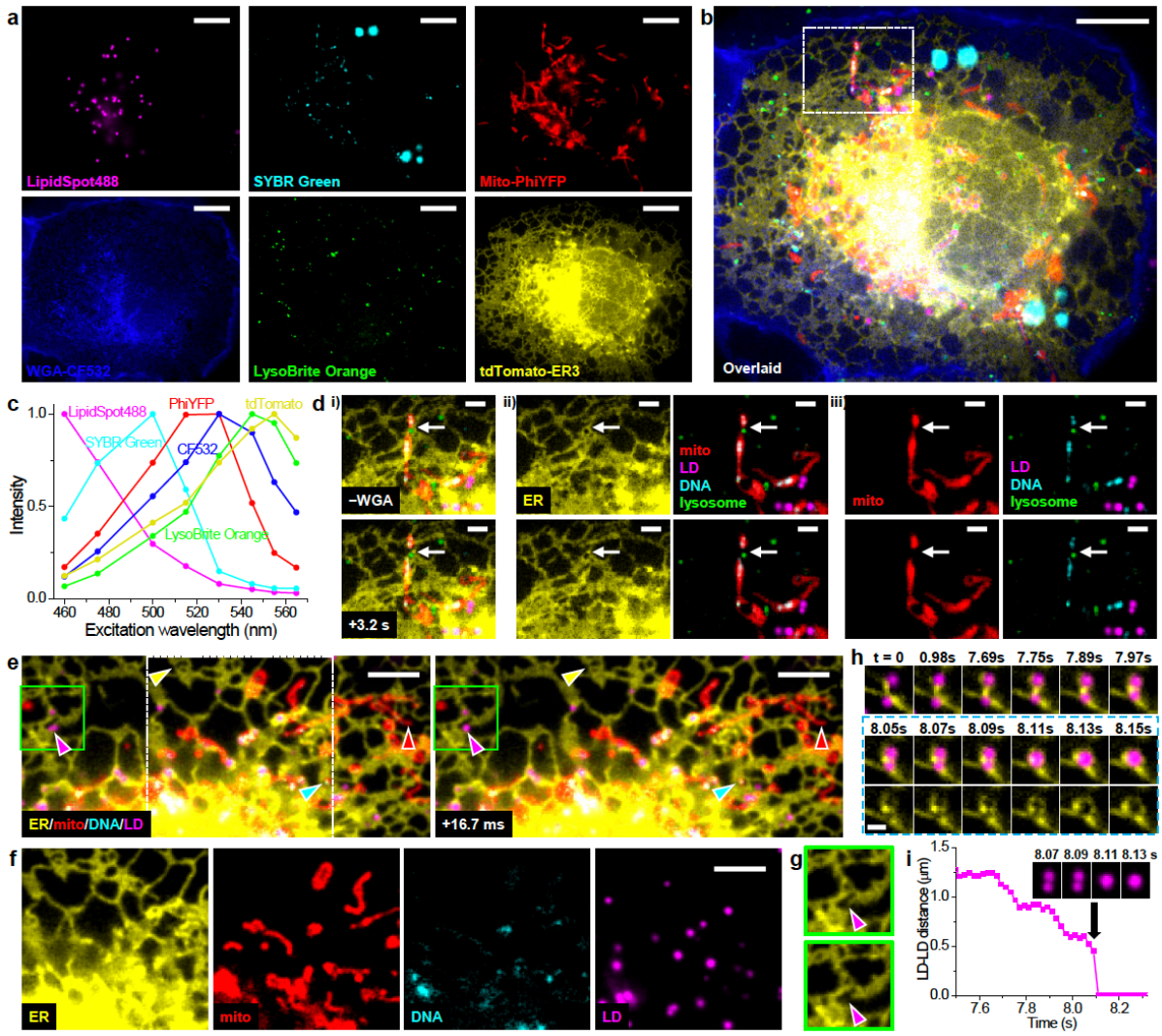

Figure 30: Fast multi-target imaging of live cells. (a) Unmixed images of 6 subcellular targets in a live COS-7 cell via 8-excitation-wavelength recording at 10 fps (0.8 s total data acquisition time). LipidSpot 488: lipid droplets (LDs), SYBR Green: mitochondrial DNA, Mito-PhiYFP: mitochondrial matrix, WGA-CF532: cell membrane, LysoBrite Orange: lysosomes, tdTomato-ER3: ER. (b) Overlay of the above 6 images. (c) Reference excitation spectra of the 6 fluorophores, separately measured on the setup using singly labeled samples. (d) The box region in (b) for two time points 3.2 s apart (top vs. bottom rows), after i) removing the WGA channel, ii) separation of the ER channel, and iii) further separation of the mitochondria channel. (e) Two consecutive 4-fluorophore images at 16.7 ms time spacing for another live COS-7 cell labeled by tdTomato-ER3, Mito-PhiYFP, SYBR Green, and LipidSpot 488, achieved by synchronizing 4-wavelength excitation with 240 fps recording. Yellow, red, cyan, and magenta arrowheads point to noticeable structural changes in each fluorophore channel. (f) The separated fluorophore channels for the white box in (e). (g) The ER channel for the green boxes in (e), at 16.7 ms separation. (h) ER-mediated LD fusion observed in another 4-wavelength experiment at 19.8 ms time spacing (202 fps recording). Bottom row: consecutive ER-LD and ER images during merging. (i) Distance between the two LDs as a function of time. Inset: four consecutive images of the LD channel. Scale bars: 10 μm (a, b); 2 μm (d); 5 μm (e, f); 1 μm (h).

For faster imaging, we next synchronized 4-wavelength excitation cycles with a 240-fps camera framerate (Materials and methods) to image 4 subcellular targets at 16.7 ms time spacing (Figure 30ef). This enabled us to simultaneously detect the fast structural changes of ER, mitochondria, mitochondrial DNA, and lipid droplets in the same field of view (color arrowheads in Figure 30e). In particular, the magenta arrowheads point to the fast fusion of two lipid droplets that occurred within the 16.7 ms timeframe, for which event we also observed associated fast retraction of ER (Figure 30g). In another 4-wavelength experiment performed at a 202 fps framerate (19.8 ms per spectral image), we recorded how an ER tubule first brought two lipid droplets closer in discrete, ~0.1 s steps, and then mediated their fusion through fast ER reorganization (Figure 30hi), a process substantially different from existing models.[238] Together, we have demonstrated, for both live and fixed cells, the power of excitation spectral microscopy for high-throughput multi-target imaging.

7.2.4 Absolute pH imaging in live cells via unmixing and quantifying two fluorescent species

We next harnessed our above capability to quantify spectrally overlapped fluorescent species to devise quantitative imaging schemes for fluorescent biosensors in live cells. A class of biosensors works on contrasting fluorescence properties between their analyte-bound and unbound states. The FP pHRed is such a bi-state sensor that exhibits distinct excitation spectra upon protonation and deprotonation.[239] Although this property has enabled ratiometric pH detection with two excitation wavelengths,[239,240] absolute pH mapping is usually not performed.

We achieved absolute pH mapping by quantifying the respective abundances of the protonated (HA) and deprotonated (A^-) species of pHRed at each pixel. To this end, we first recorded the excitation spectra of pHRed in proton-permeabilized cells at low (4.5) and high (11) pH extremes (Figure 31a, dash lines), under which conditions the FP should be in the pure HA and A^- states, respectively. We next similarly recorded excitation spectra in a series of buffers of pH = 6.5-9.5 (Figure 31a, solid lines). For each pH, the measured excitation spectrum (e.g., Figure 31b, solid line) was unmixed into that of the HA and A^- states (Figure 31b, dash lines). The resultant abundances at each pH (Figure 31c) fitted well to the simple Henderson-Hasselbalch equation based on thermodynamic equilibrium:

$$\mathrm{pH} = \mathrm{pH}_0 + \log\frac{[\mathrm{A}^-]}{[\mathrm{HA}]} \tag{7.1}$$

in which pH_0 is the only fitting parameter, and $[A^-]$ and [HA] are the abundances of the two states. From the fit we obtained $pH_0 = 7.87$, close to the apparent pK_a of pHRed (~7.8).[239]

This good fit to theory allowed us to image absolute pH in live cells by first unmixing the excitation spectrum at every pixel and then feeding the resultant HA and A^- abundances into Equation (7.1). Besides achieving high confidences for HA and A^- abundances and hence pH, this approach enabled us to readily incorporate additional fluorophores, as discussed below. For pHRed expressed in the cytoplasm, we observed homogenous pH of ~7.2-7.4 in common cell lines (Figure 31d). Meanwhile, Mito-pHRed in the mitochondrial matrix showed typical pH of ~7.7-8.1 (Figure 31d-g) in live cells while exhibiting sporadic, spontaneous jumps (Figure 31hi). Treating the cells with the uncoupler carbonyl cyanide *m*-chlorophenyl hydrazone (CCCP) led to fast drops of the mitochondrial matrix pH to ~7.4-7.5 (Figure 31ef). While these results are qualitatively consistent with previous observations,[239–241] our full-frame fast recording quantified absolute pH at high

spatiotemporal resolutions. For the CCCP-treated cells, we thus found diverse pH dynamics between different mitochondria in the same cell (Figure 31f). For the spontaneous pH jumps in untreated live cells, we showed that the matrix pH of individual mitochondria abruptly rose by ~0.1-0.3 units in ~2 s, and such fast processes often coincided with abrupt mitochondrial shape changes that were fittingly captured with our 0.8 s full-frame time resolution (Figure 31hi). The pH then gradually decreased in ~30 s and overshot to a value ~0.05 lower than the starting pH, a process often accompanied by further changes in mitochondrial shape (Figure 31hi).

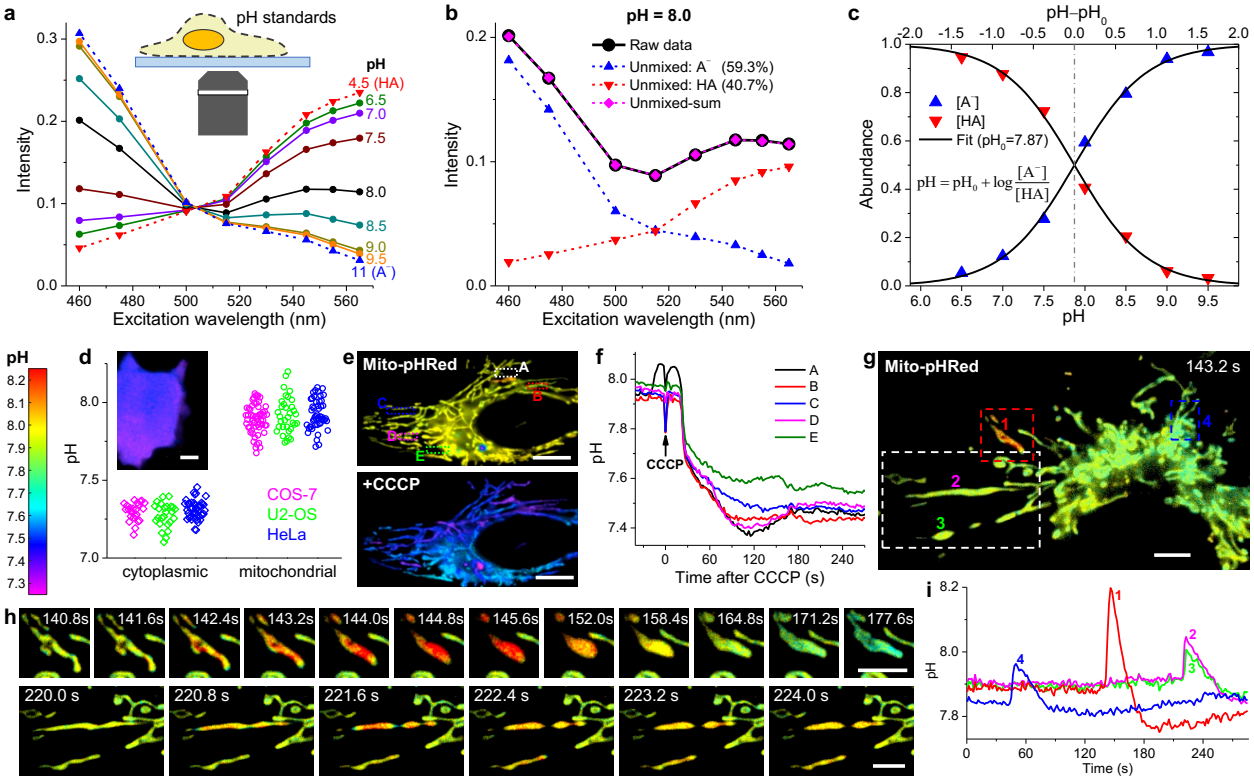

Figure 31: Absolute pH imaging in live cells via unmixing and quantifying two fluorescent species. (a) Excitation spectra measured by our spectral microscope, for pHRed in proton-permeabilized COS-7 cells in buffer standards of pH = 4.5 and 11 (dash lines; taken as pure forms of HA and A^-, respectively), and of pH = 6.5-9.5 (solid lines). (b) Linear unmixing of the excitation spectrum at pH = 8.0 (black solid line) into HA and A^- components (dash lines). (c) Fitting the resultant HA and A^- abundances unmixed at different pH values to the Henderson-Hasselbalch equation with a single parameter pH_0. (d) Statistics of the average pH values of the cytoplasm and mitochondrial matrix of live COS-7, U2OS, and HeLa cells, measured with our approach using cytoplasmic pHRed and Mito-pHRed, respectively. Inset: Color-coded absolute pH map of the cytoplasm of a live COS-7 cell. (e) Mito-pHRed absolute pH maps [same color scale as (d)] of the mitochondrial matrix in a live HeLa cell, before (top) and after (bottom) 120 s treatment with 20 μM CCCP. (f) pH value time traces for the five regions marked in (e). (g) Color-coded Mito-pHRed absolute pH map of the mitochondrial matrix in a live COS-7 cell, at the time point of 143.2 s. (h) Time sequences for the red and white boxed regions in (g), for two different time windows. (i) pH value time traces for the four mitochondria marked in (g). Experiments were performed with 8-wavelength excitation cycles at 10 fps, corresponding to 0.8 s acquisition time for each spectral image. Scale bars: 10 μm (d, e); 5 μm (g, h).

7.2.5 FRET imaging in live cells via resolving the excitation spectrum

We next examined another major class of biosensors based on Förster resonance energy transfer (FRET). Although modern FRET imaging often focuses on separating the fluorescence emissions of the donor and acceptor fluorophores,[219,221] early FRET spectroscopy studies favored the analysis of the excitation spectrum:[242] when monitoring the emission from the acceptor, FRET gives rise to new features in the excitation spectrum corresponding to donor absorption.

We achieved a microscopy version of this spectroscopy approach using the Clover-mRuby2 FP pair.[243] As our emission band well-matched the emission of mRuby2 but not Clover, for COS-7 cells co-expressing the two free FPs, the recorded 8-wavelength excitation spectrum was dominated by mRuby2 (Figure 32a, solid line). Unmixing this spectrum into mRuby2 and Clover components (Figure 32a, dash lines) showed the peak height of the latter to be ~7% of the former. In contrast, for a construct in which Clover and mRuby2 were directly linked, the excitation spectrum showed a substantial rise at ~500 nm (Figure 32b, solid line), attributable to FRET-induced mRuby2 emission due to Clover absorption.[242] Unmixing the spectrum into mRuby2 and Clover components (Figure 32b, dash lines) showed the peak height of the latter to be ~62% of the former. Subtracting the above ~7% bleed-through from Clover emission thus yielded an ~0.55 ratio between the peak heights due to the FRET donor and acceptor. Given the near-identical peak extinction coefficients of mRuby2 and Clover,[243] this ~0.55 ratio may be taken as the FRET transfer efficiency E (Materials and methods),[242] in agreement with emission spectroscopy results[243] on a similar construct (0.55).

We next constructed a FRET sensor for quantifying macromolecular crowding in live cells by linking Clover and mRuby2 with a long, conformationally flexible domain.[147] When expressed in the COS-7 cell cytoplasm, this sensor exhibited lower FRET efficiencies (Figure 32cd) than the directly linked Clover-mRuby2 (Figure 32b), consistent with increased donor-acceptor distances. Upon treating the live cells with 150% and 50% osmotic pressures of the normal medium, the measured FRET efficiency rose and dropped substantially (Figure 32d-h), as expected for the reduced and increased donor-acceptor distances under raised and lowered levels of macromolecular crowding inside the cells, respectively.[147]

Through continuous recording under our 8-wavelength excitation scheme at 10 fps and performing the above FRET analysis for every pixel, we obtained full-frame FRET images at 0.8 s time resolution, and thus unveiled rich spatiotemporal heterogeneities in macromolecular crowding in live cells (Figure 32ef). In untreated COS-7 cells, the observed FRET efficiency was largely uniform within each cell, yet varied substantially (~0.29-0.33) between cells. Interestingly, whereas the 150% hypertonic treatment resulted in quick rises in the intracellular FRET signal that plateaued in ~25 s (Figure 32eg), the 50% hypotonic treatment led to slow decreases in the FRET signal over ~500 s and subsequent recoveries (Figure 32fh). These results may be rationalized with the contrasting, quick reduction versus slow expansion-recovery of cell volumes under hypertonic and hypotonic conditions.[244,245] At the subcellular level, we found that for the hypertonic treatment, the nuclear FRET signals rose slower and achieved lower final increases when compared to the cytoplasm (~0.03 vs. ~0.05) (Figure 32eg). This result may indicate that the nuclear envelop retarded volume reduction and thus the rise in macromolecular crowding. In contrast, for the

opposite, slow hypotonic process, the cytoplasmic FRET signals dropped slower than the nuclei, with some cells further showing complete recovery over long periods of time (Figure 32fh). This result may be attributed to the regulatory volume decrease processes in the cytoplasm.[246]

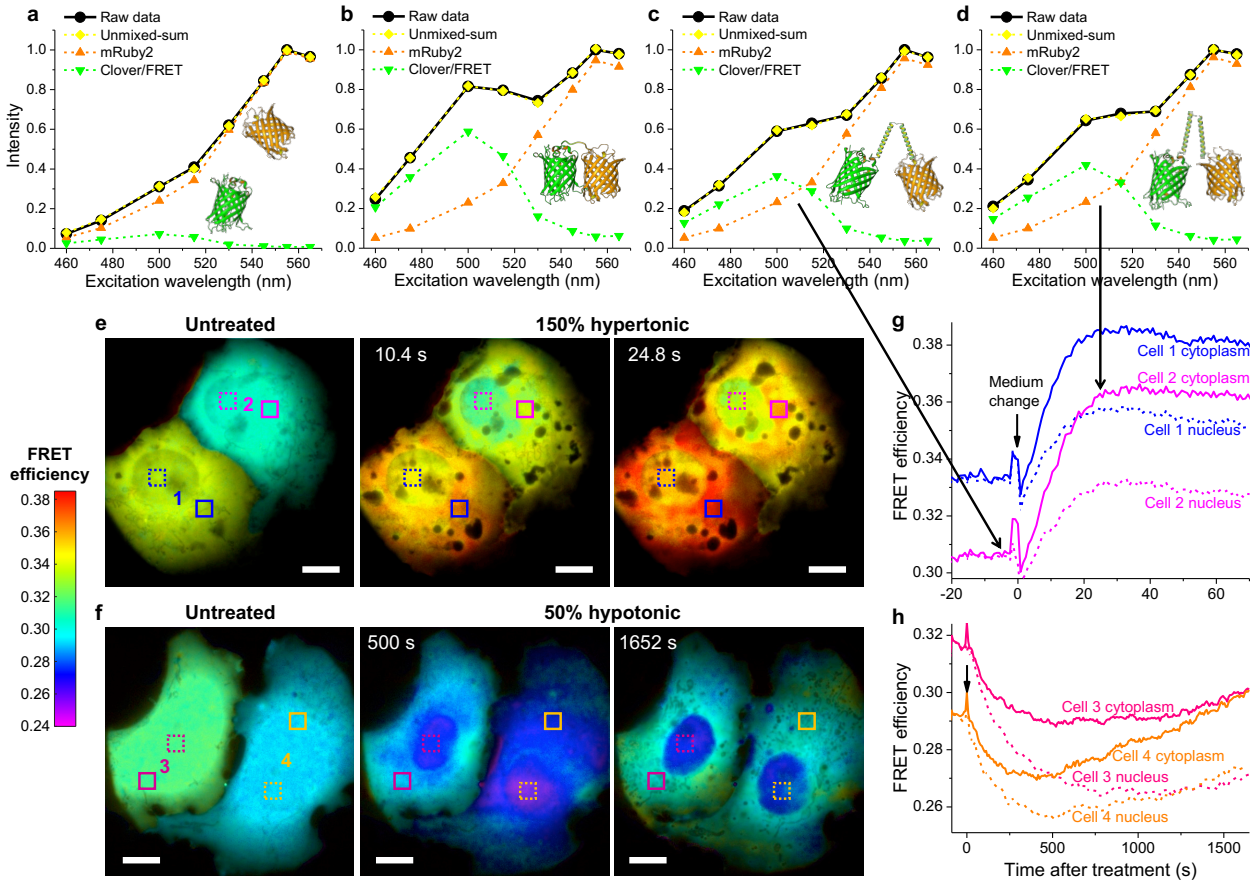

Figure 32: FRET imaging in live cells via resolving the excitation spectrum. (a) Excitation spectrum measured by our spectral microscope (black solid line) and its unmixing (dash lines) for non-interacting mRuby2 and Clover co-expressed in the cytoplasm of a live COS-7 cell. (b) Measured excitation spectrum and its unmixing for a directly linked Clover-mRuby2 construct expressed in a live COS-7 cell. (c,d) Measured excitation spectrum and its unmixing for the Clover-mRuby2 FRET crowding sensor in the cytoplasm of a live COS-7 cell, before (c) and ~25 s after (d) 150% hypertonic treatment by adding into the cell medium an equal volume of medium that was supplemented with 300 mM sorbitol. (e) Color-coded FRET maps for the crowding sensor, for two live COS-7 cells before (left), ~10 s after (center), and ~25 s after (right) the 150% hypertonic treatment. (f) Color-coded FRET maps for the crowding sensor, for two live COS-7 cells before (left), 500 s after (center), and 1650 s after (right) 50% hypotonic treatment by adding into the medium an equal volume of water. (g, h) FRET value time traces for the boxed regions of cytoplasm (solid lines) and nuclei (dash lines) of the 4 cells in (e, f). Experiments were performed with 8-wavelength excitation cycles at 10 fps (0.8 s acquisition time for each spectral image). Scale bars: 10 μm (e, f).

7.2.6 Discussion

In this work, we demonstrated excitation spectral microscopy as a powerful tool for both fast multi-target imaging and quantitative biosensing, as well as their combined use. Whereas previous spectral-imaging efforts often focus on resolving the emission spectrum, the need to disperse the local spectra impedes applications to high-throughput imaging in the wide-field. Meanwhile, as recent experiments probe the dynamics of 6 subcellular targets by exciting with 6 lasers that span the entire visible range, high (~50%) crosstalks are found in spite of the large spectral separation.[234] Separately, although fluorescence lifetime imaging and stimulated Raman scattering microscopy have recently enabled highly multiplexed imaging,[190,247] dedicated optical setups and/or labeling probes are required, and they cannot be readily applied to fast wide-field imaging.

We showed that under the typical wide-field fluorescence microscopy scheme with a conventional single-band filter cube, by fast scanning the excitation wavelength from a low-cost white lamp, 6 subcellular targets, labeled by common fluorophores of substantial spectral overlap, can be simultaneously imaged in live cells at low (~1%) crosstalks. By synchronizing the excitation wavelength to each camera frame through fast electronic modulation of the AOTF, full-frame excitation spectral images were obtained with no moving parts, hence high temporal resolutions that were effectively only limited by the camera framerate and the desired number of excitation wavelengths. As an additional benefit, as fluorescence detection was performed for a fixed emission band, the measured spectral behaviors were robustly defined by the preset excitation profiles and independent of the spectral response of the detection system. We thus were able to freely switch between different sCMOS and EM-CCD cameras in this study without the need to modify or recalibrate the system. The potential extension of our approach to even more fluorophores may be achieved by further increasing the number of excitation wavelengths or integrating emission dispersion, although the latter approach would encounter the same throughput limitations we set out to overcome in the first place. Practically, the ultimately achievable multi-target imaging capability is further limited by how well different intracellular targets may be concurrently and specifically labeled.

The capability to unmix and quantify different, spectrally overlapped fluorescent species in the same sample via the excitation spectrum next enabled us to devise fast, quantitative imaging schemes for fluorescent biosensors in live cells, as well as their multiplexing with additional fluorophores. For the bi-state sensor pHRed, we quantified the pH-dependent abundances of its protonated and deprotonated states, and well fitted them to the ideal Henderson-Hasselbalch equation to enable absolute pH imaging, thus visualizing concurrent fast changes in the mitochondrial shape and matrix pH. For FRET imaging, we established a microscopy version of the early excitation spectroscopy approaches to quantify FRET efficiency, and thus achieved high sensitivities and spatiotemporal resolutions in unveiling rich dynamics for macromolecular crowding in live cells.

7.3 Conclusion

In conclusion, our results unveil the exceptional opportunities excitation spectral microscopy provides for highly multiplexed fluorescence imaging. Whereas in this work we focused on a facile system based on a lamp-operated epifluorescence microscope, the fast multi-fluorophore and quantitative biosensor imaging capabilities we demonstrated here should be readily extendable to other systems, including light-sheet fluorescence microscopy[217,248] and structured illumination

microscopy[249], for which cases frame-synchronized fast wavelength scanning may be implemented with supercontinuum light sources.[250] The prospect of acquiring fast spectral images in the wide-field without the need for fluorescence dispersion or the care for the spectral response of the detector offers tremendous potential.

7.4 Materials and methods

Optical setup

White light from a plasma lamp (HPLS301, Thorlabs) was collimated into a beam ~4 mm in diameter, and linearly polarized through a wire grid polarizer (WP25M-VIS, Thorlabs). The polarized beam entered an acousto-optic tunable filter (AOTF) (EFLF100L1, Panasonic), and the 1st order diffracted beam, with its polarization direction rotated by 90° versus the incident beam,[230] was cleaned up with a second polarizer (WP25M-VIS) mounted perpendicular to the first polarizer (Figure 29). This excitation beam was coupled into an Olympus IX73 inverted epifluorescence microscope and focused at the back focal plane of an oil-immersion objective lens (Olympus, UPLSAPO100XO, NA 1.40), thus illuminating a sample area of ~70 μm diameter. The excitation filter, dichroic mirror, and emission filter used were FF01-505/119, FF573-Di01, and FF01-630/92, respectively, from Semrock. The AOTF unit was driven by an 8-channel RF synthesizer (97-03926-12, Gooch & Housego). The excitation wavelength profiles at different applied RF frequencies were measured using a visible spectrometer (USB4000-VIS-NIR, Ocean Optics), with power levels determined by a photodiode power sensor (S120VC, Thorlabs). Typical excitation power was ~6 μW [for recording at 10 frames per second (fps)] and ~27 μW (for recording at 240 and 202 fps) at each wavelength, corresponding to a power density of ~0.16-0.72 W/cm^2 at the sample, which allowed adequate signal and minimal photobleaching. The prolonged recording in Fig. 4fh was performed with lowered excitation powers of ~2 μW. Wide-field fluorescence images were continuously recorded using an sCMOS camera (Zyla 4.2, Andor) at an effective pixel size of 130 nm (after 2×2 binning) for 512×512 pixels (67×67 μm^2 field of view) at 10 fps or for 512×150 pixels (67×20 μm^2 field of view) at 202 fps, or an EMCCD camera (iXon Ultra 897, Andor) at an effective pixel size of 160 nm for 448×110 pixels (72×18 μm^2 field of view) at 240 fps. The camera was internally triggered, and the "fire" (exposure) output trigger signal was read by a multifunction I/O board (PCI-6733, National Instruments), which in turn modulated the RF synthesizer for the synchronized control of the excitation wavelength in each camera frame (below).

Spectral imaging via fast AOTF scanning of the excitation wavelength

In most experiments, the 8 channels of the RF synthesizer were preset to 8 different fixed RF frequencies and powers, hence 8 fixed excitation wavelengths and intensities for the AOTF output. These 8 excitations were sequentially applied to each successive camera frame in cycles, so that full-frame excitation-spectral images were obtained every 8 consecutive camera frames. For the 6-target imaging of fixed cells, the preset AOTF driving frequencies were 61.567, 63.400, 65.148, 66.749, 68.454, 70.277, 71.500, and 82.370 MHz, corresponding to excitations centered at 565, 555, 545, 535, 525, 515, 505, and 460 nm, respectively, and they were synchronized with 10 fps sCMOS recording. For the 6-target imaging of live cells and all biosensor experiments, the 8 AOTF driving frequencies were 61.567, 63.400, 65.148, 66.995, 70.277, 72.700, 78.420, and 82.370 MHz, corresponding to excitations centered at 565, 555, 545, 530, 515, 500, 475, and 460 nm, respectively, and they were also synchronized with 10 fps sCMOS recording. For the 4-

excitation wavelength imaging of fast dynamics in live cells, 4 RF channels were set to 63.400, 70.277, 72.700, and 82.370 MHz, corresponding to excitations centered at 555, 515, 500, and 460 nm, respectively, and they were synchronized with 240 fps EMCCD or 202 fps sCMOS recordings.

Acquiring the reference excitation spectra

The reference excitation spectrum of each fluorophore was obtained from singly labeled live and fixed cells by recording images at the above preset excitation wavelengths on our setup. For pHRed, excitation spectra at different pH values were obtained from pHRed-expressing COS-7 cells that were proton-permeabilized with valinomycin and nigericin and immersed in a series of buffer standards (Intracellular pH Calibration Buffer Kit, P35379, ThermoFisher, plus additional homemade buffers).

Linear unmixing of the experimentally recorded excitation spectra

For both multi-fluorophore and biosensor imaging, the recorded excitation spectrum at each pixel, *e.g.*, collected from 8 consecutive frames of raw images, was each unmixed into a linear combination of the reference excitation spectra (above) of the pertaining fluorophores using least squares regression under non-negativity constraints.[46,222] The resultant abundances of different fluorophores at each pixel were directly used to generate unmixed images for multi-target imaging or processed further for quantitative biosensor imaging, as described in the text.

Calculation of the FRET efficiency

The use of excitation spectra to calculate the FRET efficiency is established in earlier studies:[242] for a FRET system consisting of a donor and an acceptor, if one monitors the fluorescence emission of the acceptor, the excitation spectrum F is a linear combination of the absorption spectra of the acceptor and the donor: $F = \varepsilon_A + E\varepsilon_D$. Here E is the FRET efficiency, and ε_A and ε_D are the wavelength-dependent extinction coefficients of the acceptor and the donor, respectively. In our experiments, for each pixel we experimentally obtained F, and linearly unmixed it into the excitation (absorption) spectra of the donor and the acceptor (above). E may thus be determined from the ratio between the peak heights of the donor and acceptor, scaled by the ratio between the known peak extinction coefficients of the acceptor and the donor. For our FRET pair, the peak extinction coefficients Clover and mRuby2 are near identical[243] (111 vs. 113 $mM^{-1}\ cm^{-1}$). We thus took the peak height ratios between the donor and acceptor (minus the ~7% bleed-through from the donor emission) directly as the FRET efficiency.

Plasmids

tdTomato-ER-3 and LAMP1-Clover (Clover-Lysosomes-20) were gifts from Michael Davidson (Addgene #58097 and #56528). Mito-PhiYFP (pPhi-Yellow-mito) was from Evrogen (#FP607). GW1-pHRed and GW1-Mito-pHRed were gifts from Gary Yellen (Addgene #31473 and #31474) for expression of pHRed in the cytoplasm and mitochondrial matrix, respectively.[239] The Clover-mRuby2 FRET crowding sensor was constructed by inserting a conformationally flexible linker[147] [$(GSG)_6A(EAAAK)_6A(GSG)_6A(EAAAK)_6A(GSG)_6$; synthesized by Twist Bioscience] between the Clover and mRuby2 of pcDNA3.1-Clover-mRuby2 (Addgene #49089; a gift from Kurt Beam) at the AgeI site. The co-expression plasmid of free Clover and mRuby2 was constructed by inserting an internal ribosome entry site (cloned from Addgene #127332; a gift from Jeremy Wilusz) between the Clover and mRuby2 of pcDNA3.1-Clover-mRuby2 at the AgeI site. For the expression of untagged Parkin, pCMV-Parkin was constructed by inserting Parkin (cloned from

Addgene #89299, a gift from Michael Lazarou) into an N1 cloning vector (cut from Addgene #54642, a gift from Michael Davidson). mOrange2-Parkin was constructed by first inserting mCherry-Parkin (cloned from Addgene #59419, a gift from Richard Youle) into an N1 cloning vector (cut from Addgene #54642, a gift from Michael Davidson), and then replacing mCherry with mOrange2 (cloned from Addgene #57969, a gift from Michael Davidson) between the BmtI and BspEI sites. PhiYFP-Parkin was constructed by replacing mOrange2 in the mOrange2-Parkin with PhiYFP between the BmtI and BspEI sites. PhiYFP-LC3 was constructed by replacing mRFP in the pmRFP-LC3 (Addgene #21075; a gift from Tamotsu Yoshimori) with PhiYFP between the BmtI and BglII sites. Clover-LC3 was constructed by replacing mRFP in the pmRFP-LC3 with Clover between the BmtI and BglII sites. LAMP1-mOrange2 was constructed by replacing mRuby2 in the LAMP1-mRuby2 (Addgene #55902; a gift from Michael Davidson) with mOrange2 between the AgeI and NotI sites.

Live-cell experiments

COS-7, U2-OS, and HeLa cells (Cell Culture Facility, UC-Berkeley) were cultured in Dulbecco's modified Eagle's medium (DMEM) (Gibco 31053-028) supplemented with 10% fetal bovine serum (Corning), 1× GlutaMAX Supplement, and 1× non-essential amino acids, at 37°C and 5% CO_2. For live-cell experiments, cells were cultured in Lab-Tek 8-well chambered coverglass (ThermoFisher), and transiently transfected with the above plasmids, either alone or in combination. Transfection was performed using Lipofectamine 3000 (ThermoFisher) or the Neon Transfection System (ThermoFisher), following the manufacturers' instructions. For live-cell staining of the plasma membrane, lipid droplet, and DNA, wheat germ agglutinin (WGA) CF532 (300-500×, 29064, Biotium), LipidSpot488 (300-1000×, 70065, Biotium), and SYBR Green (15000-100000×, S7536, ThermoFisher) were added to the medium for 30 min at 37°C and washed 3 times with DMEM before imaging. Imaging buffer was the regular culture medium with the addition of 25 mM HEPES at pH 7.4 (15630106, Gibco) or a commercial buffer based on MOPS (Hibernate A, BrainBits), with similar results observed.

Fixed-cell experiments

For fixed-cell experiments, COS-7 cells were plated in an 8-well LabTek chamber at ~30% confluency. After 24 h, cells were fixed using 3% paraformaldehyde and 0.1% glutaraldehyde in phosphate-buffered saline (PBS) followed by two washes with 0.1% sodium borohydride in PBS. Cells were blocked and permeabilized in a blocking buffer (3% bovine serum albumin with either 0.5% Triton X-100 or 0.02% saponin in PBS), followed by primary and secondary antibody labeling. Primary antibodies used were chicken anti-α-tubulin (ab89984, Abcam) for labeling of microtubules, rabbit anti-Nogo (ab47085, Abcam) for labeling of ER, mouse IgG1 anti-NPM1 (32-5200, ThermoFisher) for labeling of nucleoli, and mouse IgG2a anti-Tom20 (sc-17764, Santa Cruz Biotech) for labeling of mitochondria. Secondary antibodies (Jackson ImmunoResearch) were labeled via reaction with dye NHS esters: CF514 (92103, Biotium), CF568 (92131, Biotium), ATTO 532 (AD532-31, ATTO-TEC) and ATTO 542 (AD542-31, ATTO-TEC). After antibody staining, cells were incubated in LipidSpot488 (300-1000×, 70065, Biotium) and SYBR Gold (300-1000×, S11494, ThermoFisher) in PBS to stain lipid droplets and nuclear DNA for 30 min, and the sample was washed with PBS for 10 min × 3 times before imaging in PBS.

Chapter 8: Microscopy-driven discovery of a novel trafficking organelle

The work in this chapter was conducted in collaboration with Kun Chen and Ke Xu. It is reproduced in part here from Yan et al[251] with permission from all co-authors.

8.1 Introduction

The excitation spectral microscopy described in the previous chapter enabled us to look into fast dynamics of cellular organelles, such as the motion of vesicles in intracellular trafficking. In this chapter, we focus on the transport intermediates between the ER and the Golgi, motivated by the unexpected observation of a mistargeted ER-bound protein.

About 6,000 human proteins, after synthesized at the ER, are transported to the Golgi apparatus for secretion or sorting to other organelles.[252–255] How cells selectively transport different proteins to fulfill their diverse functions has elicited a wealth of research interest. Under current models, ER-to-Golgi trafficking starts at the ER-exit sites (ERESs), where the cargo receptor or the cargo itself recruits the coat protein complex II (COPII) to generate ER-derived vesicles.[252,256–258] Whereas in yeasts these vesicles appear to directly reach the Golgi apparatus via cytoplasmic diffusion,[252,258] in animal cells they relay the cargo to the ER-Golgi intermediate compartment (ERGIC) for microtubule-dependent sorting to the Golgi apparatus.[259,260] Additionally, proteins lacking affinity to any receptors may be transported via "bulk flow" through nonspecific packaging into the ERES.[252,255]

Contrasting with the diversity of protein cargoes and receptors identified over the past decades, the ERGIC is often simply represented by the presence of the membrane lectin ERGIC-53/LMAN1, which may not define all carriers mediating ER-to-Golgi trafficking.[259–261] Whereas electron microscopy often shows ERGIC as vesiculo-tubular clusters (VTCs) <~1 μm in size,[262,263] elongated tubular carriers have also been noted.[264–266] Live-cell fluorescence microscopy using synchronized cargoes has also occasionally noted long (>2 μm) tubular carriers in ER-to-Golgi trafficking,[267–272] yet some cargoes do not seem to access this pathway.[273,274] Whether these morphologically distinct carriers are specific to different protein cargoes, and if so, what determines such selectivity, remain elusive. Furthermore, the functional significance of this morphological diversity in regulating transport kinetics remains unexplored.

In this chapter we report tubular ERGIC (t-ERGIC), a distinct class of ERGIC that specifically expedites the ER-to-Golgi transport of soluble cargoes of the receptor SURF4, the mammalian homolog of the yeast cargo receptor Erv29p.[253,275,276] The t-ERGIC lacks ERGIC-53 but is marked by the small GTPase Rab1, and further differs from the canonical ERGIC/VTCs by its extremely slender shape. After de novo generation at expanded ERESs via SURF4-cargo interactions, the t-ERGIC travels and recycles in the cell at high speeds to enable efficient ER-to-Golgi transport.

8.2 Results and discussion

8.2.1 Identification of a highly elongated tubular organelle through mislocalized DsRed2-ER-5

We initially attempted to deliver the red fluorescent protein (FP) DsRed2 into the ER lumen of COS-7 cells via an N-terminal signal peptide. Curiously, whereas DsRed2-ER-3 (Figure 33a) correctly localized to the ER (Figure 33b), a similar construct with slightly varied linkers, DsRed2-ER-5 (Figure 33a), only showed up the expected ER localization in ~20% of the transfected cells. A preponderance (~45%) of the cells had fluorescence mainly distributed in peculiar, 2-20 μm long tubular organelles (TOs) (Figure 33b-d), while another major population (~30%) had most fluorescence in small vesicles (Figure 33d).

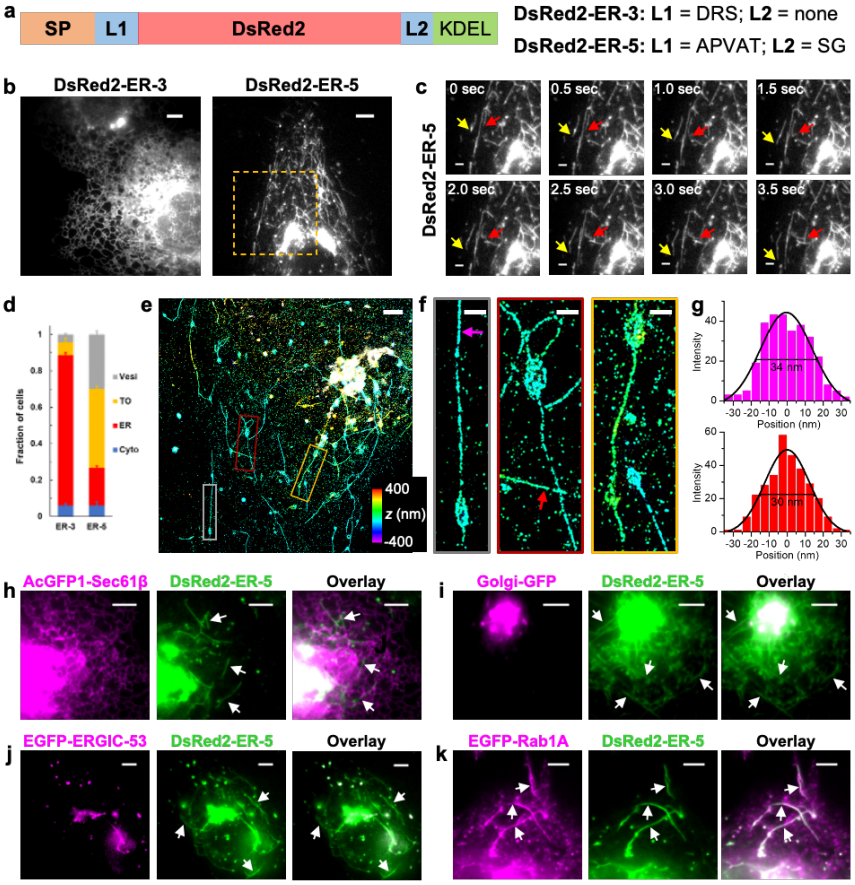

Figure 33: DsRed2-ER-5 mislocalizes to an extremely slender, Rab1-positive tubular organelle. (a) Schematics of the sequences of DsRed2-ER-3 and DsRed2-ER-5. SP: signal peptide; L: linker. (b) Representative live-cell images of DsRed2-ER-3 and DsRed2-ER-5 expressed in COS-7 cells. (c) Time-lapse series of the boxed region in (b), showing the morphology and fast motion of the tubular organelles (TOs) (arrows). (d) Classification of the dominating distribution modes of DsRed2-ER-3 and DsRed2-ER-5 in each cell: ER, TO, vesicles (Vesi), and cytoplasm (Cyto). Error bars: SEM (n = 4 with ~50 cells in each replicate). (e) 3D-STORM image of immunolabeled DsRed2-ER-5 in a COS-7 cell. Colors encode axial positions. (f) Close-ups of the TOs in the three colored boxes in (e). (g) STORM intensity profiles across the widths of two TOs at the magenta and red arrows in (f). Black curves: Gaussian fits with FWHM of 34 and 30 nm, respectively. (h-k) Dual-color live-cell images of DsRed2-ER-5 (green) with the ER marker AcGFP1-Sec61β (h), the Golgi marker Golgi-GFP (i), the canonical ERGIC marker EGFP-ERGIC-53 (j), and the small GTPase EGFP-Rab1A (k). Arrows point to TOs. Scale bars: 5 μm (b,h-k); 2 μm (c,e); 500 nm (f).

The DsRed2-ER-5-containing TOs each had one or a few enlarged vesicular bodies and a thin projection, and underwent frequent deformation, fission, and fusion as they moved actively in the cell at typical speeds of 1-2 µm/s (Figure 33c). The vesicular bodies were often found at the tubule ends, yet they also frequently slid along the TOs, indicating high structural flexibility. 3D STORM super-resolution microscopy[125] further revealed their unusual ultrastructure (Figure 33ef): Whereas the vesicular bodies were spheroids ~500 nm in size, the elongated projections were extremely thin with apparent diameters of ~30 nm (Figure 33g). Given the ~20 nm resolution of STORM and the immunolabeling antibody sizes,[125] the true diameters should thus be <30 nm.

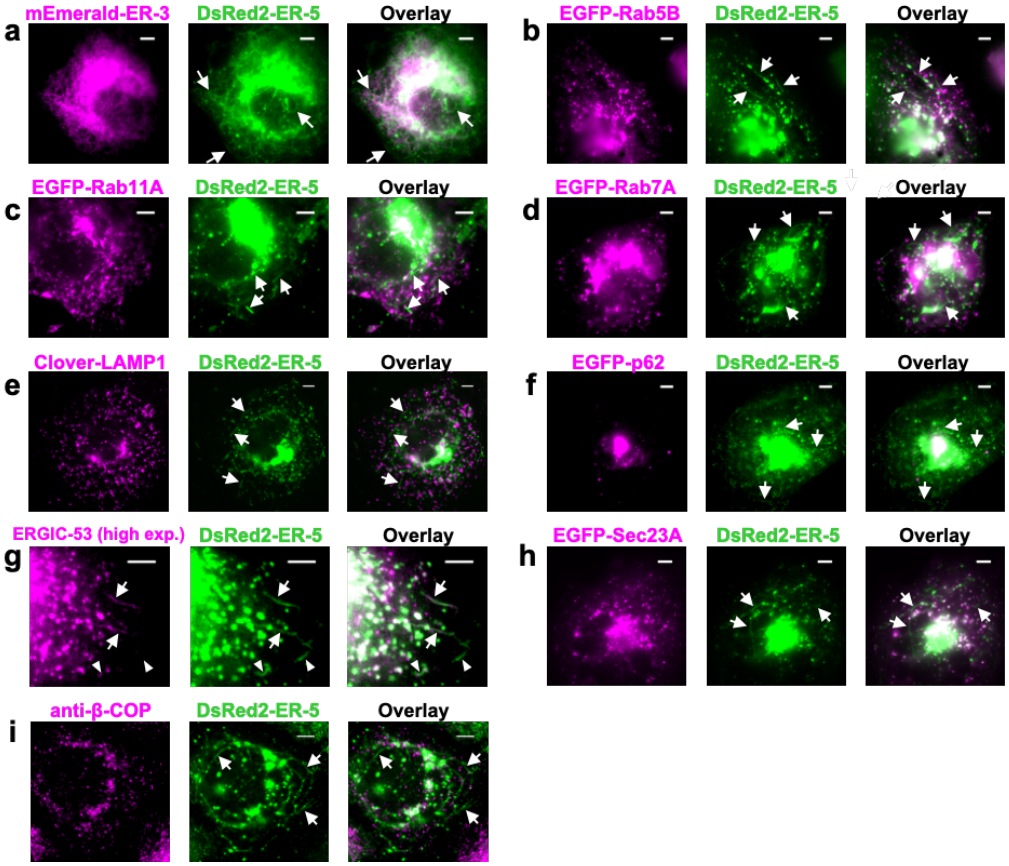

Figure 34: Localization of DsRed2-ER-5 compared to various organelle markers. (a-h) Dual-color fluorescence micrographs of DsRed2-ER-5 (green) in live COS-7 cells with the ER markers mEmerald-ER-3 (a), the early endosome marker EGFP-Rab5B (b), the recycling endosome marker EGFP-Rab11A (c), the late endosome marker EGFP-Rab7A (d), the lysosome marker Clover-LAMP1 (e), the autophagosome marker EGFP-p62 (f), the highly expressed ERGIC marker AcGFP1-ERGIC-53 (g), and the ERES marker EGFP-Sec23A (h). Arrowheads in (g) indicate TOs negative for ERGIC-53. (i) Immunofluorescence of the COPI vesicle marker β-COP vs. DsRed2-ER-5. Scale bars: 5 µm. Arrows point to TOs.

To identify these TOs, we performed dual-color fluorescence microscopy of DsRed2-ER-5 and different organelle markers in living cells. The TOs did not have soluble or membrane markers of the ER (Figure 33h, 34a), nor were they positive for common markers of endosomes, autophagosomes, or lysosomes (Figure 34b-f). Instead, we noticed dynamic interactions of the TOs with the Golgi apparatus, where the FP accumulated (Figure 33i), suggesting its involvement

in the secretory pathway. Interestingly, whereas the canonical ERGIC marker ERGIC-53 colocalized with DsRed2-ER-5 in vesicle-like structures, it was absent from the TOs (Figure 33j). However, when ERGIC-53 was overexpressed at high levels, it also entered a subset of the TOs (Figure 34g), implying interactions and material exchange between the TOs and the canonical ERGIC. COPII and COPI coats also only partly colocalized with DsRed2-ER-5 in puncta but not in the TOs (Figure 34hi).

We next found Rab1A/B, the major small GTPases in ER-to-Golgi trafficking,[277–279] are enriched on the surface of the DsRed2-ER-5-containing TOs, a result supported by both expressed EGFP-Rab1A (Figure 33k, 35a) and the immunostaining of endogenous Rab1A and Rab1B (Figure 35bc). Time-lapse imaging captured the dynamic flow of DsRed2-ER-5 from the ER to small vesicles (Figure 35d). In this process, the TOs only existed before DsRed2-ER-5 reached its maximal signal at the Golgi, suggesting that they are intermediates between the ER and the Golgi. Together, we identified the DsRed2-ER-5-containing, highly elongated TO as a Rab1-coated ERGIC that is not normally enriched with ERGIC-53. Hereafter we refer to it as "tubular ERGIC (t-ERGIC)".

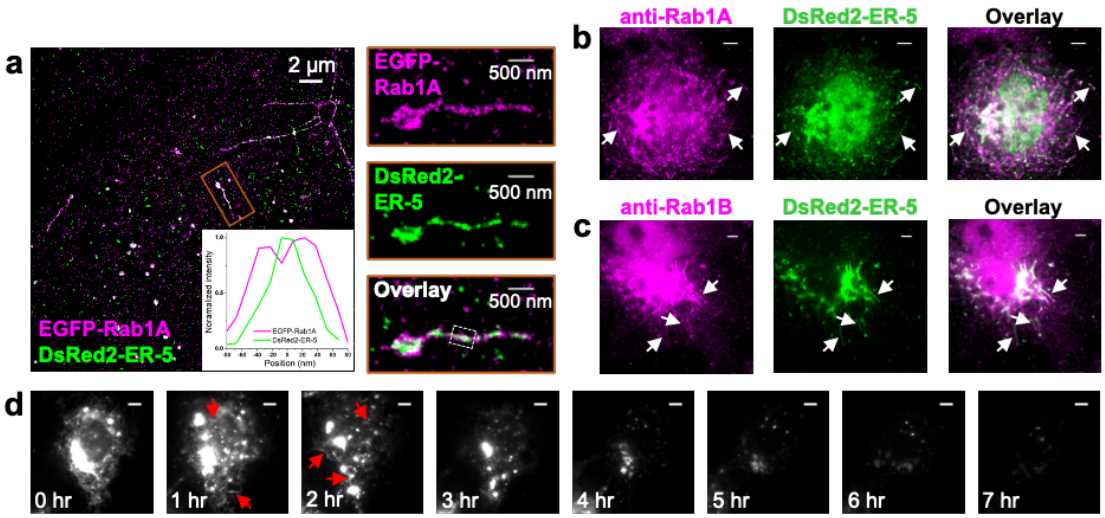

Figure 35: DsRed2-ER-5 TOs are labeled by Rab1A/B and exist between the ER and the Golgi. (a) Two-color STORM of immunolabeled DsRed2-ER-5 and EGFP-Rab1A showing that Rab1A decorates the surface of the TO. Inset: cross-sectional intensity profiles of the boxed region in the overlay. (b,c) Immunofluorescence of endogenous Rab1A (b) and Rab1B (c) in COS-7 cells, showing good colocalization with the DsRed2-ER-5 TOs. (d) Time-lapse imaging of DsRed2-ER-5 in an unsynchronized COS-7 cell, showing its redistribution from the ER to the TOs, Golgi, and vesicles accompanied by a reduction of fluorescence intensity. Scale bars: 5 μm except for the labeled scale bars in (a). Arrows point to TOs.

8.2.2 The t-ERGIC mediates ER-to-Golgi trafficking, and is formed through both de novo generation and fusion

To understand how DsRed2-ER-5 escaped from the ER, we examined the effects of different small molecules that respectively inhibited ER-to-Golgi transport (brefeldin A), induced ER stress (thapsigargin and dithiothreitol), and inhibited ER-associated degradation (CB-5083 and MG132). We only find time-dependent increase of intracellular retention with brefeldin A treatment (Figure

36ab), which was accompanied by a redistribution of the DsRed2-ER-5 fluorescence back to the ER (Figure 36c). These results suggest that DsRed2-ER-5 is targeted to the ER-to-Golgi transport pathway through t-ERGIC.

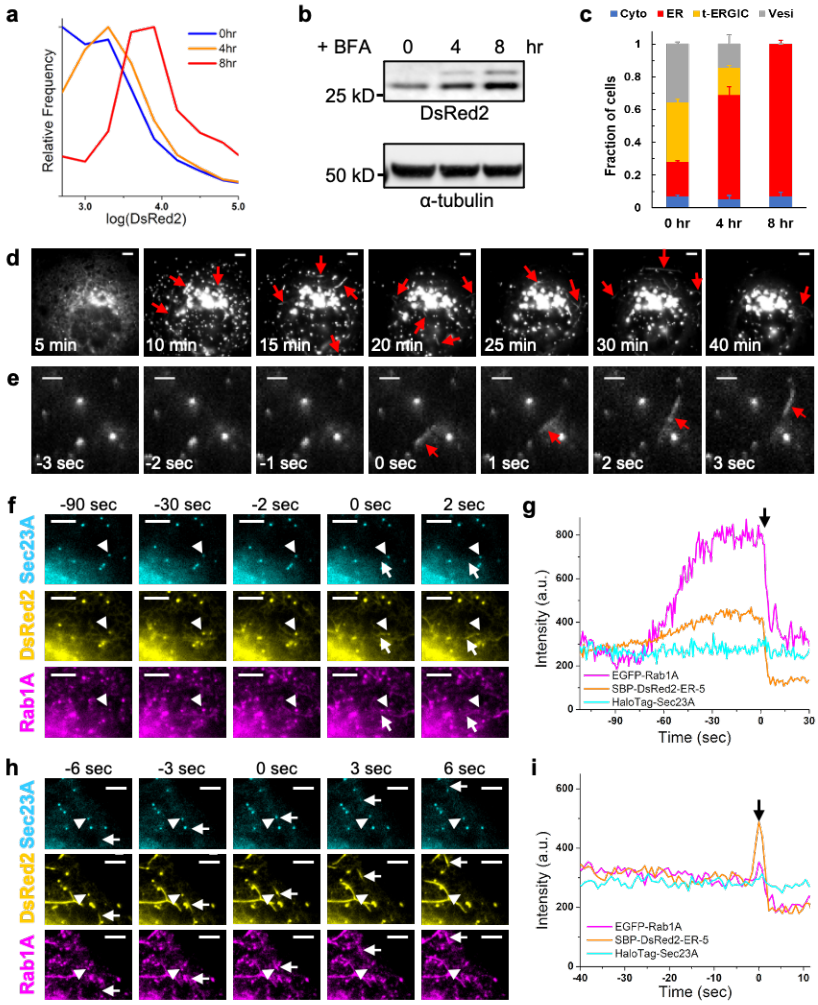

Figure 36: The t-ERGIC mediates ER-to-Golgi trafficking, and is formed through both de novo generation and fusion. (a-c) Flow cytometry histograms (a), lysate immunoblots (b), and subcellular distribution (c) of DsRed2-ER-5 for transfected COS-7 cells treated with 1 μM brefeldin A (BFA) for 0, 4, and 8 hr. Error bars: SEM (n = 3 with ~50 cells in each replicate). (d) Representative RUSH image sequence of SBP-DsRed2-ER-5 after the addition of 80 μM biotin at time 0. Arrows indicate t-ERGICs. (e) De novo generation of SBP-DsRed2-ER-5-positive t-ERGIC (arrow) in RUSH. Time 0 corresponds to when budding occurred. Biotin was added at -5 min for cargo release. (f) Image sequences of EGFP-Rab1A, SBP-DsRed2-ER-5, and JF635-labeled HaloTag-Sec23A in a RUSH experiment showing the de novo generation of a t-ERGIC (arrow) from the ERES (arrowhead). Time 0 corresponds to when budding occurred. Biotin addition corresponded to -20 min. (g) Fluorescence intensity time traces of the three color channels for the ERES indicated by the arrowhead in (f). (h) Another image sequence of an ERES (arrowhead) in the same RUSH experiment as in (f), showing its fusion with a pre-existing t-ERGIC (arrow). Time 0 corresponds to when fusion occurred. Biotin addition corresponded to -

28 min. (i) Fluorescence intensity time traces of the three color channels for the ERES indicated by the arrowhead in (h). Scale bars: 5 µm (d,f,h); 2 µm (e).

To elucidate the biogenesis and potential functions of the t-ERGIC, we next employed the Retention Using Selective Hooks (RUSH) assay[273] to synchronize the release of DsRed2-ER-5 from the ER. In RUSH, the cargo is tagged with a streptavidin binding peptide (SBP) and thus initially retained in the ER by an ER-resident streptavidin "hook". The addition of biotin outcompetes SBP for streptavidin binding and so enables the synchronized onset of ER-to-Golgi transport of the cargo. Insertion of the SBP tag at the N-terminus of DsRed2-ER-5 (Figure 37a) did not alter the phenotype (Figure 37bc). The SBP-DsRed2-ER-5 cargo was then co-expressed with a streptavidin-KDEL hook, which retained most of the fluorescence signal in the ER two days after transfection. Upon release of the cargo by biotin, we observed that the cargo first concentrated at the ERES and vesicle-like structures (Figure 36d). The t-ERGIC emerged right after ER exit (Figure 36de). Single-particle tracking of the vesicles and TOs showed an overall centripetal movement, as the fluorescence redistributed from the peripheral ER to the Golgi apparatus (Figure 37de). These results confirm that the t-ERGIC mediates anterograde ER-to-Golgi transport.

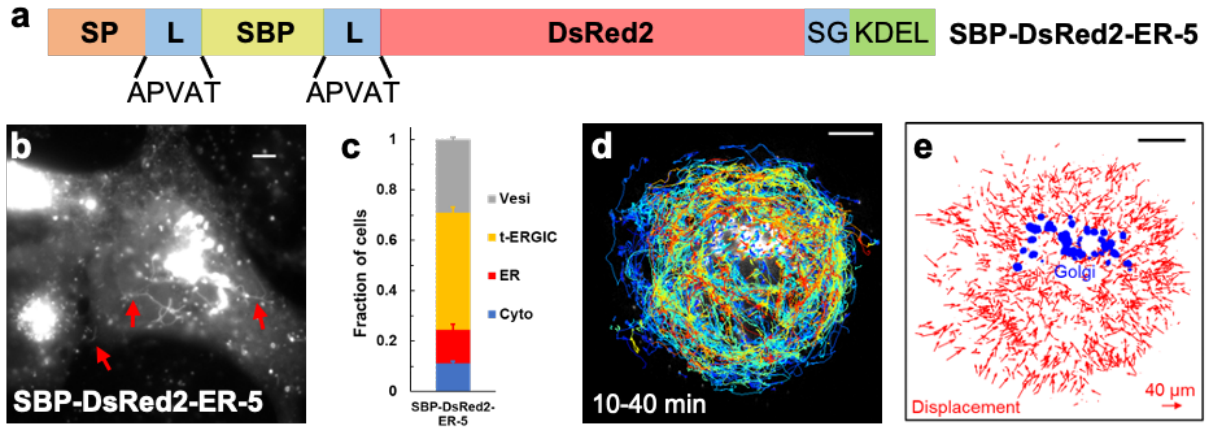

Figure 37: Design of SBP-DsRed2-ER-5 for RUSH and single-particle tracking in RUSH. (a-c) Schematic of SBP-DsRed2-ER-5 (a), a representative image of its presence in the t-ERGIC (b), and its subcellular distribution (c) in transfected COS-7 cells. Error bars: SEM (n = 3 with ~50 cells in each replicate). Arrows in (b) indicate t-ERGICs. (d) Single-particle tracking of post-ER carriers in Figure 36d. The color of each trajectory encodes the maximum speed reached. (e) Displacement map of the trajectories in (d). The Golgi apparatus is marked blue. Arrows point to the direction of displacement (from the initial position to the final position), and their magnitudes are scaled according to the legend. Scale bars: 10 µm (d,e); 5 µm (b).

A closer examination of the RUSH image sequences unveiled two modes of biogenesis for t-ERGIC: de novo formation vs. elongation of existing t-ERGIC through fusion. For the first mode, three-color live imaging of the cargo with the ERES marker Sec23A and the t-ERGIC marker Rab1A (Figure 36fg) showed that the cargo was first enriched at the ERES, where Rab1A gradually accumulated, leveled off, and then budded off together with the cargo into newly formed t-ERGIC tubules. The budded t-ERGIC then separated from the ERES, leaving behind the Sec23A COPII coat (Figure 36f), from which another t-ERGIC could bud again (Figure 38a). Accordingly, local fluorescence intensity time traces showed that DsRed2-ER-5 and Rab1A both accumulated

at the ERES before they simultaneously budded into the t-ERGIC in a single step, whereas Sec23A stayed constant (Figure 36g). In the second mode, existing t-ERGIC tubules actively collected more cargo at ERES as they rapidly traversed the cell (Figure 36hi). In particular, we often noticed cases in which tubules generated from the Golgi traveled retrogradely to fuse with the ERES and bring more cargo back to the Golgi (Figure 38b), a cycling behavior that has been noted previously for ERGIC.[269,270,280] Thus, the t-ERGIC is a carrier organelle that buds from the ERES and shuttles between the ER and the Golgi to mediate the anterograde transport of cargo proteins.

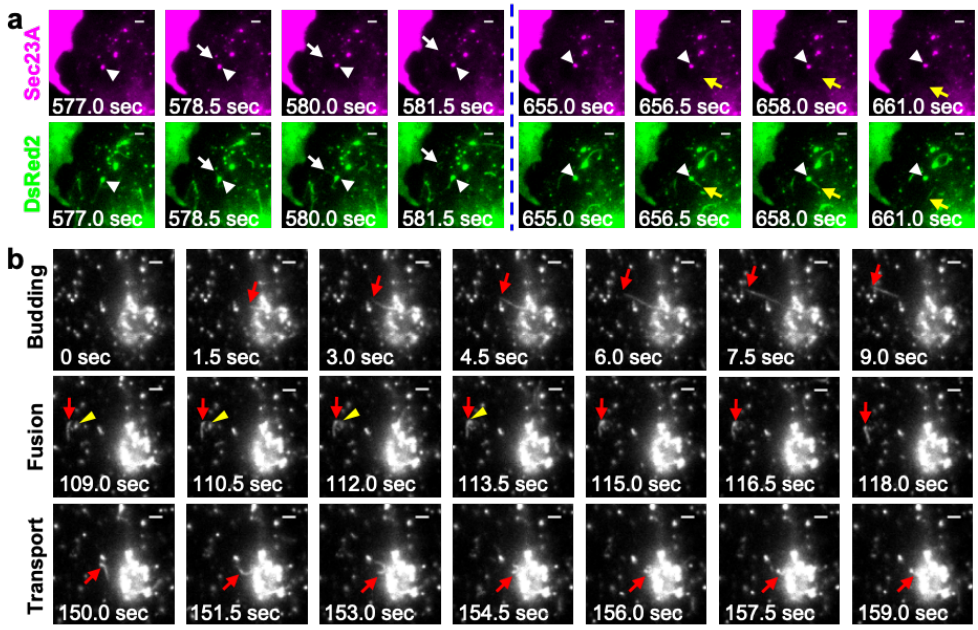

Figure 38: Dynamics of t-ERGIC for ER-to-Golgi trafficking. (a) RUSH image sequence showing that the same COPII-coated ERES (arrowhead) sequentially generates two t-ERGICs (white and yellow arrows) in opposite directions. 80 µM biotin was added at time 0. (b) RUSH image sequence showing that a t-ERGIC (arrow) buds from the Golgi apparatus, fuses with an ERES (arrowhead), and carries the cargo back to the Golgi apparatus. 80 µM biotin was added 30 min before time 0. Scale bars: 2 µm.

8.2.3 Fast ER-to-Golgi trafficking via the t-ERGIC is determined by the N-termini of soluble cargoes

Our unexpected discovery of t-ERGIC through DsRed2-ER-5 raises the question of why a similar construct, DsRed2-ER-3, localized predominantly in the ER (Figure 33bd). Given the small dissimilarities between the two constructs (Figure 33a), we wondered whether the property of the N-terminus after the signal-peptide cleavage (P1') could be important to the fate of the cargo protein. The N-terminus of the cleaved DsRed2-ER-5 begins with the hydrophobic APV tripeptide, whereas that of DsRed2-ER-3 starts with the charged DRS (Figure 33a). Consequently, we constructed a point mutant of DsRed2-ER-5, where the P1' alanine (A) was substituted by glutamic acid (E). Remarkably, this EPV-DsRed2-ER-5 variant (Figure 39a) phenocopied DsRed2-ER-3 (Figure 39bc), thus a good control for the original DsRed2-ER-5 (hereafter APV-DsRed2-ER-5) for our mechanistic investigations.

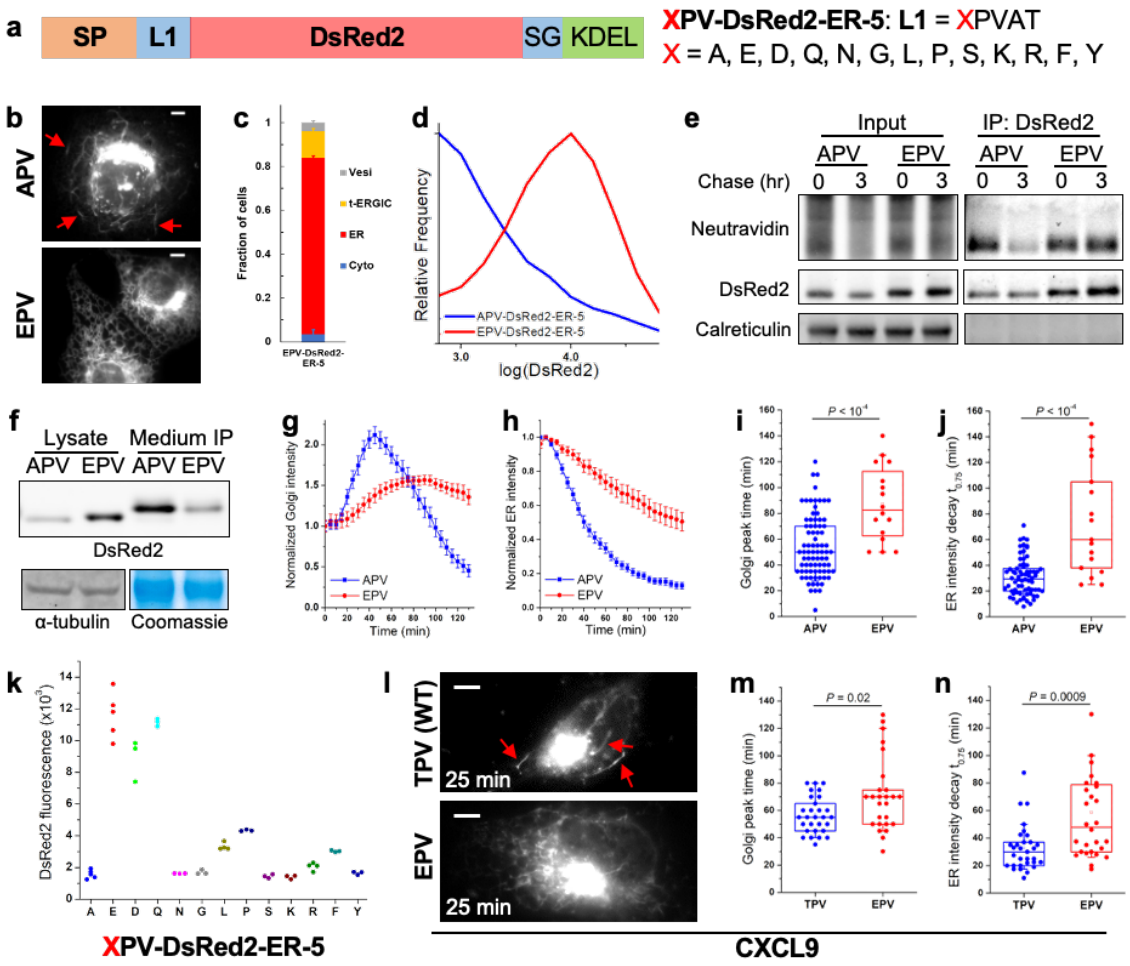

Figure 39: The N-terminus of the cargo determines its transport with the t-ERGIC and ER-to-Golgi trafficking efficiency. (a) Sequences of the XPV-DsRed2-ER-5 mutations we examined, with varied N-termini after the signal peptide (SP). The original DsRed2-ER-5 has X=A (APV-DsRed2-ER-5). (b) Representative fluorescence micrographs of APV/EPV-DsRed2-ER-5 in COS-7 cells. Arrows point to t-ERGICs. (c) Subcellular distribution of EPV-DsRed2-ER-5. Error bars: SEM (n = 3 with ~50 cells in each replicate). (d) Flow cytometry histograms of APV/EPV-DsRed2-ER-5. (e) Azidohomoalanine-biotin-alkyne pulse-chase of APV/EPV-DsRed2-ER-5. Newly synthesized proteins were labeled by azidohomoalanine click chemistry and detected by NeutrAvidin (see Materials and methods). (f) Immunoblots of intracellular (cell lysate) and secreted (anti-FLAG immunoprecipitation from the culture medium) APV/EPV-FLAG-DsRed2-ER-5. (g,h) Golgi (g) and peripheral ER (h) fluorescence intensity time traces of APV/EPV-SBP-DsRed2-ER-5 in RUSH, pooled from 70 cells from 5 independent runs (APV) or 17 cells from 3 independent runs (EPV). Error bars: SEM. 80 µM biotin was added at time 0. (i,j) Comparison of the time to the peak fluorescence in the Golgi (i) and the time of fluorescence decay to 75% of the start in the ER (j) of APV/EPV-SBP-DsRed2-ER-5 in RUSH. Whiskers and boxes show 10%, 25%, 50%, 75%, and 90% quantiles. (k) Median intracellular fluorescence of different XPV-DsRed2-ER-5 variants expressed in COS-7 cells, as determined by flow cytometry. (l) Representative fluorescence micrographs of TPV/EPV-CXCL9-mCherry-SBP in RUSH. 80 µM biotin was added at time 0. Arrows point to t-ERGICs. (m,n) Comparison of the time to the peak fluorescence in the Golgi (m) and the time of fluorescence decay to 75% of the start in the ER (n) of TPV/EPV-CXCL9-

mCherry-SBP in RUSH. Whiskers and boxes show 10%, 25%, 50%, 75%, and 90% quantiles. Scale bars: 5 μm. *P* values are calculated by two-tailed *t* test.

Flow cytometry of COS-7 cells transfected with APV-DsRed2-ER-5 and EPV-DsRed2-ER-5 showed markedly higher intracellular fluorescence for the latter (Figure 39d). Pulse-chase experiments indicated that the APV version was selectively removed from the cell (Figure 39e). With FLAG-tagged versions of APV/EPV-DsRed2-ER-5 (Figure 40a), which, without altering the APV/EPV phenotypes (Figure 40bc), facilitated immunoprecipitation from the culture medium, we next found substantially higher extracellular secretion and lower intracellular retention for the APV version (Figure 39f). Immunoblots of ER stress indicators indicated no noticeable activation (Figure 40d), suggesting that the different fates of the APV and EPV variants were attributed to physiological secretory pathways. Similar contrasting behavior of the two variants was observed in U2OS and HeLa cells (Figure 40e), as well as for APV/EPV variants of the GCaMP6s FP (Figure 40fg).

RUSH experiments showed that contrasting the fast, t-ERGIC-mediated ER-to-Golgi transport of APV-SBP-DsRed2-ER-5 (Figure 36d), EPV-SBP-DsRed2-ER-5 did not enter t-ERGIC and was slowly transported to the Golgi after biotin release (Figure 40h). Quantification of the fluorescence intensity in the Golgi area showed a substantially faster rise for the APV version after cargo release (Figure 39gi). Accordingly, fluorescence in the ER decayed significantly faster in the APV-transfected cells (Figure 39hj). These results demonstrate dramatic differences in the ER-to-Golgi transport pathway and efficiency between APV- and EPV-DsRed2-ER-5, which explain their different intracellular retentions at the steady state.

To further examine the effects of the cargo N-terminus, we compared 13 different amino acid residues at the P1' position (Figure 39a). Interestingly, we found DsRed2 to be strongly retained in the ER when glutamic acid (E), aspartic acid (D), or glutamine (Q) was present at the P1' position, but often entered the t-ERGIC and got exported out of the ER when the P1' position was other amino acids, including the structurally similar asparagine (N) (Figure 39k, 39ij).

To test whether this "N-terminus rule" for t-ERGIC-mediated ER export is relevant to endogenous proteins, we examined a normally secreted cytokine CXCL9, which has a native TPV P1' N-terminus. RUSH showed that the wild-type CXCL9 was transported via the t-ERGIC, whereas few t-ERGICs were involved in the trafficking of a mutant with an EPV N-terminus (Figure 39l). Concomitantly, substantially faster ER-to-Golgi transport was found for the former (Figure 39mn).

Collectively, our data indicate that a group of cargoes with explicit N-terminal features are routed to the t-ERGIC-mediated fast ER-to-Golgi trafficking pathway.

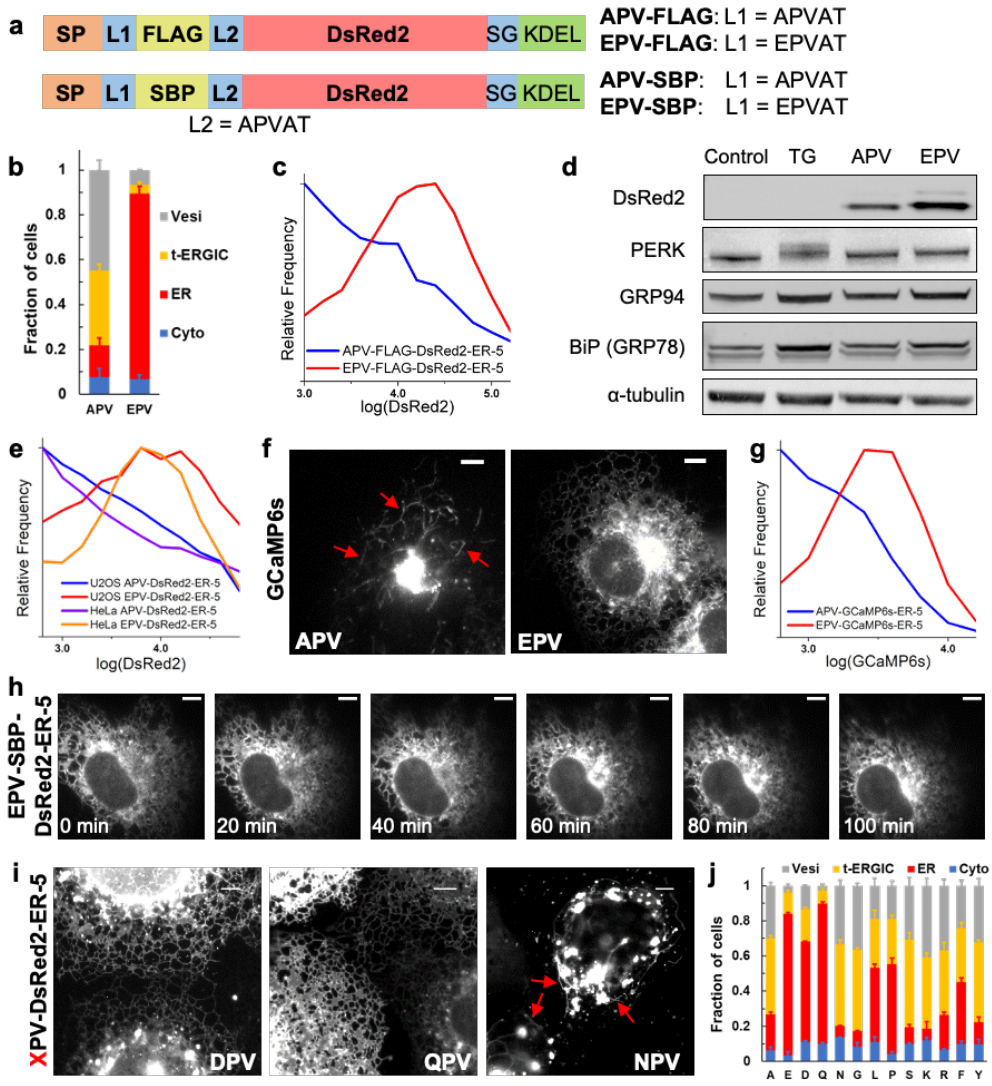

Figure 40: The N-terminus rule of ER-to-Golgi transport by t-ERGIC applies to different cargoes. (a) Sequences of APV/EPV-FLAG-DsRed2-ER-5 and APV/EPV-SBP-DsRed2-ER-5. (b,c) Subcellular distributions (b) and flow cytometry histograms (c) of APV/EPV-FLAG-DsRed2-ER-5. (d) Immunoblots of APV/EPV-DsRed2-ER-5-transfected cells and non-transfected cells with or without 1 μM thapsigargin (positive control for ER stress) treatment for 5 hr. (e) Flow cytometry histograms of APV/EPV-DsRed2-ER-5 in HeLa and U2OS cells. (f,g) Representative fluorescence micrographs (f) and flow cytometry histograms (g) of APV/EPV-GCaMP6s-ER-5 in COS-7 cells. (h) Representative RUSH image sequence of EPV-SBP-DsRed2-ER-5. 80 μM biotin was added at time 0. (i) Representative fluorescence micrographs of DPV/QPV/NPV-DsRed2-ER-5 in COS-7 cells. (j) Subcellular distributions of different XPV-DsRed2-ER-5 variants. The "A" and "E" data duplicates that of "ER-5" in Figure 33d and that of Figure 39c, respectively. Scale bars: 5 μm. Error bars: SEM (n = 3 with ~50 cells in each replicate). Arrows point to t-ERGICs.

8.2.4 The biogenesis and cargo selectivity of t-ERGIC both depend on SURF4

In search of an explanation for how a "D/E/Q but not N" N-terminus could have prevented the DsRed2 cargoes from entering the t-ERGIC, we noticed a recent study that reported an analogous

rule for protein secretion:[281] With a growth hormone cargo, it is found that D/E/Q-containing, but not N-containing, N-terminal tripeptides are unfavored for secretion mediated by the receptor SURF4, whereas hydrophobic-proline-hydrophobic (Φ-P-Φ) tripeptides are the most favored. Recent studies on SURF4 and its homologs have generally suggested its preference for hydrophobic N-termini.[275,282–284] Therefore, we set out to examine the role of SURF4 in the t-ERGIC pathway.

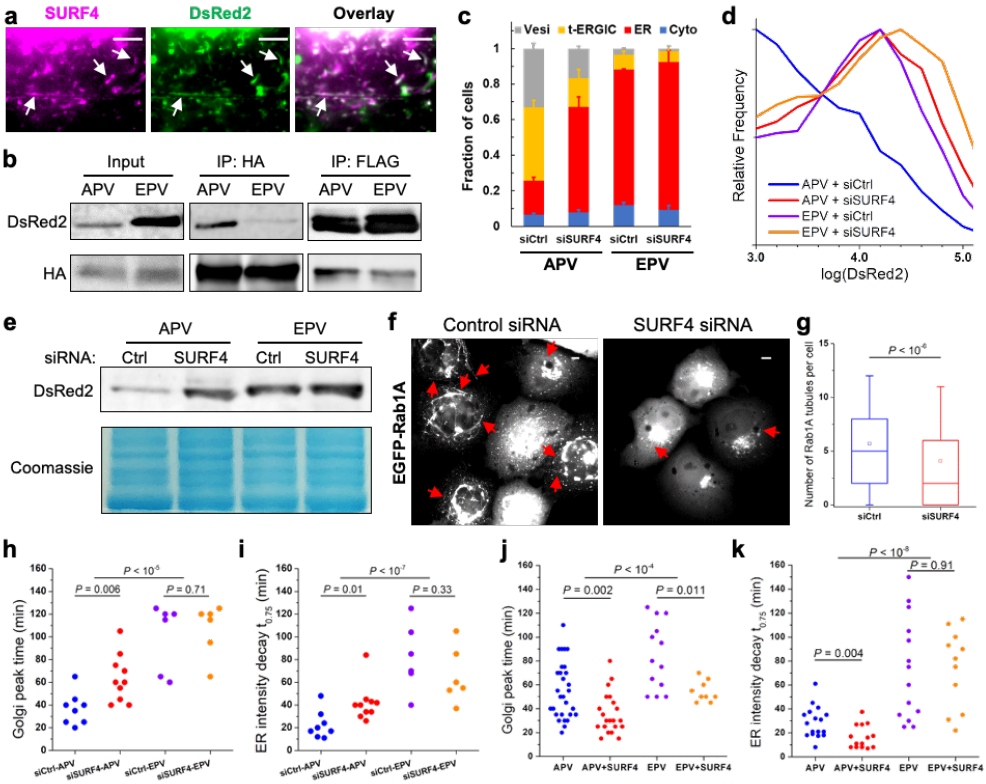

Figure 41: SURF4 recognizes the N-terminus of the cargo and enables t-ERGIC formation for expedited ER-to-Golgi trafficking. (a) Live-cell images of co-transfected AcGFP1-SURF4 and APV-DsRed2-ER-5 in a COS-7 cell. (b) Co-immunoprecipitation of APV/EPV-FLAG-DsRed2-ER-5 with co-expressed SURF4-HA. (c-e) Subcellular distributions (c), flow cytometry histograms (d), and lysate immunoblots (e) of APV/EPV-DsRed2-ER-5 for COS-7 cells co-transfected with control siRNA or SURF4 siRNA. Error bars: SEM (n = 3 with ~50 cells in each replicate). (f,g) Representative fluorescence micrographs (f) and counts per cell (g) of Rab1A-positive tubules in control or SURF4 siRNA-treated COS-7 cells. Whiskers and boxes show 10%, 25%, 50%, 75%, and 90% quantiles. Open squares indicate means. 287 and 321 cells were quantified for siCtrl and siSURF4, respectively. (h,i) Comparison of the time to the peak fluorescence in the Golgi (h) and the time of fluorescence decay to 75% of the start in the ER (i) of APV/EPV-SBP-DsRed2-ER-5 with control siRNA or SURF4 siRNA in RUSH. (j,k) Comparison of the time to the peak fluorescence in the Golgi (j) and the time of fluorescence decay to 75% of the start in the ER (k) of APV/EPV-SBP-DsRed2-ER-5 with or without co-expression of FLAG-SURF4 in RUSH. Scale bars: 5 μm. Arrows point to t-ERGICs. *P* values are calculated by Mann-Whitney test (g), two-way ANOVA (APV vs. EPV in [h-k]), or two-tailed *t* test (siRNA or SURF4 overexpression in [h-k]).

Live-cell imaging showed that AcGFP1-SURF4 colocalized with the t-ERGICs (Figure 41a). SURF4-HA co-immunoprecipitated much more efficiently with APV-FLAG-DsRed2-ER-5 than EPV-FLAG-DsRed2-ER-5, even as the input amount of the former was several-fold lower due to secretion (Figure 41b).

With small interfering RNA (siRNA) targeting SURF4 (Figure 42a), we next observed a substantial reduction in APV-DsRed2-ER-5 t-ERGICs (Figure 41c, 42b). The intracellular retention of APV-DsRed2-ER-5, as determined by both flow cytometry and immunoblotting, was also significantly enhanced (Figure 41de). In comparison, intracellular retention of the SURF4-unfavored EPV variant started high and was only mildly affected by the SURF4 siRNA (Figure 41de). Notably, in cells not expressing DsRed2 cargoes, SURF4 knockdown also markedly reduced the number of EGFP-Rab1A-labeled t-ERGICs (Figure 41fg). RUSH experiments further showed that SURF4 knockdown substantially decreased the trafficking rate of APV- but not EPV-SBP-DsRed2-ER-5 (Figure 41hi). Conversely, when FLAG-SURF4 was overexpressed, the ER-to-Golgi trafficking of APV-SBP-DsRed2-ER-5 was specifically accelerated (Figure 41jk).

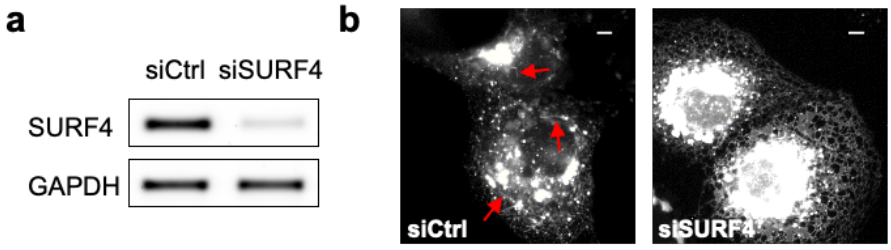

Figure 42: The efficacy of SURF4 siRNA treatment. (a) Reverse transcription (RT)-PCR of SURF4 mRNA in control and SURF4 siRNA-treated cells. (b) Representative live-cell images of APV-DsRed2-ER-5 in control and SURF4 siRNA-treated cells. Arrows indicate t-ERGICs. Scale bars: 5 μm.

Together, our results indicate that the biogenesis and cargo selectivity of t-ERGIC both depend on SURF4, thus explaining the peculiar "N-terminus rule" we identified for t-ERGIC-based ER-to-Golgi transport.

8.2.5 Co-clustering of SURF4 and cargo expands the ERES for t-ERGIC biogenesis

To examine how SURF4 facilitated t-ERGIC biogenesis, we utilized STORM to examine whether SURF4 cargoes were sequestered into a special ERES domain. With cells co-transfected with APV-DsRed2-ER-5 and EGFP-Sec23A and immunolabeled for Sec31A, STORM showed that at the ERES (colocalization of Sec23A and Sec31A), Sec31A formed cup-shaped cages (Figure 43ab). Markedly, STORM of APV-DsRed2-ER-5 in a second color channel showed that at the ERES, Sec31A cages that surrounded this SURF4 cargo (e.g., filled arrowheads in Figure 43b) were notably larger than those not loaded with the cargo (e.g., open arrowheads in Figure 43b). As larger ERESs could provide more membrane materials for forming the long t-ERGIC tubules, this observation (statistics in Figure 43c) may explain the specificity of t-ERGIC to SURF4 cargoes. SURF4 siRNA treatment substantially reduced the occurrence of large (>~250 nm) Sec31A cups and hence removed the size difference between DsRed2-loaded and non-loaded ERESs (Figure 44), suggesting that SURF4 is necessary for the ERES enlargement in t-ERGIC biogenesis.

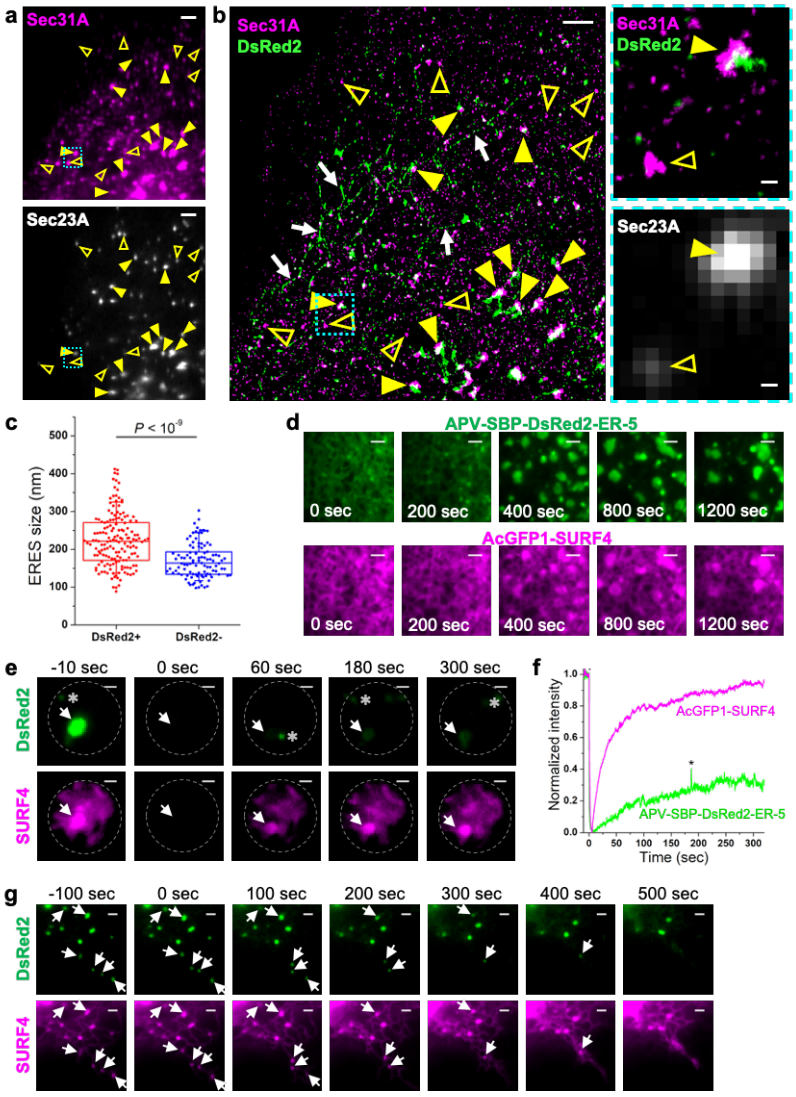

Figure 43: SURF4 co-clusters with its cargo to expand the ERES. (a) Epifluorescence of immunolabeled Sec31A (top) and EGFP-Sec23A (bottom) in a COS-7 cell co-expressing EGFP-Sec23A and APV-DsRed2-ER-5. (b) Two-color STORM image of Sec31A and APV-DsRed2-ER-5 for the same view as (a) (left), as well as zoom-ins (right) of the cyan-boxed region of the STORM image and the EGFP-Sec23A epifluorescence image. Yellow arrowheads in (a,b) indicate examples of ERES labeled with both EGFP-Sec23A and Sec31A. Filled and open arrowheads indicate DsRed2-loaded and non-loaded ERESs, respectively. Arrows in (b) indicate t-ERGICs. (c) Statistics of the sizes of DsRed2-loaded and non-loaded, Sec23A-positive ERESs, based on the STORM-determined sizes of the Sec31A clusters. Whiskers and boxes show 10%, 25%, 50%, 75%, and 90% quantiles. *P* value is calculated by a two-tailed *t* test. n = 5 STORM images were quantified. (d) Representative RUSH image sequence showing the formation and fusion of LLPS-like domains of co-clustered AcGFP1-SURF4 and APV-SBP-DsRed2-ER-5. Biotin was added at time 0 for cargo release. (e) Dual-color FRAP image sequence of AcGFP1-SURF4 and APV-SBP-DsRed2-ER-5 in a condensate. The gray circle indicates the illuminated area as defined by a pinhole. Asterisks mark random DsRed2-containing vesicles entering the illuminated area. 80 μM biotin was added at -30 min. (f) Fluorescence recovery time trace for the condensate pointed to by

the arrow in (e). (g) Dissolution of the AcGFP1-SURF4 and APV-SBP-DsRed2-ER-5 condensates in RUSH by adding 3% 1,6-hexanediol at time 0. Arrows mark the gradually dissolved condensates. 80 μM biotin was added at -30 min. Scale bars: 2 μm (a,b,d,g); 200 nm (zoom-ins of b); 1 μm (e).

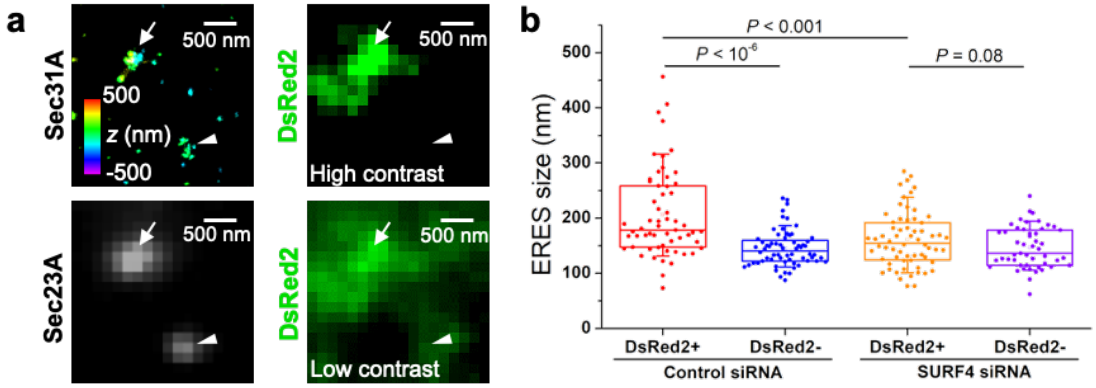

Figure 44: ERES expansion diminishes with SURF4 siRNA. (a) DsRed2-loaded (arrow) and non-loaded (arrowhead) ERESs in a SURF4 siRNA-treated cell. Sec31A is shown in 3D-STORM, and epifluorescence of EGFP-Sec23A and APV-DsRed2-ER-5 are shown in gray and green, respectively. Note that with SURF4 knockdown, the APV-DsRed2-ER-5 cargo no longer clustered strongly at the ERES, so that DsRed2-loaded and non-loaded ERESs were subjectively assigned based on enhanced contrast of the epifluorescence image. (b) Statistics of the sizes of DsRed2-loaded and non-loaded, Sec23A-positive ERESs, based on the STORM-determined sizes of the Sec31A clusters, in control and SURF4 siRNA-treated cells. Whiskers and boxes show 10%, 25%, 50%, 75%, and 90% quantiles. *P* values are calculated by the two-tailed *t* test. n = 4 STORM images were quantified.

To further understand how SURF4 expanded ERES, we turned to live-cell RUSH assay. Upon the release of APV-SBP-DsRed2-ER-5 by biotin, we observed the co-clustering of this cargo with AcGFP1-SURF4 at the ERES, as well as their co-translocation into the fast-moving t-ERGIC. However, the transient nature of the cargo-loaded ERES impeded detailed characterization. Interestingly, in a fraction (~20%) of the cells characterized by high expression levels, we observed that after the release of cargo by biotin, SURF4 and the cargo co-clustered to form gradually expanding domains in the ER (Figure 43d). 3D-STORM of fixed cells showed that SURF4 and the cargo were both membrane-associated at the expanded clusters (Figure 45). These membrane-bound clusters (condensates) showed liquid-like properties as found in liquid-liquid phase separation (LLPS),[285] including their quasi-circular appearance and growth by fusion (Figure 43d). After ~15 min, the fusion between the SURF4-cargo condensates slowed down, which offered us an opportunity to examine their physical properties in live cells.

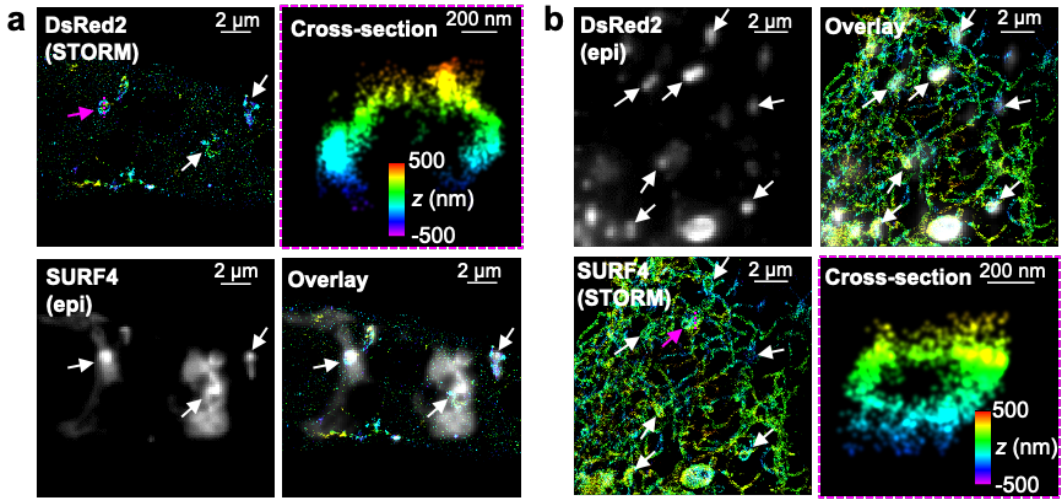

Figure 45: SURF4 and its cargo condensates on the ER membrane. 3D-STORM of immunolabeled APV-SBP-DsRed2-ER-5 (a) or AcGFP1-SURF4 (b), in comparison with epifluorescence images of AcGFP1-SURF4 (a) or APV-SBP-DsRed2-ER-5 (b) of the same views in a RUSH experiment. For cargo release, 80 µM biotin was added 40 min before sample fixation. Arrows indicate SURF4 and DsRed2 condensates. Vertical cross-sections of the STORM images are given for the condensates indicated by the magenta arrows, showing membrane localizations for both proteins. Colors in the 3D-STORM images encode axial positions (depth).

We first applied fluorescence recovery after photobleaching (FRAP) to examine the dynamics of SURF4 and cargo in these condensates. Intriguingly, upon photobleaching, whereas the AcGFP1-SURF4 fluorescence quickly recovered in ~1 min, APV-SBP-DsRed2-ER-5 exhibited slow and incomplete recovery (Figure 43ef). This result may be understood as that as SURF4 and its cargo dynamically bound and unbound at the ERES, an excessive amount of the former prevented the diffusion of the latter. We next tested whether the SURF4-cargo condensates could be disrupted by 1,6-hexanediol, an amphiphilic small molecule widely used in LLPS characterizations.[286] We thus found that as AcGFP1-SURF4 and APV-SBP-DsRed2-ER-5 started to cluster, the addition of 3% 1,6-hexanediol led to gradual, yet always concurrent dissolution of the SURF4 and DsRed2 condensates, so that only a few larger ones persisted after ~400 s (Figure 43g). Together, our results suggest that the co-clustering of SURF4 and cargo provides an LLPS-related mechanism to expand the ERES to facilitate t-ERGIC biogenesis.

8.2.6 Antagonism between SURF4 and KDEL receptors regulates the steady-state location of cargo proteins

While we have elucidated how soluble proteins of different N-termini were differentially selected by SURF4 for entering the t-ERGIC secretion pathway, further experiments indicated another layer of complexity. Specifically, whereas we showed above that APV-DsRed2-ER-5 and APV-GCaMP6s-ER-5 both mainly localized to t-ERGIC tubules at the steady state, analogous constructs of other FPs, including Dendra2, mOrange2, mCherry, EGFP, and mEmerald, mainly localized to the ER and had only ~10% cells dominated by fluorescence in the t-ERGIC (Figure 46ab).

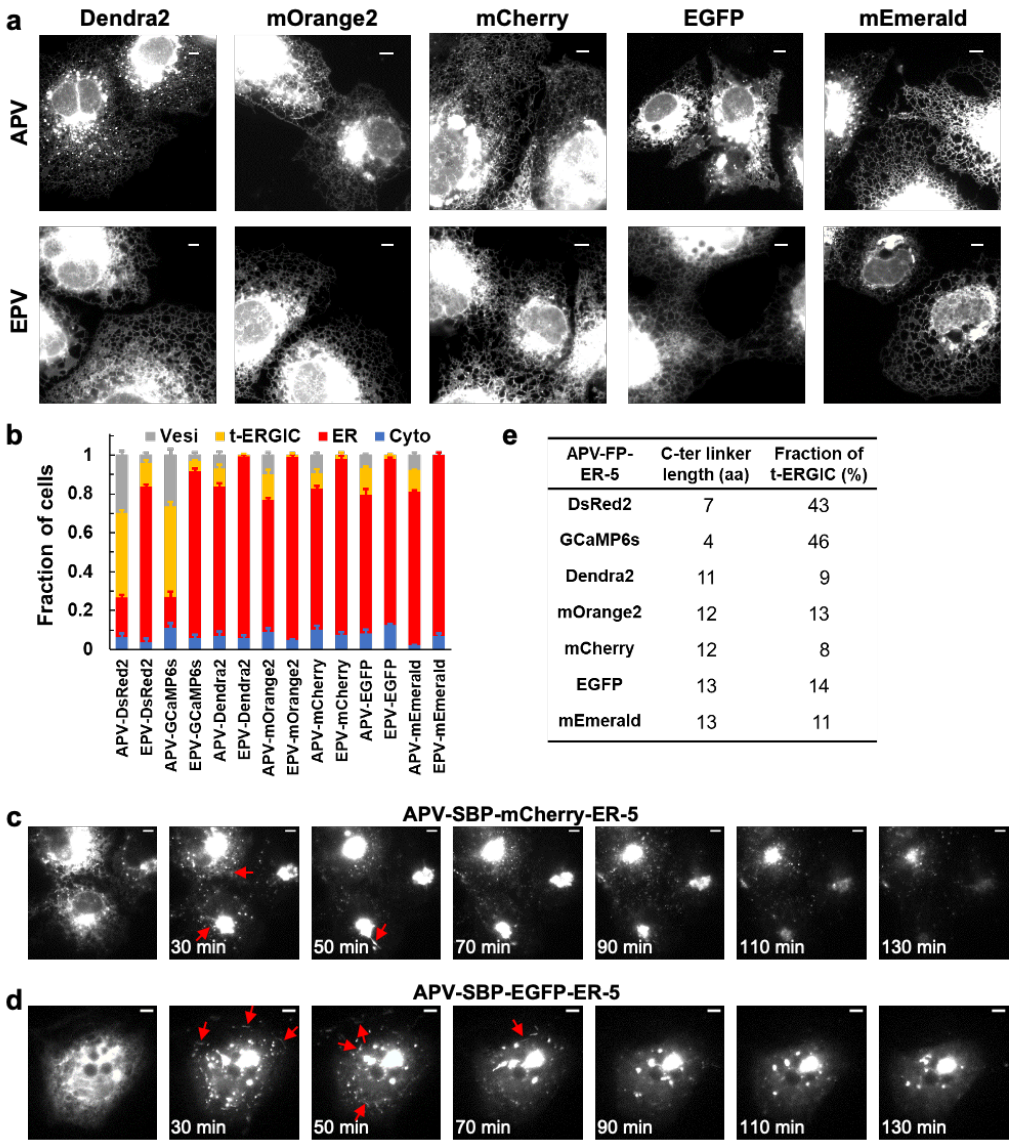

e

APV-FP-ER-5	C-ter linker length (aa)	Fraction of t-ERGIC (%)
DsRed2	7	43
GCaMP6s	4	46
Dendra2	11	9
mOrange2	12	13
mCherry	12	8
EGFP	13	14
mEmerald	13	11

Figure 46: Distinct steady-state localizations of different FP-ER-5 constructs. (a) Representative fluorescence micrographs of APV/EPV-Dendra2-ER-5, APV/EPV-mOrange2-ER-5, APV/EPV-mCherry-ER-5, APV/EPV-EGFP-ER-5, and APV/EPV-mEmerald-ER-5 in COS-7 cells. (b) Subcellular distributions of different APV/EPV-FP-ER-5 constructs. The APV-DsRed2 and EPV-DsRed2 data duplicate that of "ER-5" in Figure 33d and that of Figure 39c, respectively. Error bars: SEM (n = 3 with ~50 cells in each replicate). (c,d) RUSH image sequences of APV-SBP-mCherry-ER-5 (c) and APV-SBP-EGFP-ER-5 (d) showing efficient ER exit and the formation of t-ERGIC. Arrows indicate t-ERGICs. (e) Table summarizing the C-terminal linker lengths and the fractions of t-ERGIC-predominant cells for different APV-FP-ER-5 constructs. See Materials and methods for detail. Scale bars: 5 μm.

Curiously, RUSH experiments on APV-SBP-FP-ER-5 showed that upon cargo release, all FPs were efficiently trafficked to the Golgi via t-ERGIC (Figure 46cd). Thus, although all FP cargoes entered the t-ERGIC pathway, other factors modulated their steady-state location. One possibility is that the cargoes were differentially retrieved back from the Golgi to the ER. As the Golgi-to-ER

transport is often mediated by KDEL receptors (KDELRs), which recognize KDEL-like motifs at the cargo C-termini,[287,288] we compared APV-mEmerald-DsRed2-ER-5 and APV-DsRed2-mEmerald-ER-5, which respectively had C-termini identical to that of APV-DsRed2-ER-5 and APV-mEmerald-ER-5 (Figure 47a). Remarkably, at the steady state, we found the former was often in the t-ERGIC (Figure 47b), whereas the latter was mainly in the ER (Figure 47b) and was better retained in the cell (Figure 47a).

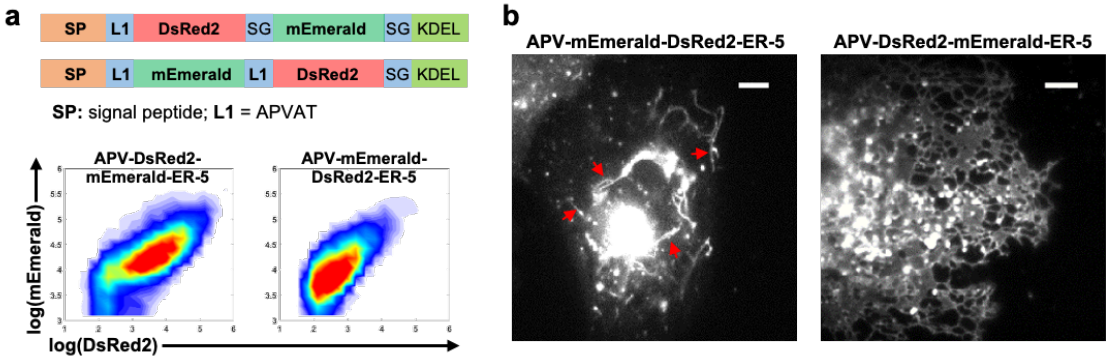

Figure 47: Distinct behavior of APV-DsRed2-mEmerald-ER-5 and APV-mEmerald-DsRed2-ER-5. (a) Sequences and flow cytometry of APV-DsRed2-mEmerald-ER-5 and APV-mEmerald-DsRed2-ER-5. (b) Representative fluorescence micrographs of APV-DsRed2-mEmerald-ER-5 and APV-mEmerald-DsRed2-ER-5 in COS-7 cells. Scale bars: 5 μm. Arrows indicate t-ERGICs.

To rationalize how the C-termini of APV-DsRed2-ER-5 and APV-mEmerald-ER-5, which both ended with KDEL, could interact differently with KDELRs, we noted that recent structural analysis indicates that the KDELR binding pocket is largely buried inside the membrane.[289] It is thus possible that the binding efficiency of KDELRs may depend on how well the C-terminus KDEL motifs are exposed. Indeed, as we examined the linker between the folded FP core and the C-terminus KDEL motif, we found that the DsRed2 and GCaMP6s constructs had much shorter linkers when compared to the other FPs (Figure 46e, Materials and methods).

To test whether this linker length could be significant, we inserted into APV-DsRed2-ER-5 three different sequences (FLAG-tag of 8 aa, HA-tag of 9 aa, and a random 18-aa linker) between the DsRed2 C-terminus and the KDEL motif (Figure 48a). Remarkably, these constructs of extended pre-KDEL linkers all mainly localized to the ER (Figure 48bc) and showed substantially increased intracellular retention (Figure 48d). Co-immunoprecipitation showed that the C-terminally extended cargo indeed interacted with the KDELR much more strongly when compared to control constructs in which the same extension was added to the N-terminus (Figure 48e). Conversely, as we truncated 10 C-terminal residues before the KDEL motif in APV-EGFP-ER-5, increased t-ERGIC presence of the cargo was observed (Figure 49ab) together with reduced intracellular retention (Figure 49c). Together, our results suggest that the efficacy of KDELR-mediated Golgi-to-ER transport, and hence the steady-state localization of cargoes, depend on how well the C-terminus KDEL motif is exposed.

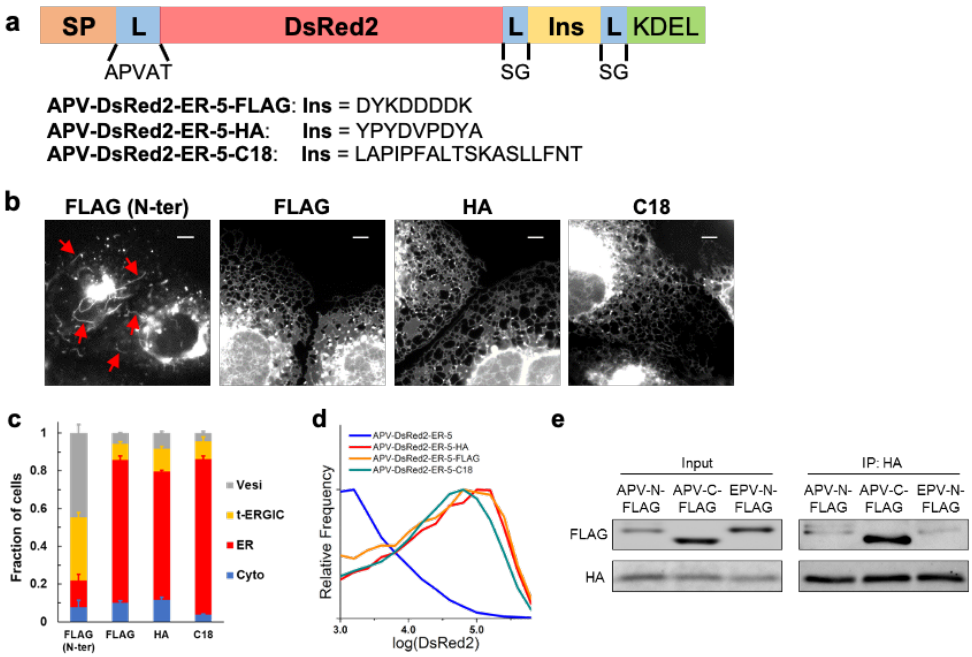

Figure 48: C-terminal extension of KDEL enhances ER retrieval. (a) Schematics of different C-terminal insertions of APV-DsRed2-ER-5. (b) Representative fluorescence micrographs of APV-FLAG-DsRed2-ER-5, APV-DsRed2-ER-5-FLAG, APV-DsRed2-ER-5-HA, and APV-DsRed2-ER-5-C18 in COS-7 cells. Scale bars: 5 μm. Arrows indicate t-ERGICs. (c,d) Subcellular distributions (c) and flow cytometry histograms (d) of APV-(FLAG-)DsRed2-ER-5 and its C-terminal inserted derivatives. The "FLAG (N-ter)" data in (c) duplicates "APV" in Figure 40b. Error bars: SEM (n = 3 with ~50 cells in each replicate). (e) Co-immunoprecipitation of APV-FLAG-DsRed2-ER-5, APV-DsRed2-ER-5-FLAG, and EPV-FLAG-DsRed2-ER-5 with KDELR3-HA.

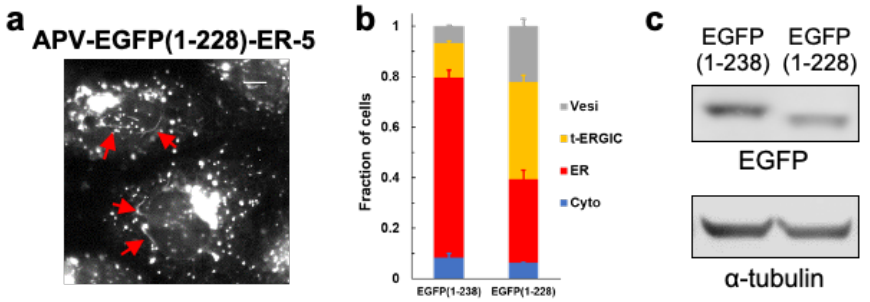

Figure 49: C-terminal truncation of APV-EGFP-ER-5 reduces ER retrieval. (a) Representative fluorescence micrograph of APV-EGFP(1-228)-ER-5 in COS-7 cells, showing t-ERGICs. Scale bar: 5 μm. Arrows indicate t-ERGICs. (b,c) Subcellular distributions (b) and immunoblots (c) of APV-EGFP(1-238)-ER-5 and the C-terminally truncated APV-EGFP(1-228)-ER-5. Error bar: SEM (n = 3 with ~50 cells in each replicate). The APV-EGFP(1-238)-ER-5 subcellular distribution in (b) duplicates "APV-EGFP-ER-5" in Figure 46b.

Notably, although the C-terminally extended APV-DsRed2-ER-5-HA mainly localized to the ER, co-imaging with EGFP-Rab1A showed that it also populated Rab1A-positive t-ERGICs (Figure 50a), whereas EPV-DsRed2-ER-5-HA did not (Figure 50b). Moreover, as we overexpressed

FLAG-SURF4 in cells expressing APV-mOrange2-ER-5, more cells were characterized by fluorescence in the t-ERGICs (Figure 51a), and the intracellular retention decreased (Figure 51bc). Thus, the N-terminal SURF4 signal and the C-terminal KDELR signal independently promote anterograde and retrograde trafficking, and thus antagonistically regulate the steady-state localization and retention of the cargo.

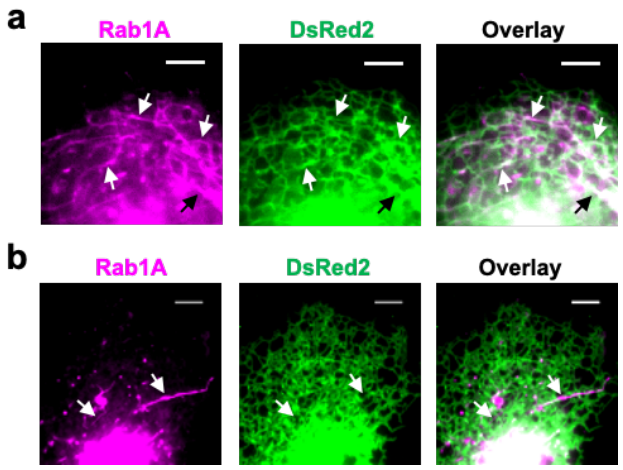

Figure 50: Enhanced ER retrieval is independent of t-ERGIC biogenesis. Dual-color live-cell fluorescence micrographs of APV-DsRed2-ER-5-HA (a) or EPV-DsRed2-ER-5-HA (b) and EGFP-Rab1A in co-transfected cells. Scale bar: 5 µm. Arrows indicate t-ERGICs.

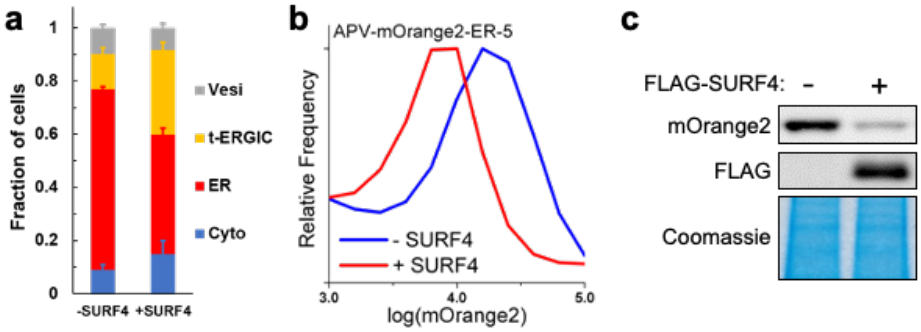

Figure 51: Overexpression of SURF4 overrides KDEL-mediated ER retrieval. Subcellular distribution (a), flow cytometry histograms (b), and lysate immunoblots (c) of APV-mOrange2-ER-5 in COS-7 cells with or without the co-expression of FLAG-SURF4. Error bars: SEM (n = 3 with ~50 cells in each replicate).

8.2.7 Discussion

Although the molecular diversity of cargo-receptor interactions in the early secretory pathways have been extensively characterized biochemically, their cell biological consequences, including the diversity of cargo carriers and the differential transport kinetics, are less understood.[253–255] Our results showed that SURF4-cargo interactions give rise to a morphologically and functionally distinct compartment that specifically expedites the ER-to-Golgi transport of SURF4 cargoes (Figure 52a).

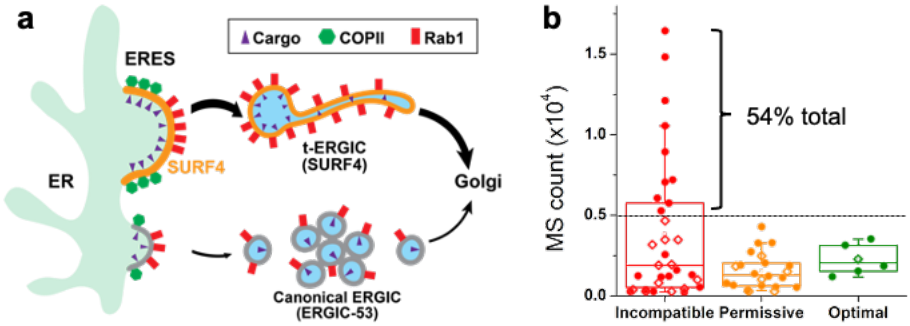

Figure 52: SURF4-mediated t-ERGIC transport leads to differential protein trafficking rates and steady-state localizations. (a) Working model of differential ER-to-Golgi trafficking via the SURF4-mediated t-ERGIC vs. the canonical ERGIC. (b) Categorization of the mass spectrometry counts of ER-lumen proteins in the HeLa cell,[290] based on the N-terminal tripeptide, into SURF4-incompatible (D/E/Q-containing), optimal (Φ-P-Φ), and permissive (others). Proteins with and without KDEL-like motifs[291] are marked by filled circles and open diamonds, respectively.

Whereas studies in yeasts suggest the budding off of COPII-coated vesicles at the ERES as ER-to-Golgi carriers,[252,253,258] live imaging of mammalian cells has shown COPII coats stably associate with the ER.[272,274,292,293] Our RUSH results are in line with the latter observations. This contrasting behavior may be attributed to the lack of ERGIC in model yeasts, thus highlighting the importance of ERGIC in relaying and sorting cargoes for the much larger mammalian cells.

Early electron microscopy studies depict ERGICs as VTCs with ~100 nm tubular buds extending from vesicular bodies.[262,263] The abundance of ERGIC-53 in the VTCs has since made it a canonical marker for ERGIC.[259–261] Although ERGIC-53-positive and ERGIC-53-negative tubular carriers of >2 µm lengths have been observed for certain cargoes,[267–272,280] it remains unclear what cargo features and/or their molecular interactions lead to this phenotype. Our results showed that the cargo receptor SURF4 defines an ERGIC-53-negative ERGIC domain that is morphologically distinct from VTCs, being ~10 µm long and <30 nm in diameter.

While lacking ERGIC-53, the t-ERGIC is enriched with Rab1. Rab1 plays key roles in ER-to-Golgi trafficking by recruiting motors to enable budding and effectors to mediate targeting and fusion.[294,295] Our RUSH experiments showed the accumulation and co-budding of Rab1 with the cargo at the ERES for both the de novo generation and fusion-elongation of the t-ERGIC, and that a dominant negative Rab1A mutant abolished t-ERGIC generation. These results echo previous findings that Rab1 is indispensable for cargo export,[277–279] as well as recent experiments reporting the ERES accumulation and co-budding of Rab1 into Golgi-bound carriers.[272,274]

The biogenesis of the extraordinarily long t-ERGIC demands a large amount of membrane materials. STORM showed that ERESs loaded by SURF4 cargoes were considerably larger. Moreover, as we depleted SURF4, the enlarged ERESs disappeared and the number of t-ERGIC in the cell diminished. Though a similar drop in ERES size has been noticed with SURF4 knockdown in *Caenorhabditis elegans*, the molecular mechanisms remain unclear.[296] With RUSH live-cell imaging, we captured the gradual expansion of the ERES after cargo release. In particular, for cells with high expression levels, we observed the co-clustering of SURF4 and cargo at large, stable domains characteristic of membrane-bound LLPS condensates. Although the structure of

SURF4 is unresolved, recent work has shown that SURF4 oligomerizes in vivo,[297] thus implying possible multivalent interactions required by LLPS.[298]

Whereas ERES expansion via SURF4-cargo interactions provides a potential mechanism for t-ERGIC generation, additional machineries await to be identified to explain the recruitment of Rab1, which we showed to enable both the ERES budding of new t-ERGICs and the fusion with pre-existing t-ERGICs. Packing more cargoes into an existing t-ERGIC is potentially more efficient than transporting many smaller vesicles. The accumulation of membrane materials through the continued fusion with more ERESs also explains how the very long t-ERGICs could form. The extreme lengths and thinness of these carriers may be natural consequences of the Rab1-recruited motors,[299] which rapidly pulled the t-ERGICs along the microtubules.

By systematically comparing the behavior of different cargo proteins under native, SURF4-depleted, and SURF4-overexpressed conditions, we showed that SURF4 selectively routed its cargoes to the t-ERGIC for accelerated ER-to-Golgi transport. Whereas it has been recognized that the SURF4-mediated transport is substantially faster than the bulk flow,[253,275,281–284,296,300,301] our results unveiled that SURF4 establishes a distinct ERGIC form to facilitate this process. By virtue of its *en bloc* cargo packaging, high moving speed, and fast recycling capability, the t-ERGIC provides an efficient trafficking pathway. With its extremely elongated shape and hence high surface-to-volume ratio, the t-ERGIC may be particularly efficient for the transport of receptor-bound cargoes at the membrane while minimizing the nonspecific trafficking of other soluble proteins in the lumen.[260]

While our RUSH results showed that SURF4 cargoes consistently entered the t-ERGICs for rapid ER-to-Golgi transport, at the steady state some cargoes localized more strongly to the ER, even though Rab1 co-labeling showed that they entered t-ERGICs. Whereas KDELRs provide a well-studied mechanism for retrograde trafficking,[254] we unveiled an interesting effect, in which the C-terminal KDEL motif was less accessed by the KDELRs when closely linked to a well-folded core. Extending this linker substantially increased the KDEL-KDELR affinity, under which condition the cargo became more localized to the ER. Overexpressing SURF4 tipped this balance again and led to more pronounced localization of the cargo in the t-ERGIC at the steady state and decreased ER retrieval. Together, we thus showed that the N-terminus-selective, SURF4-mediated t-ERGIC fast route for ER-to-Golgi transport may be counterbalanced by the C-terminal ER-retrieval signal for regulating the spatiotemporal distribution of the cargo.

For ER-resident soluble proteins, one may thus expect that the SURF4 signal to be negatively selected. We surveyed the N-terminal tripeptides of the ER-resident proteome based on a subcellular fractionation-mass spectrometry dataset of HeLa cells.[290] Notably, out of the 61 annotated ER-lumen proteins, the 10 most abundant ones, making up 54% of the total, all have SURF4-incompatible N-termini together with KDEL-like C-terminal motifs (Figure 52b). Low SURF4-binding affinity may thus have been evolutionarily selected for the abundant ER-resident proteins.[281] Intriguingly, our analysis also identified ER-resident proteins with SURF4-optimal N-termini (Figure 52b). Although 5 out of these 6 proteins have KDEL-like ER retrieval motifs,[291] a survey of the literature and our immunofluorescence images both indicated the substantial presence of these proteins outside the ER in the Golgi, vesicles, and the extracellular space.[302–304] Of note, immunolabeled endogenous calumenin colocalized with EGFP-Rab1A-marked t-ERGIC

(Figure 53), thus suggesting antagonistic trafficking may be utilized by the cell to enrich proteins in the intermediate organelles along secretory pathways.

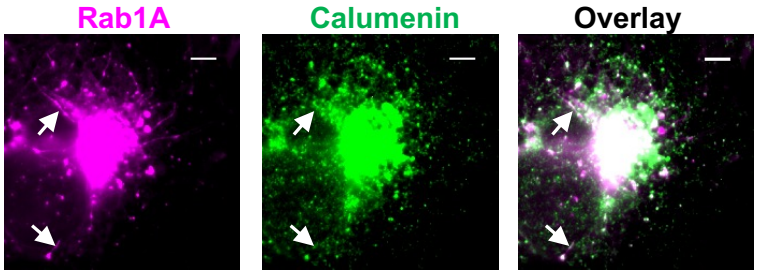

Figure 53: Calumenin localizes to the t-ERGIC. Immunofluorescence of endogenous calumenin vs. fluorescence micrograph of EGFP-Rab1A in a COS-7 cell. Scale bars: 5 µm. Arrows point to t-ERGICs.

8.3 Conclusion

In summary, by identifying t-ERGIC as a SURF4-mediated, morphologically and functionally distinct compartment that specifically expedites the ER-to-Golgi transport of SURF4 cargoes, our results argue that specific cargo-receptor interactions give rise to distinct transport carriers, which in turn regulate the ER-to-Golgi trafficking kinetics. Given the diversity of cargo receptors, it remains open whether other receptor-cargo interactions may produce yet other ERGIC forms. Meanwhile, the antagonism between the N-terminal ER export and C-terminal ER retrieval signals unveiled in this work demonstrates how the cargo primary structure may be utilized to achieve exquisite, hierarchical controls of protein trafficking and localization.

8.4 Materials and methods

Cell culture

COS-7, U2OS, and HeLa cells were obtained from the Cell Culture Facility at University of California Berkeley. Cells were cultured in Dulbecco's Modified Eagle Medium (DMEM, Gibco 31053-028) supplemented with 10% fetal bovine serum (FBS, Gibco A3160401), 1x GlutaMax (Gibco 35050061), and 1x non-essential amino acids (Gibco 11140050) at 37°C, 5% CO_2, and ambient oxygen. Lipofectamine 3000 (Invitrogen L3000008) was used for transient transfection according to the manufacturer's protocol. In general, cells were plated 20-24 hr before transfection to reach 60%-70% confluency. A total of 1 µg plasmid was used for each sample in a 12-well plate (Corning 3513). Experiments were performed 20-24 hr post-transfection, except for RUSH, where the plasmids were expressed for 40-48 hr to ensure adequate expression.

Plasmids

The following plasmids were from Addgene: pDendra2-ER-5 (57716), pmEmerald-ER-3 (54082), pAcGFP1-Sec61β (15108), pEGFP-ERGIC-53 (38270), pEGFP-Rab1A (49467), pEGFP-Rab5B (61802), pEGFP-Rab11A (12674), pEGFP-Rab7A (12605), pClover-LAMP1 (56528), pEGFP-p62 (38277), pEGFP-Sec23A (66609), pStr-KDEL_SBP-EGFP-Ecadherin (65286).

The following plasmids were synthesized by Twist Bioscience: pTwist-CMV BetaGlobin-KDELR3-HA (HA inserted between E143 and A144 of human KDELR3), pTwist-CMV BetaGlobin-SURF4-HA (HA inserted between D263 and K265 of human SURF4).

The Golgi-GFP BacMam construct was from Thermo Fisher (Invitrogen C10592), and was transduced following the manufacturer's protocol.

pDsRed2-ER-5 was constructed from pDendra2-ER-5 by replacing Dendra2 with DsRed2 using the AgeI and Kpn2I sites. The EPV construct (A18E mutation of APV-DsRed2-ER-5) was generated by changing the alanine codon (GCA) to a glutamate codon (GAA) using the BmtI and AgeI sites of the ER-5 plasmids. N-terminal tags (SBP, FLAG) were inserted using the AgeI site, duplicating the APVAT/EPVAT linker. Other A18X mutations were generated in a similar manner. C-terminal tags (HA, FLAG, C18) were inserted using the Kpn2I site, duplicating the SG linker. Other pFP-ER-5 plasmids were generated by replacing DsRed2 with corresponding FPs. pDsRed2-ER-3 was constructed from pmEmerald-ER-3 by replacing mEmerald-KDEL with DsRed2-KDEL using the AgeI and EcoRI sites. pAcGFP1-ERGIC-53 (high expression) and pAcGFP1-SURF4 were constructed by replacing Sec61β of pAcGFP1-Sec61β with ERGIC-53 or SURF4 using the Kpn2I and SalI sites. pStr-KDEL_APV/EPV-SBP-DsRed2-ER-5 was constructed by replacing SBP-EGFP-Ecadherin of pStr-KDEL_SBP-EGFP-Ecadherin with APV/EPV-SBP-DsRed2-ER-5 using the AscI and XbaI sites. pHaloTag-Sec23A was constructed by replacing EGFP of pEGFP-Sec23A with HaloTag using AgeI and Kpn2I sites. pStr-KDEL_TPV-CXCL9-mCherry-SBP was constructed by inserting the synthesized human CXCL9-mCherry-SBP (Twist Bioscience) in between the AscI and XbaI sites. The TPV-to-EPV mutation was generated by PCR between the intrinsic BsrGI site and the XbaI site. pStr-KDEL_APV-Dendra2/mCherry/EGFP-ER-5 was constructed by the Gibson assembly (New England BioLabs E2611) of pStr-KDEL_SBP-EGFP-Ecadherin linearized by AscI and XbaI, PCR-amplified calreticulin signal peptide-SBP tag, and PCR-amplified Dendra2/mCherry/EGFP-SGKDEL. pFLAG-SURF4 was constructed by inserting PCR-amplified FLAG-SURF4 from COS-7 cDNA between the BmtI and EcoRI sites of pDsRed2-ER-5. pAPV-DsRed2-mEmerald-ER-5 and pAPV-mEmerald-DsRed2-ER-5 were made by inserting mEmerald into pDsRed2-ER-5 using the Kpn2I site and the AgeI site, respectively. pAPV-EGFP(1-228)-ER-5 was constructed by replacing the full-length EGFP of pAPV-EGFP-ER-5 with EGFP(1-228) using the AgeI and Kpn2I sites.

All constructed plasmids were prepared from DH5α, XL1-Blue, or Stbl3 cells (from University of California Berkeley QB3 MacroLab) using the QIAprep Spin Miniprep kit (QIAGEN 27106). Protein-coding sequences were verified by Sanger sequencing at UC Berkeley DNA Sequencing Facility.

Antibodies

The following secondary antibodies were conjugated in house using previously described protocol:[56] goat anti-mouse (Jackson ImmunoResearch 715-005-151)-CF568 (Biotium 92131), goat anti-mouse IgG2b (Jackson 115-005-207)-Alexa Fluor 647 (A37573), goat anti-mouse IgG1 (Jackson ImmunoResearch 115-005-205)-CF568, goat anti-chick (Jackson ImmunoResearch 703-005-155)-Alexa Fluor 488 (Invitrogen A20000). These antibodies (0.3-0.4 mg/mL) were used at 1:60 dilution for immunofluorescence and 1:300 for immunoblotting.

The following antibodies and dilutions were used for immunofluorescence: rabbit anti-β-COP (Invitrogen PA1-061, 1:100), rabbit anti-Rab1A (Cell Signaling Technology 13075, 1:50), rabbit anti-Rab1B (Proteintech 17824-1-AP, 1:40), mouse anti-DsRed (Santa Cruz 390909, 1:100), rabbit anti-FLAG (Cell Signaling Technology 14793, 1:500), rabbit anti-Sec31A (Proteintech 17913-1-AP, 1:200), mouse anti-calumenin (Santa Cruz 271357, 1:30), rabbit anti-GFP-Alexa Fluor 647 (Invitrogen A31852, 1:300), goat anti-rabbit-Alexa Fluor 647 (Invitrogen A21245, 1:400), goat anti-mouse-Alexa Fluor 647 (Invitrogen A21236, 1:400), goat anti-mouse-CF568 (1:60).

For immunoblotting, the following antibodies and dilutions were used: mouse anti-DsRed (1:300), mouse anti-α-tubulin (Sigma T9026, 1:3000), NeutrAvidin (Thermo Scientific 31000)-Alexa Fluor 647 (1:600), chick anti-α-tubulin (Abcam 89984, 1:600), mouse anti-PERK (Santa Cruz 377400, 1:300), rat anti-GRP94 (Santa Cruz 32249, 1:600), rabbit anti-GRP78 (Invitrogen PA5-29705, 1:1000), rabbit anti-FLAG (1:1000), mouse anti-HA (Invitrogen 26183, 1:2000), rabbit anti-GFP-Alexa Fluor 647 (1:1500), goat anti-rabbit-Alexa Fluor647 (1:2000), goat anti-mouse-CF568 (1:300), goat anti-chick-Alexa Fluor 488 (1:300), goat anti-mouse IgG2b-Alexa Fluor 647 (1:300), goat anti-mouse IgG1-CF568 (1:300).

Drug treatments

Cells were transfected for 20-24 hr before the addition of the drug for the indicated time. The following chemicals were used: brefeldin A (Abcam 120299), dithiothreitol (Thermo Scientific R0861), MG132 (Tocris 1748), CB5083 (Cayman Chemical 19311), thapsigargin (Invitrogen T7459), dimethyl sulfoxide (DMSO, Sigma-Aldrich 276855), 1,6-hexanediol (Sigma-Aldrich 240117).

Live-cell fluorescence microscopy

Cells were plated in Lab-Tek II chambered coverglass (Thermo Scientific 155409) and transfected as described above. For cells transfected with HaloTag-Sec23A, 0.2 μM of JF635 HaloTag ligand (Lavis Lab) was added to the cell culture medium 1 hr before imaging. After incubation at 37°C for 30 min, the cells were rinsed with normal cell culture medium for 5 min x 6 times. Prior to imaging, 25 mM HEPES (Gibco 15630080) was added to the cell culture medium to maintain the pH in the ambient environment.

Live-cell fluorescence microscopy was performed on an Olympus IX73 inverted epifluorescence microscope with a water-immersion objective (Olympus, UPLSAPO60XW, NA 1.2) and a mercury lamp, or a Nikon Eclipse Ti-E inverted fluorescence microscope with an oil-immersion objective (Nikon CFI Plan Apochromat λ 100x, NA 1.45) with 488-nm, 560-nm, and 647-nm lasers modulated by an acousto-optic tunable fiber (AOTF, Gooch & Housego, 97-03151-01). Cells were imaged at 2-20 frames per second (fps) at room temperature to moderately slow down the motion of the fast-moving t-ERGIC. Concurrent multi-color imaging was achieved by modulating the AOTF to allow frame-synchronized alternating excitation at 488, 560, and 647 nm with a multi-bandpass filter cube (Semrock Di01-R405/488/561/635 and Chroma ZET405/488/561/640m).[162]

Single-particle tracking analysis

The time-sorted image sequence was imported into Fiji[305] and analyzed through the TrackMate plugin[306] with the LoG detector and the simple LAP tracker. For t-ERGICs, the vesicular bodies were tracked as single particles, and the tubules were not separately tracked. The tracked trajectories were outputted to MATLAB for plotting into scaled displacements of trajectories. The Golgi territory was manually defined.

RUSH assay and analysis

Constructs for the RUSH assay (pStr-KDEL plasmids with a co-expressed streptavidin-KDEL hook) were modified from previous work.[273] Cells were plated in 8-well Lab-Tek chambered coverglass and transfected. The cells were imaged in the cell culture medium with 25 mM HEPES on the abovementioned Nikon Ti-E microscope. 80 μM D-biotin (J&K Scientific 322564) was added to the imaging medium to release the cargo. For quantification of the ER-to-Golgi transport kinetics, images were acquired every 5 min for ~10 predetermined positions using Micro-Manager. For high temporal resolution imaging, images were acquired continuously at 2-20 fps.

To analyze the ER-to-Golgi trafficking rate, the Golgi area and the ER area were manually defined in the image before biotin addition using Fiji. The background-subtracted intensities in the two regions were plotted as a function of time and normalized to the initial values. Golgi peak time was defined as the time corresponding to the highest intensity in the Golgi region. ER intensity decay $t_{0.75}$ was defined as the time when the ER intensity dropped to 0.75 of the initial value. For the very slow ER intensity decay of EPV-DsRed2-ER-5 samples, extrapolation was used to estimate the $t_{0.75}$.

Cell fixation, immunolabeling, and epifluorescence microscopy

Cells were plated in Lab-Tek II chambered coverglass or on 12-mm #1.5 coverslips in 24-well plates (Corning 3526) and transfected as described above. Cells were fixed with 3% paraformaldehyde (Electron Microscopy Sciences 15714) with 0.02%-0.1% glutaraldehyde (GA, Electron Microscopy Sciences 16720) in DPBS (Corning 21-030-CV) for 30 min at room temperature. We found that the t-ERGIC morphology was best preserved in the presence of GA, yet a high concentration of GA impeded epitope immunolabeling, especially for antibodies against β-COP and Rab1A. The sample was then reduced with 0.1% $NaBH_4$ (Sigma-Aldrich 213462) in DPBS for 5 min, and rinsed with DPBS for 10 min x 3 times.

For immunolabeling, the cells were blocked with the blocking buffer (3% bovine serum albumin [BSA, Sigma-Aldrich A3059] and 0.1% saponin [Sigma-Aldrich S4521] dissolved in DPBS) for 1 hr at room temperature. Primary antibodies were diluted in the blocking buffer at the abovementioned ratios. Cells were incubated with the primary antibodies for 1 hr at room temperature or overnight at 4°C. Cells were then rinsed with the washing buffer (0.1x blocking buffer diluted in DPBS) for 10 min x 3 times before incubation with the secondary antibodies diluted in the blocking buffer for 1 hr at room temperature. After the secondary labeling, cells were rinsed with the washing buffer for 10 min x 3 times and finally with DPBS for 10 min.

Conventional epifluorescence microscopy was performed in DPBS on the same setups for live-cell fluorescence microscopy.

STORM super-resolution microscopy

STORM experiments were conducted as previously described.[25,307] Briefly, the sample was immersed in a photoswitching buffer (5% D-(+)-glucose [Sigma-Aldrich G7528], 100 mM cysteamine [TCI A0648], 0.8 mg/mL glucose oxidase [Sigma-Aldrich G2133], and 40 μg/mL catalase [Sigma-Aldrich C30] in 100 mM Tris-HCl pH 7.5 [Corning 46-030-CM]) and mounted on a custom-built STORM microscope with a cylindrical lens for 3D-STORM.[125] Single-molecule images were collected at 110 fps for 50,000-80,000 frames for the construction of each super-resolution image. For dual-color STORM, Alexa Fluor 647 and CF568 were sequentially imaged as described above with the 647-nm laser and the 560-nm laser, respectively.

ERES size measurement

STORM single-molecule coordinates of each Sec31A cluster were plotted in the imaging plane, whose long and short axes were defined by a principal direction algorithm as described.[162] Distributions along the long axis and the short axis were respectively fitted by Gaussian curves. The average of the FWHMs of the two Gaussians was taken as the estimated size of the ERES.

Flow cytometry

Flow cytometry was carried out on an Attune NxT flow cytometer (Thermo Fisher) per the manufacturer's protocols. Transfected cells were trypsinized, neutralized with DMEM, and transferred to a 1.7 mL microcentrifuge tube. ~50,000 cells were analyzed. At 30%-60% transfection efficiency, non-transfected cells in the sample were thresholded by the fluorescence signal and not shown in the graphs.

Protein gel electrophoresis, Coomassie Blue staining, and immunoblotting

Cells were plated and transfected in 12-well plates. 20-24 hr after transfection, the cell culture medium was centrifuged at 2,000 g for 2 min and collected for the analysis of secreted proteins (see Immunoprecipitation [IP] and Co-IP below). Cells on the surface of the plate were then lysed in the Triton lysis buffer (1% TritonX-100 [Sigma-Aldrich T8787], 137 mM NaCl [Sigma-Aldrich S9888], 50 mM Tris-HCl pH 7.5, 1x protease inhibitor cocktail [Thermo Scientific 87786], and 1x phosphatase inhibitor cocktail [Sigma-Aldrich P0044] in water) for 30 min on ice. The lysate was then centrifuged at 16,000 g for 15 min at 4°C. The supernatant was added to 1x LDS sample buffer (Invitrogen NP0007) with 300 mM DTT and incubated for 10 min at 75°C.

Samples were run in NuPAGE Bis-Tris gels (4%-12% [Invitrogen NP0321] for small volumes of samples, 10% [Invitrogen NP0315] for larger amounts) in 1x MOPS SDS running buffer (Invitrogen NP0001) at 90 V for 1-2 hr.

For Coomassie Blue staining, the gel was rinsed in water for 5 min, incubated with 50 mL Bio-Safe Coomassie Blue Stain (Bio-Rad 1610786) for 2 hr, and rinsed with water for 30 min x 3 times.

For immunoblotting, the sample in the gel was transferred to a low-fluorescence PVDF membrane (Thermo Scientific 22860) in the transfer buffer (25 mM Tris base [Acros Organics 42457-1000], 192 mM glycine [Sigma-Aldrich G8898], and 10% v/v methanol [VWR BDH1135] in water) at 18 V for 50-70 min at room temperature using the Mini Gel system (Invitrogen NW2000). The membrane was blocked in the blocking buffer of 5% BSA in TBST (137 mM NaCl, 2.7 mM KCl [Sigma-Aldrich P9541], 19 mM Tris-HCl pH 7.5, and 0.1% v/v Tween 20 [Sigma-Aldrich P7949] in water) for 1 hr at room temperature. Primary and dye-conjugated secondary antibodies were

diluted in the blocking buffer and incubated with the membrane for 1 hr each. After each round of labeling, the membrane was washed in TBST for 10 min x 3 times. A laboratory rocker (Bellco Biotechnology 7740-10010) was used for all steps. The fluorescently labeled membrane was imaged by the Typhoon FLA 9500 scanner (GE Healthcare Life Sciences) per the manufacturer's protocol.

Pulse-chase assay

Azidohomoalanine-based pulse-chase assay was performed according to a previous protocol.[308] Cells were plated and transfected in 6-cm dishes (Falcon 353004). Pulse-chase was performed by incubating the cells in methionine/cysteine/glutamine-free DMEM (Gibco 21013024) with 10% dialyzed FBS (Gibco A3382001), 1x GlutaMax, 0.2 mM L-cysteine (Alfa Aesar J63745), and 50 μM L-azidohomoalanine (AHA, Click Chemistry Tools 1066) for 1 hr at 37°C. The medium was then replaced by the normal cell culture medium supplemented with 2 mM L-methionine (Alfa Aesar J61904) for 0-3 hr at 37°C for the chase. The cells were then lysed in the sodium dodecyl sulfate (SDS) lysis buffer (1% SDS [Sigma L6026], 100 mM Tris-HCl pH 8.0 [Corning 46-031-CM] and 1x protease inhibitor cocktail in water) for 30 min at 4°C, and then centrifuged at 16,000 g for 15 min at 4°C.

Labeling of the incorporated AHA by biotin-alkyne (Click Chemistry Tools 1266) was conducted using the Click-&-Go Protein Reaction Buffer Kit (Click Chemistry Tools 1262) according to the manufacturer's protocol. The reacted mixture was dialyzed in PBST buffer (DPBS with 0.05% v/v Tween 20) by a centrifugal filter with a 3 KDa molecular weight cut-off (Millipore UFC500324). The supernatant was immunoprecipitated by custom-made anti-RFP-beads (see Immunoprecipitation [IP] and Co-IP below). Biotinylated proteins were detected by western blotting using NeutrAvidin-Alexa Fluor 647.

Immunoprecipitation (IP) and co-IP

IP was used to enrich target proteins from the cell culture medium and pulse-chased samples. For anti-FLAG IP of the secreted APV/EPV-FLAG-DsRed2-ER-5, 10-20 μL rat anti-FLAG magnetic beads (Thermo Scientific A36797) were added to 1 mL of the centrifuged cell culture medium (above). For anti-DsRed IP of the AHA pulse-chased samples (above), rabbit anti-RFP magnetic beads were prepared by conjugating 5 μg rabbit anti-RFP antibody (Rockland 600-401-379) to 50 μL Protein G magnetic beads (Invitrogen 10003D) according to the manufacturer's protocol, and 20-50 μL conjugated beads was used for IP.

Co-IP was performed for cell lysates from 10-cm dishes (Corning 430167). Cells were lysed in the digitonin lysis buffer (1% digitonin [Sigma-Aldrich D141], 137 mM NaCl, 10% w/v glycerol [Alfa Aesar 38988], and 1x protease inhibitor cocktail in water) with pH controlled at 7.0 (for co-IP of APV/EPV-FLAG-DsRed2-ER-5 and SURF4-HA, 17 mM Na_2HPO_4 [Macron Fine Chemicals 7917-04], 13 mM NaH_2PO_4 [Fisher Chemical S369]) or 6.5 (for co-IP with KDELR3-HA, 18 mM Na_2HPO_4, 32 mM NaH_2PO_4) for 30 min at 4°C. The lysate was centrifuged at 16,000 g for 20 min at 4°C, and the supernatant was diluted 2x with 200 mM NaCl with 1x protease inhibitor cocktail for co-IP. The rat anti-FLAG magnetic beads and the mouse anti-HA magnetic beads (Thermo Scientific 88836) were used for co-IP.

The sample-loaded beads in 1.7 mL tubes were incubated on a tube rotator (VWR 10136-084) for

3 hr at 4°C. The beads were then washed in the washing buffer (corresponding lysis buffer without digitonin and glycerol supplemented with 0.03% v/v Tween 20) on ice for 5 min x 3 times. The IP-ed proteins were eluted by 20 μL 1.5x LDS sample buffer diluted in the washing buffer for 10 min x 2 times at 80°C, with intermittent vortex mixing.

RNA interference

Silencer Select siRNA against SURF4 was purchased from Thermo Fisher Scientific (Ambion 4427037-s13651). Scrambled Silencer Select control siRNA (GUACCAAUUCGUAAGUGUUT T; AACACUUACGAAUUGGUACTT) was synthesized by Thermo Fisher Scientific. Cells were plated in 6-well plates (Corning 3516). siRNA transfection was conducted using Lipofectamine RNAiMAX (Invitrogen 13778) per manufacturer's protocol. Cells were replated on day 3 to ~70% confluency and transfected with plasmids using Lipofectamine 3000 on day 4.

RT-PCR Assay

siRNA-transfected cells were harvested on Day 5 by trypsinization. Total RNA was extracted with the RNeasy Mini kit (QIAGEN 74104). Reverse transcription was performed using the GoScript Reverse Transcription Kit (Promega A50001) per manufacturer's protocol. 20 ng cDNA was used for PCR amplification with the iProof High-Fidelity PCR Kit (Bio-Rad 1725330) for 24 cycles. The PCR product was analyzed in 1.5% agarose (Lonza 50002) gel stained by SYBR Safe (Invitrogen S33102) and imaged by the Typhoon TLA 9500 scanner.

Primers used for PCR were: SURF4 (5': CTGCTCCTAGCAGAATCCC; 3': TGCATGGGCTT GTAGACTG); GAPDH (5': CATCACCATCTTCCAGGAGC; 3': GGATGATGTTCTGGAGA GCC).

Dual-color FRAP and analysis

FRAP experiments were performed on the Nikon Ti-E setup with wide-field illumination and recording. DsRed2 signal and AcGFP1 signal were simultaneously acquired with frame-synchronized alternating excitation at 560 and 488 nm using the abovementioned AOTF-controlled illumination scheme (see Live-cell fluorescence microscopy above) at 10 fps. Identified region of interest was moved to the center of the view, and an adjustable aperture in the incident light path was closed down into a pinhole to limit illumination to a circular region of ~5 μm diameter. Photobleaching was achieved by setting the intensities of both the 560 and 488 nm laser to ~2 kW/cm^2 for 5-10 sec. The excitation intensities were then lowered to ~1 W/cm^2 to record fluorescence recovery. Intensity profiles at the phase-separated condensates were background-subtracted and analyzed in Fiji and replotted by Origin 8.5 (OriginLab).

Estimation of C-terminal linker lengths of FPs

Crystal structures of relevant FPs were identified in the Protein Data Bank (PDB). We defined the free C-terminal linker as the C-terminal tail extending from the folded core of the protein in the structure, plus the unresolved sequence of the FP and the "SG" linker in the ER-5 constructs. The number of amino acid residues was counted as the length of the C-terminal linker. PDB structures used are: 1G7K (DsRed, for DsRed2), 3WLC (GCaMP6m, for GCaMP6s), 2VZX (Dendra2, for Dendra2), 2H5Q (mCherry, for mOrange2 and mCherry), and 2Y0G (EGFP, for EGFP and mEmerald).

Quantification and statistical analysis

The sample size was not predetermined by statistical methods. Fluorescence images and immunoblots were representative of at least three biological replicates. The sample size and significance test of statistical analyses were indicated in the figure legends. The value of "n" corresponds to the number of biological replicates. A *P* value lower than 0.05 was considered statistically significant.

Concluding remarks

The work described in this dissertation encompasses diverse topics in chemistry and biology but is unified under a common theme: how to use microscopy to define and address important biological questions.

The work in Part I was primarily driven by the methodological development of f-SRM, with the initial aim of achieving multiparametric single-molecule measurements. The additional information gained by such multiparametric measurements then allows for inquiries of new, previously unasked questions. For example, SM*d*M revealed slow diffusion domains within the ER membrane, which inspired us to further ask what structures they were and how they hindered diffusion. These questions would not be proposed if without the discovery enabled by f-SRM. New techniques we developed thus define important biological questions in this sense. Furthermore, these new methods also helped answer the questions. By correlating SM*d*M with SR-SMLM, we were able to rule out lipid packing as a potential cause of the slow diffusion at ER-PM contact sites.

By contrast, in Part II, we focused more on biological questions at first, and developed new methods or utilized existing approaches to address the questions. The excitation spectrum-resolved microscopy was developed on demand of fast multiplexed imaging for tracking organelle dynamics in cells. The study of t-ERGIC originated from the observation of a peculiar tubular organelle. Various microscopy, biochemistry, and molecular biology techniques were synthesized to elucidate its functions and biogenesis mechanisms. Altogether, we see that the development of methodology and the pursuit of scientific questions are mutually dependent.

References

1. Amos, B. Lessons from the history of light microscopy. *Nat. Cell Biol.* **2**, E151–E152 (2000).
2. Lakowicz, J. R. *Principles of fluorescence spectroscopy*. (Springer Science & Business Media, 2013).
3. Lichtman, J. W. & Conchello, J.-A. Fluorescence microscopy. *Nat. Methods* **2**, 910–919 (2005).
4. Ritort, F. Single-molecule experiments in biological physics: methods and applications. *J. Phys. Condens. Matter* **18**, R531–R583 (2006).
5. Huang, B., Bates, M. & Zhuang, X. Super-resolution fluorescence microscopy. *Annu. Rev. Biochem.* **78**, 993–1016 (2009).
6. Sigal, Y. M., Zhou, R. & Zhuang, X. Visualizing and discovering cellular structures with super-resolution microscopy. *Science* **361**, 880–887 (2018).
7. Paddock, S. W. & Eliceiri, K. W. Laser scanning confocal microscopy: History, applications, and related optical sectioning techniques. *Methods Mol. Biol.* **1075**, 9–47 (2014).
8. Axelrod, D. Total internal reflection fluorescence microscopy. *Methods in Cell Biology* vol. 89 169–221 (2008).
9. Thompson, R. E., Larson, D. R. & Webb, W. W. Precise nanometer localization analysis for individual fluorescent probes. *Biophys. J.* **82**, 2775–2783 (2002).
10. von Diezmann, A., Shechtman, Y. & Moerner, W. E. Three-dimensional localization of single molecules for super-resolution imaging and single-particle tracking. *Chem. Rev.* **117**, 7244–7275 (2017).
11. Milo, R. What is the total number of protein molecules per cell volume? A call to rethink some published values. *BioEssays* **35**, 1050–1055 (2013).
12. Ambrose, W. P. & Moerner, W. E. Fluorescence spectroscopy and spectral diffusion of single impurity molecules in a crystal. *Nature* **349**, 225–227 (1991).
13. Xie, X. S. & Dunn, R. C. Probing single molecule dynamics. *Science* **265**, 361–364 (1994).
14. Schmidt, T., Schütz, G. J., Baumgartner, W., Gruber, H. J. & Schindler, H. Imaging of single molecule diffusion. *Proc. Natl. Acad. Sci. U. S. A.* **93**, 2926–2929 (1996).
15. Betzig, E. *et al.* Imaging intracellular fluorescent proteins at nanometer resolution. *Science* **313**, 1642–1645 (2006).
16. Hess, S. T., Girirajan, T. P. K. & Mason, M. D. Ultra-high resolution imaging by fluorescence photoactivation localization microscopy. *Biophys. J.* **91**, 4258–4272 (2006).
17. Rust, M. J., Bates, M. & Zhuang, X. Sub-diffraction-limit imaging by stochastic optical reconstruction microscopy (STORM). *Nat. Methods* **3**, 793–795 (2006).
18. Sharonov, A. & Hochstrasser, R. M. Wide-field subdiffraction imaging by accumulated binding of diffusing probes. *Proc. Natl. Acad. Sci. U. S. A.* **103**, 18911–18916 (2006).
19. Sauer, M. & Heilemann, M. Single-molecule localization microscopy in eukaryotes. *Chem. Rev.* **117**, 7478–7509 (2017).
20. Gustafsson, M. G. L. Surpassing the lateral resolution limit by a factor of two using structured illumination microscopy. *J. Microsc.* **198**, 82–87 (2000).
21. Hell, S. W. & Wichmann, J. Breaking the diffraction resolution limit by stimulated emission: Stimulated-emission-depletion fluorescence microscopy. *Opt. Lett.* **19**, 780–782 (1994).

22. Xu, K., Zhong, G. & Zhuang, X. Actin, spectrin, and associated proteins form a periodic cytoskeletal structure in axons. *Science* **339**, 452–456 (2013).
23. Ricci, M. A., Manzo, C., García-Parajo, M. F., Lakadamyali, M. & Cosma, M. P. Chromatin fibers are formed by heterogeneous groups of nucleosomes in vivo. *Cell* **160**, 1145–1158 (2015).
24. Bintu, B. *et al.* Super-resolution chromatin tracing reveals domains and cooperative interactions in single cells. *Science* **362**, eaau1783 (2018).
25. Hauser, M. *et al.* The spectrin-actin-based periodic cytoskeleton as a conserved nanoscale scaffold and ruler of the neural stem cell lineage. *Cell Rep.* **24**, 1512–1522 (2018).
26. Jacko, M. *et al.* Rbfox splicing factors promote neuronal maturation and axon initial segment assembly. *Neuron* **97**, 853–868 (2018).
27. Sohn, P. D. *et al.* Pathogenic tau impairs axon initial segment plasticity and excitability homeostasis. *Neuron* **104**, 458–470 (2019).
28. Pan, L., Yan, R., Li, W. & Xu, K. Super-resolution microscopy reveals the native ultrastructure of the erythrocyte cytoskeleton. *Cell Rep.* **22**, 1151–1158 (2018).
29. Theillet, F. X. *et al.* Physicochemical properties of cells and their effects on intrinsically disordered proteins (IDPs). *Chem. Rev.* **114**, 6661–6714 (2014).
30. Ernst, R., Ballweg, S. & Levental, I. Cellular mechanisms of physicochemical membrane homeostasis. *Curr. Opin. Cell Biol.* **53**, 44–51 (2018).
31. Demchenko, A. P., Mély, Y., Duportail, G. & Klymchenko, A. S. Monitoring biophysical properties of lipid membranes by environment-sensitive fluorescent probes. *Biophys. J.* **96**, 3461–3470 (2009).
32. Ueno, T. & Nagano, T. Fluorescent probes for sensing and imaging. *Nat. Methods* **8**, 642–645 (2011).
33. Klymchenko, A. S. Solvatochromic and fluorogenic dyes as environment-sensitive probes: Design and biological applications. *Acc. Chem. Res.* **50**, 366–375 (2017).
34. Davis, M. M. & Hetzer, H. B. Titrimetric and equilibrium studies using indicators related to Nile Blue A. *Anal. Chem.* **38**, 451–461 (1966).
35. Yang, Z. *et al.* Macro-/micro-environment-sensitive chemosensing and biological imaging. *Chem. Soc. Rev.* **43**, 4563–4601 (2014).
36. Yan, R., Wang, B. & Xu, K. Functional super-resolution microscopy of the cell. *Curr. Opin. Chem. Biol.* **51**, 92–97 (2019).
37. Moon, S. *et al.* Spectrally resolved, functional super-resolution microscopy reveals nanoscale compositional heterogeneity in live-cell membranes. *J. Am. Chem. Soc.* **139**, 10944–10947 (2017).
38. Yan, R., Moon, S., Kenny, S. J. & Xu, K. Spectrally resolved and functional super-resolution microscopy via ultrahigh-throughput single-molecule spectroscopy. *Acc. Chem. Res.* **51**, 697–705 (2018).
39. Jun, M. E., Roy, B. & Ahn, K. H. 'Turn-on' fluorescent sensing with 'reactive' probes. *Chem. Commun.* **47**, 7583–7601 (2011).
40. Loudet, A. & Burgess, K. BODIPY dyes and their derivatives: Syntheses and spectroscopic properties. *Chem. Rev.* **107**, 4891–4932 (2007).
41. Reichardt, C. Solvatochromic dyes as solvent polarity indicators. *Chem. Rev.* **94**, 2319–2358 (1994).
42. Dutta, A. K., Kamada, K. & Ohta, K. Spectroscopic studies of nile red in organic solvents and polymers. *J. Photochem. Photobiol. A Chem.* **93**, 57–64 (1996).

43. Guido, C. A., Mennucci, B., Jacquemin, D. & Adamo, C. Planar vs. twisted intramolecular charge transfer mechanism in Nile Red: New hints from theory. *Phys. Chem. Chem. Phys.* **12**, 8016–8023 (2010).
44. Kucherak, O. A. *et al.* Switchable Nile Red-based probe for cholesterol and lipid order at the outer leaflet of biomembranes. *J. Am. Chem. Soc.* **132**, 4907–4916 (2010).
45. Dickinson, M. E., Bearman, G., Tille, S., Lansford, R. & Fraser, S. E. Multi-spectral imaging and linear unmixing add a whole new dimension to laser scanning fluorescence microscopy. *Biotechniques* **31**, 1272–1278 (2001).
46. Garini, Y., Young, I. T. & McNamara, G. Spectral imaging: Principles and applications. *Cytom. Part A* **69**, 735–747 (2006).
47. Hagen, N. & Kudenov, M. W. Review of snapshot spectral imaging technologies. *Opt. Eng.* **52**, 090901 (2013).
48. Lee, M. H., Kim, J. S. & Sessler, J. L. Small molecule-based ratiometric fluorescence probes for cations, anions, and biomolecules. *Chem. Soc. Rev.* **44**, 4185–4191 (2015).
49. Lakowicz, J. R., Szmacinski, H., Nowaczyk, K., Berndt, K. W. & Johnson, M. Fluorescence lifetime imaging. *Anal. Biochem.* **202**, 316–330 (1992).
50. Berezin, M. Y. & Achilefu, S. Fluorescence lifetime measurements and biological imaging. *Chem. Rev.* **110**, 2641–2684 (2010).
51. Perrin, J. Mouvement brownien et réalité moléculaire. *Ann. Chim. Phys.* (1909).
52. Gradinaru, C. C., Marushchak, D. O., Samim, M. & Krull, U. J. Fluorescence anisotropy: From single molecules to live cells. *Analyst* **135**, 452–459 (2010).
53. Jameson, D. M. & Ross, J. A. Fluorescence polarization/anisotropy in diagnostics and imaging. *Chem. Rev.* **110**, 2685–2708 (2010).
54. van de Linde, S. & Sauer, M. How to switch a fluorophore: From undesired blinking to controlled photoswitching. *Chem. Soc. Rev.* **43**, 1076–1087 (2014).
55. Li, H. & Vaughan, J. C. Switchable fluorophores for single-molecule localization microscopy. *Chem. Rev.* **118**, 9412–9454 (2018).
56. Dempsey, G. T., Vaughan, J. C., Chen, K. H., Bates, M. & Zhuang, X. Evaluation of fluorophores for optimal performance in localization-based super-resolution imaging. *Nat. Methods* **8**, 1027–1036 (2011).
57. Gao, F., Mei, E., Lim, M. & Hochstrasser, R. M. Probing lipid vesicles by bimolecular association and dissociation trajectories of single molecules. *J. Am. Chem. Soc.* **128**, 4814–4822 (2006).
58. Zhao, Y., Pal, K., Tu, Y. & Wang, X. Cellular force nanoscopy with 50 nm resolution based on integrin molecular tension imaging and localization. *J. Am. Chem. Soc.* **142**, 6930–6934 (2020).
59. Brockman, J. M. *et al.* Live-cell super-resolved PAINT imaging of piconewton cellular traction forces. *Nat. Methods* **17**, 1018–1024 (2020).
60. Zhang, Z., Kenny, S. J., Hauser, M., Li, W. & Xu, K. Ultrahigh-throughput single-molecule spectroscopy and spectrally resolved super-resolution microscopy. *Nat. Methods* **12**, 935–938 (2015).
61. Dong, B. *et al.* Super-resolution spectroscopic microscopy via photon localization. *Nat. Commun.* **7**, 12290 (2016).
62. Mlodzianoski, M. J., Curthoys, N. M., Gunewardene, M. S., Carter, S. & Hess, S. T. Super-resolution imaging of molecular emission spectra and single molecule spectral fluctuations. *PLoS One* **11**, e0147506 (2016).

63. Granzow, N. Supercontinuum white light lasers: A review on technology and applications. *Photonics Educ. Meas. Sci. 2019* **11144**, 1114408 (2019).
64. Oleksiievets, N. *et al.* Wide-field fluorescence lifetime imaging of single molecules. *J. Phys. Chem. A* **124**, 3494–3500 (2020).
65. Bowman, A. J., Klopfer, B. B., Juffmann, T. & Kasevich, M. A. Electro-optic imaging enables efficient wide-field fluorescence lifetime microscopy. *Nat. Commun.* **10**, 4561 (2019).
66. Long, F., Zeng, S. & Huang, Z.-L. Localization-based super-resolution microscopy with an sCMOS camera Part II: Experimental methodology for comparing sCMOS with EMCCD cameras. *Opt. Express* **20**, 17741–17759 (2012).
67. Ma, Y., Lee, Y., Best-Popescu, C. & Gao, L. High-speed compressed-sensing fluorescence lifetime imaging microscopy of live cells. *Proc. Natl. Acad. Sci. U. S. A.* **118**, e2004176118 (2021).
68. Bowman, A. J. & Kasevich, M. A. Resonant electro-optic imaging for microscopy at nanosecond resolution. *arXiv* 2104.11313 (2021).
69. Harms, G. S., Sonnleitner, M., Schütz, G. J., Gruber, H. J. & Schmidt, T. Single-molecule anisotropy imaging. *Biophys. J.* **77**, 2864–2870 (1999).
70. Kabbani, A. M. & Kelly, C. V. The detection of nanoscale membrane bending with polarized localization microscopy. *Biophys. J.* **113**, 1782–1794 (2017).
71. Lu, J., Mazidi, H., Ding, T., Zhang, O. & Lew, M. D. Single-molecule 3D orientation imaging reveals nanoscale compositional heterogeneity in lipid membranes. *Angew. Chemie Int. Ed.* **59**, 17572–17579 (2020).
72. Elf, J., Li, G. W. & Xie, X. S. Probing transcription factor dynamics at the single-molecule level in a living cell. *Science* **316**, 1191–1194 (2007).
73. Xiang, L., Chen, K., Yan, R., Li, W. & Xu, K. Single-molecule displacement mapping unveils nanoscale heterogeneities in intracellular diffusivity. *Nat. Methods* **17**, 524–530 (2020).
74. Xie, X. S. & Trautman, J. K. Optical studies of single molecules at room temperature. *Annu. Rev. Phys. Chem.* **49**, 441–480 (1998).
75. Moerner, W. E. & Orrit, M. Illuminating single molecules in condensed matter. *Science* **283**, 1670–1676 (1999).
76. Joo, C., Balci, H., Ishitsuka, Y., Buranachai, C. & Ha, T. Advances in single-molecule fluorescence methods for molecular biology. *Annu. Rev. Biochem.* **77**, 51–76 (2008).
77. Cordes, T. & Blum, S. A. Opportunities and challenges in single-molecule and single-particle fluorescence microscopy for mechanistic studies of chemical reactions. *Nat. Chem.* **5**, 993–999 (2013).
78. Yildiz, A. *et al.* Myosin V walks hand-over-hand: Single fluorophore imaging with 1.5-nm localization. *Science* **300**, 2061–2065 (2003).
79. Chen, T. *et al.* Optical super-resolution imaging of surface reactions. *Chem. Rev.* **117**, 7510–7537 (2017).
80. Chen, P. *et al.* Spatiotemporal catalytic dynamics within single nanocatalysts revealed by single-molecule microscopy. *Chem. Soc. Rev.* **43**, 1107–1117 (2014).
81. Brasselet, S. & Moerner, W. E. Fluorescence behavior of single-molecule pH-sensors. *Single Mol.* **1**, 17–23 (2000).
82. Tinnefeld, P., Herte, D. P. & Sauer, M. Photophysical dynamics of single molecules studied by Spectrally-resolved Flourescence Lifetime Imaging Microscopy (SFLIM). *J.*

Phys. Chem. A **105**, 7989–8003 (2001).
83. Bossi, M. *et al.* Multicolor far-field fluorescence nanoscopy through isolated detection of distinct molecular species. *Nano Lett.* **8**, 2463–2468 (2008).
84. Testa, I. *et al.* Multicolor fluorescence nanoscopy in fixed and living cells by exciting conventional fluorophores with a single wavelength. *Biophys. J.* **99**, 2686–2694 (2010).
85. Gunewardene, M. S. *et al.* Superresolution imaging of multiple fluorescent proteins with highly overlapping emission spectra in living cells. *Biophys. J.* **101**, 1522–1528 (2011).
86. Trautman, J. K., MacKlin, J. J., Brus, L. E. & Betzig, E. Near-field spectroscopy of single molecules at room temperature. *Nature* **369**, 40–42 (1994).
87. Macklin, J. J., Trautman, J. K., Harris, T. D. & Brus, L. E. Imaging and time-resolved spectroscopy of single molecules at an interface. *Science* **272**, 255–258 (1996).
88. Lu, H. P. & Xie, X. S. Single-molecule spectral fluctuations at room temperature. *Nature* **385**, 143–146 (1997).
89. Moerner, W. E. & Fromm, D. P. Methods of single-molecule fluorescence spectroscopy and microscopy. *Rev. Sci. Instrum.* **74**, 3597–3619 (2003).
90. Luong, A. K., Gradinaru, C. C., Chandler, D. W. & Hayden, C. C. Simultaneous time- and wavelength-resolved fluorescence microscopy of single molecules. *J. Phys. Chem. B* **109**, 15691–15698 (2005).
91. Lundquist, P. M. *et al.* Parallel confocal detection of single molecules in real time. *Opt. Lett.* **33**, 1026–1028 (2008).
92. Howell, S. B. *Handbook of CCD astronomy*. vol. 5 (Cambridge University Press, 2006).
93. Ma, Y., Shortreed, M. R. & Yeung, E. S. High-throughput single-molecule spectroscopy in free solution. *Anal. Chem.* **72**, 4640–4645 (2000).
94. Wei, L. *et al.* Probing single-molecule fluorescence spectral modulation within individual hotspots with subdiffraction-limit image resolution. *Anal. Chem.* **85**, 3789–3793 (2013).
95. Bongiovanni, M. N. *et al.* Multi-dimensional super-resolution imaging enables surface hydrophobicity mapping. *Nat. Commun.* **7**, 13544 (2016).
96. Shechtman, Y., Weiss, L. E., Backer, A. S., Lee, M. Y. & Moerner, W. E. Multicolour localization microscopy by point-spread-function engineering. *Nat. Photonics* **10**, 590–594 (2016).
97. Broeken, J., Rieger, B. & Stallinga, S. Simultaneous measurement of position and color of single fluorescent emitters using diffractive optics. *Opt. Lett.* **39**, 3352–3355 (2014).
98. Smith, C., Huisman, M., Siemons, M., Grünwald, D. & Stallinga, S. Simultaneous measurement of emission color and 3D position of single molecules. *Opt. Express* **24**, 4996–5013 (2016).
99. Kim, D., Zhang, Z. & Xu, K. Spectrally resolved super-resolution microscopy unveils multipath reaction pathways of single spiropyran molecules. *J. Am. Chem. Soc.* **139**, 9447–9450 (2017).
100. Wang, Q. & Moerner, W. E. Lifetime and spectrally resolved characterization of the photodynamics of single fluorophores in solution using the anti-brownian electrokinetic trap. *J. Phys. Chem. B* **117**, 4641–4648 (2013).
101. van Meer, G., Voelker, D. R. & Feigenson, G. W. Membrane lipids: Where they are and how they behave. *Nat. Rev. Mol. Cell Biol.* **9**, 112–124 (2008).
102. Holthuis, J. C. M. & Menon, A. K. Lipid landscapes and pipelines in membrane homeostasis. *Nature* **510**, 48–57 (2014).
103. Holthuis, J. C. M. & Levine, T. P. Lipid traffic: Floppy drives and a superhighway. *Nat.*

Rev. Mol. Cell Biol. **6**, 209–220 (2005).
104. van Meer, G. & de Kroon, A. I. P. M. Lipid map of the mammalian cell. *J. Cell Sci.* **124**, 5–8 (2011).
105. Owen, D. M., Rentero, C., Magenau, A., Abu-Siniyeh, A. & Gaus, K. Quantitative imaging of membrane lipid order in cells and organisms. *Nat. Protoc.* **7**, 24–35 (2012).
106. Golfetto, O., Hinde, E. & Gratton, E. Laurdan fluorescence lifetime discriminates cholesterol content from changes in fluidity in living cell membranes. *Biophys. J.* **104**, 1238–1247 (2013).
107. Niko, Y., Didier, P., Mely, Y., Konishi, G. I. & Klymchenko, A. S. Bright and photostable push-pull pyrene dye visualizes lipid order variation between plasma and intracellular membranes. *Sci. Rep.* **6**, 18870 (2016).
108. Munro, S. Lipid rafts: Elusive or illusive? *Cell* **115**, 377–388 (2003).
109. Lingwood, D. & Simons, K. Lipid rafts as a membrane-organizing principle. *Science* **327**, 46–50 (2010).
110. Sevcsik, E. & Schütz, G. J. With or without rafts? Alternative views on cell membranes. *BioEssays* **38**, 129–139 (2016).
111. Levental, I. & Veatch, S. L. The continuing mystery of lipid rafts. *J. Mol. Biol.* **428**, 4749–4764 (2016).
112. Klotzsch, E. & Schütz, G. J. A critical survey of methods to detect plasma membrane rafts. *Philos. Trans. R. Soc. B Biol. Sci.* **368**, 20120033 (2013).
113. Klymchenko, A. S. & Kreder, R. Fluorescent probes for lipid rafts: From model membranes to living cells. *Chem. Biol.* **21**, 97–113 (2014).
114. Schäferling, M. The art of fluorescence imaging with chemical sensors. *Angew. Chemie - Int. Ed.* **51**, 3532–3554 (2012).
115. Hell, S. W. Far-field optical nanoscopy. *Science* **316**, 1153–1158 (2007).
116. Huang, B., Babcock, H. & Zhuang, X. Breaking the diffraction barrier: Super-resolution imaging of cells. *Cell* **143**, 1047–1058 (2010).
117. Patterson, G., Davidson, M., Manley, S. & Lippincott-Schwartz, J. Superresolution imaging using single-molecule localization. *Annu. Rev. Phys. Chem.* **61**, 345–367 (2010).
118. Lew, M. D. *et al.* Three-dimensional superresolution colocalization of intracellular protein superstructures and the cell surface in live Caulobacter crescentus. *Proc. Natl. Acad. Sci. U. S. A.* **108**, E1102–E1110 (2011).
119. Shim, S. H. *et al.* Super-resolution fluorescence imaging of organelles in live cells with photoswitchable membrane probes. *Proc. Natl. Acad. Sci. U. S. A.* **109**, 13978–13983 (2012).
120. Zidovetzki, R. & Levitan, I. Use of cyclodextrins to manipulate plasma membrane cholesterol content: Evidence, misconceptions and control strategies. *Biochim. Biophys. Acta - Biomembr.* **1768**, 1311–1324 (2007).
121. Van Zanten, T. S. *et al.* Direct mapping of nanoscale compositional connectivity on intact cell membranes. *Proc. Natl. Acad. Sci. U. S. A.* **107**, 15437–15442 (2010).
122. Greenspan, P. & Fowler, S. D. Spectrofluorometric studies of the lipid probe, Nile Red. *J. Lipid Res.* **26**, 781–789 (1985).
123. Honigmann, A. *et al.* Scanning STED-FCS reveals spatiotemporal heterogeneity of lipid interaction in the plasma membrane of living cells. *Nat. Commun.* **5**, 5412 (2014).
124. Sevcsik, E. *et al.* GPI-anchored proteins do not reside in ordered domains in the live cell plasma membrane. *Nat. Commun.* **6**, 6969 (2015).

125. Huang, B., Wang, W., Bates, M. & Zhuang, X. Three-dimensional super-resolution imaging by stochastic optical reconstruction microscopy. *Science* **319**, 810–813 (2008).
126. Carlini, L. & Manley, S. Live intracellular super-resolution imaging using site-specific stains. *ACS Chem. Biol.* **8**, 2643–2648 (2013).
127. Weigel, A. V., Simon, B., Tamkun, M. M. & Krapf, D. Ergodic and nonergodic processes coexist in the plasma membrane as observed by single-molecule tracking. *Proc. Natl. Acad. Sci. U. S. A.* **108**, 6438–6443 (2011).
128. Shen, H. *et al.* Single particle tracking: From theory to biophysical applications. *Chem. Rev.* **117**, 7331–7376 (2017).
129. Lippincott-Schwartz, J., Snapp, E. & Kemvorthy, A. Studying protein dynamics in living cells. *Nat. Rev. Mol. Cell Biol.* **2**, 444–456 (2001).
130. Ishikawa-Ankerhold, H. C., Ankerhold, R. & Drummen, G. P. C. Advanced fluorescence microscopy techniques-FRAP, FLIP, FLAP, FRET and FLIM. *Molecules* **17**, 4047–4132 (2012).
131. Digman, M. A. & Gratton, E. Lessons in fluctuation correlation spectroscopy. *Annu. Rev. Phys. Chem.* **62**, 645–668 (2011).
132. Ries, J. & Schwille, P. Fluorescence correlation spectroscopy. *BioEssays* **34**, 361–368 (2012).
133. Macháň, R. & Wohland, T. Recent applications of fluorescence correlation spectroscopy in live systems. *FEBS Lett.* **588**, 3571–3584 (2014).
134. Krieger, J. W. *et al.* Imaging fluorescence (cross-) correlation spectroscopy in live cells and organisms. *Nat. Protoc.* **10**, 1948–1974 (2015).
135. Enderlein, J., Gregor, I., Patra, D., Dertinger, T. & Kaupp, U. B. Performance of fluorescence correlation spectroscopy for measuring diffusion and concentration. *ChemPhysChem* **6**, 2324–2336 (2005).
136. Eggeling, C. *et al.* Direct observation of the nanoscale dynamics of membrane lipids in a living cell. *Nature* **457**, 1159–1162 (2009).
137. Sezgin, E. *et al.* Measuring nanoscale diffusion dynamics in cellular membranes with super-resolution STED–FCS. *Nat. Protoc.* **14**, 1054–1083 (2019).
138. Manley, S. *et al.* High-density mapping of single-molecule trajectories with photoactivated localization microscopy. *Nat. Methods* **5**, 155–157 (2008).
139. Chenouard, N. *et al.* Objective comparison of particle tracking methods. *Nat. Methods* **11**, 281–289 (2014).
140. Kusumi, A., Tsunoyama, T. A., Hirosawa, K. M., Kasai, R. S. & Fujiwara, T. K. Tracking single molecules at work in living cells. *Nat. Chem. Biol.* **10**, 524–532 (2014).
141. Cognet, L., Leduc, C. & Lounis, B. Advances in live-cell single-particle tracking and dynamic super-resolution imaging. *Curr. Opin. Chem. Biol.* **20**, 78–85 (2014).
142. Manzo, C. & Garcia-Parajo, M. F. A review of progress in single particle tracking: From methods to biophysical insights. *Reports Prog. Phys.* **78**, 124601 (2015).
143. Elf, J. & Barkefors, I. Single-molecule kinetics in living cells. *Annu. Rev. Biochem.* **88**, 635–659 (2019).
144. Milo, R. & Phillips, R. *Cell Biology by the Numbers*. (Garland Science, 2015).
145. English, B. P. *et al.* Single-molecule investigations of the stringent response machinery in living bacterial cells. *Proc. Natl. Acad. Sci. U. S. A.* **108**, E365–E373 (2011).
146. Zhang, M. *et al.* Rational design of true monomeric and bright photoactivatable fluorescent proteins. *Nat. Methods* **9**, 727–729 (2012).

147. Boersma, A. J., Zuhorn, I. S. & Poolman, B. A sensor for quantification of macromolecular crowding in living cells. *Nat. Methods* **12**, 227–229 (2015).
148. Swaminathan, R., Hoang, C. P. & Verkman, A. S. Photobleaching recovery and anisotropy decay of green fluorescent protein GFP-S65T in solution and cells: Cytoplasmic viscosity probed by green fluorescent protein translational and rotational diffusion. *Biophys. J.* **72**, 1900–1907 (1997).
149. Xu, K., Babcock, H. P. & Zhuang, X. Dual-objective STORM reveals three-dimensional filament organization in the actin cytoskeleton. *Nat. Methods* **9**, 185–188 (2012).
150. Seksek, O., Biwersi, J. & Verkman, A. S. Translational diffusion of macromolecule-sized solutes in cytoplasm and nucleus. *J. Cell Biol.* **138**, 131–142 (1997).
151. Boisvert, F. M., Van Koningsbruggen, S., Navascués, J. & Lamond, A. I. The multifunctional nucleolus. *Nat. Rev. Mol. Cell Biol.* **8**, 574–585 (2007).
152. Potma, E. O. *et al.* Reduced protein diffusion rate by cytoskeleton in vegetative and polarized Dictyostelium cells. *Biophys. J.* **81**, 2010–2019 (2001).
153. Baum, M., Erdel, F., Wachsmuth, M. & Rippe, K. Retrieving the intracellular topology from multi-scale protein mobility mapping in living cells. *Nat. Commun.* **5**, 4494 (2014).
154. Kuimova, M. K. *et al.* Imaging intracellular viscosity of a single cell during photoinduced cell death. *Nat. Chem.* **1**, 69–73 (2009).
155. Di Rienzo, C., Cardarelli, F., Di Luca, M., Beltram, F. & Gratton, E. Diffusion tensor analysis by two-dimensional pair correlation of fluorescence fluctuations in cells. *Biophys. J.* **111**, 841–851 (2016).
156. Bancaud, A. *et al.* Molecular crowding affects diffusion and binding of nuclear proteins in heterochromatin and reveals the fractal organization of chromatin. *EMBO J.* **28**, 3785–3798 (2009).
157. Dross, N. *et al.* Mapping eGFP oligomer mobility in living cell nuclei. *PLoS One* **4**, e5041 (2009).
158. Anderson, C. M., Georgiou, G. N., Morrison, I. E. G., Stevenson, G. V. W. & Cherry, R. J. Tracking of cell surface receptors by fluorescence digital imaging microscopy using a charge-coupled device camera. Low-density lipoprotein and influenza virus receptor mobility at 4°C. *J. Cell Sci.* **101**, 415–425 (1992).
159. Kues, T., Peters, R. & Kubitscheck, U. Visualization and tracking of single protein molecules in the cell nucleus. *Biophys. J.* **80**, 2954–2967 (2001).
160. Lin, W. C. *et al.* H-Ras forms dimers on membrane surfaces via a protein-protein interface. *Proc. Natl. Acad. Sci. U. S. A.* **111**, 2996–3001 (2014).
161. Hansen, A. S. *et al.* Robust model-based analysis of single-particle tracking experiments with spot-on. *Elife* **7**, e33125 (2018).
162. Yan, R., Chen, K. & Xu, K. Probing nanoscale diffusional heterogeneities in cellular membranes through multidimensional single-molecule and super-resolution microscopy. *J. Am. Chem. Soc.* **142**, 18866–18873 (2020).
163. Hughes, L. D., Rawle, R. J. & Boxer, S. G. Choose your label wisely: Water-soluble fluorophores often interact with lipid bilayers. *PLoS One* **9**, e87649 (2014).
164. Nishimura, S. Y. *et al.* Diffusion of lipid-like single-molecule fluorophores in the cell membrane. *J. Phys. Chem. B* **110**, 8151–8157 (2006).
165. Brouwer, A. M. Standards for photoluminescence quantum yield measurements in solution (IUPAC technical report). *Pure Appl. Chem.* **83**, 2213–2228 (2011).
166. Cser, A., Nagy, K. & Biczók, L. Fluorescence lifetime of Nile Red as a probe for the

hydrogen bonding strength with its microenvironment. *Chem. Phys. Lett.* **360**, 473–478 (2002).
167. Danylchuk, D. I., Moon, S., Xu, K. & Klymchenko, A. S. Switchable solvatochromic probes for live-cell super-resolution imaging of plasma membrane organization. *Angew. Chemie - Int. Ed.* **58**, 14920–14924 (2019).
168. Cooper, R. A. Influence of increased membrane cholesterol on membrane fluidity and cell function in human red blood cells. *J. Supramol. Cell. Biochem.* **8**, 413–430 (1978).
169. Johnson, M. E. *et al.* Lateral diffusion of small compounds in human stratum corneum and model lipid bilayer systems. *Biophys. J.* **71**, 2656–2668 (1996).
170. Korlach, J., Schwille, P., Webb, W. W. & Feigenson, G. W. Characterization of lipid bilayer phases by confocal microscopy and fluorescence correlation spectroscopy. *Proc. Natl. Acad. Sci. U. S. A.* **96**, 8461–8466 (1999).
171. Goodwin, J. S., Drake, K. R., Remmert, C. L. & Kenworthy, A. K. Ras diffusion is sensitive to plasma membrane viscosity. *Biophys. J.* **89**, 1398–1410 (2005).
172. Saheki, Y. & De Camilli, P. Endoplasmic reticulum-plasma membrane contact sites. *Annu. Rev. Biochem.* **86**, 659–681 (2017).
173. Wu, H., Carvalho, P. & Voeltz, G. K. Here, there, and everywhere: The importance of ER membrane contact sites. *Science* **361**, eaan5835 (2018).
174. Chen, Y. J., Quintanilla, C. G. & Liou, J. Recent insights into mammalian ER–PM junctions. *Curr. Opin. Cell Biol.* **57**, 99–105 (2019).
175. Besprozvannaya, M. *et al.* GRAM domain proteins specialize functionally distinct ER-PM contact sites in human cells. *Elife* **7**, e31019 (2018).
176. Fernández-Busnadiego, R., Saheki, Y. & De Camilli, P. Three-dimensional architecture of extended synaptotagmin-mediated endoplasmic reticulum-plasma membrane contact sites. *Proc. Natl. Acad. Sci. U. S. A.* **112**, E2004–E2013 (2015).
177. Wu, Y. *et al.* Contacts between the endoplasmic reticulum and other membranes in neurons. *Proc. Natl. Acad. Sci. U. S. A.* **114**, E4859–E4867 (2017).
178. Ramadurai, S. *et al.* Lateral diffusion of membrane proteins. *J. Am. Chem. Soc.* **131**, 12650–12656 (2009).
179. Frick, M., Schmidt, K. & Nichols, B. J. Modulation of lateral diffusion in the plasma membrane by protein density. *Curr. Biol.* **17**, 462–467 (2007).
180. Goose, J. E. & Sansom, M. S. P. Reduced lateral mobility of lipids and proteins in crowded membranes. *PLoS Comput. Biol.* **9**, e1003033 (2013).
181. Guigas, G. & Weiss, M. Effects of protein crowding on membrane systems. *Biochim. Biophys. Acta - Biomembr.* **1858**, 2441–2450 (2016).
182. National Research Council. *Visualizing Chemistry: The progress and promise of advanced chemical imaging*. (National Academies Press, 2006).
183. Chan, J., Dodani, S. C. & Chang, C. J. Reaction-based small-molecule fluorescent probes for chemoselective bioimaging. *Nat. Chem.* **4**, 973–984 (2012).
184. Li, X., Gao, X., Shi, W. & Ma, H. Design strategies for water-soluble small molecular chromogenic and fluorogenic probes. *Chem. Rev.* **114**, 590–659 (2014).
185. Mishina, N. M. *et al.* Live-cell STED microscopy with genetically encoded biosensor. *Nano Lett.* **15**, 2928–2932 (2015).
186. Mo, G. C. H. *et al.* Genetically encoded biosensors for visualizing live-cell biochemical activity at super-resolution. *Nat. Methods* **14**, 427–434 (2017).
187. Lesoine, M. D., Bose, S., Petrich, J. W. & Smith, E. A. Supercontinuum stimulated

emission depletion fluorescence lifetime imaging. *J. Phys. Chem. B* **116**, 7821–7826 (2012).
188. Auksorius, E. *et al.* Stimulated emission depletion microscopy with a supercontinuum source and fluorescence lifetime imaging. *Opt. Lett.* **33**, 113–115 (2008).
189. Bückers, J., Wildanger, D., Vicidomini, G., Kastrup, L. & Hell, S. W. Simultaneous multi-lifetime multi-color STED imaging for colocalization analyses. *Opt. Express* **19**, 3130–3143 (2011).
190. Niehörster, T. *et al.* Multi-target spectrally resolved fluorescence lifetime imaging microscopy. *Nat. Methods* **13**, 257–262 (2016).
191. Gould, T. J. *et al.* Nanoscale imaging of molecular positions and anisotropies. *Nat. Methods* **5**, 1027–1030 (2008).
192. Cruz, C. A. V. *et al.* Quantitative nanoscale imaging of orientational order in biological filaments by polarized superresolution microscopy. *Proc. Natl. Acad. Sci. U. S. A.* **113**, E820–E828 (2016).
193. Shaban, H. A., Valades-Cruz, C. A., Savatier, J. & Brasselet, S. Polarized super-resolution structural imaging inside amyloid fibrils using Thioflavine T. *Sci. Rep.* **7**, 12482 (2017).
194. Backer, A. S., Lee, M. Y. & Moerner, W. E. Enhanced DNA imaging using super-resolution microscopy and simultaneous single-molecule orientation measurements. *Optica* **3**, 659–666 (2016).
195. Sezgin, E. *et al.* Polarity-sensitive probes for superresolution stimulated emission depletion microscopy. *Biophys. J.* **113**, 1321–1330 (2017).
196. Hauser, M. *et al.* Correlative super-resolution microscopy: New dimensions and new opportunities. *Chem. Rev.* **117**, 7428–7456 (2017).
197. Wöll, D. & Flors, C. Super-resolution fluorescence imaging for materials science. *Small Methods* **1**, 1700191 (2017).
198. Pujals, S., Feiner-Gracia, N., Delcanale, P., Voets, I. & Albertazzi, L. Super-resolution microscopy as a powerful tool to study complex synthetic materials. *Nat. Rev. Chem.* **3**, 68–84 (2019).
199. Chapman, D. V., Du, H., Lee, W. Y. & Wiesner, U. B. Optical super-resolution microscopy in polymer science. *Prog. Polym. Sci.* **111**, 101312 (2020).
200. Xiang, L. *et al.* Optical characterization of surface adlayers and their compositional demixing at the nanoscale. *Nat. Commun.* **9**, 1435 (2018).
201. Roberts, T. D. *et al.* Direct correlation of single-particle motion to amorphous microstructural components of semicrystalline poly(ethylene oxide) electrolytic films. *J. Phys. Chem. Lett.* **11**, 4849–4858 (2020).
202. Dutta, C. *et al.* Imaging switchable protein interactions with an active porous polymer support. *J. Phys. Chem. B* **124**, 4412–4420 (2020).
203. Mir, M. *et al.* Single molecule imaging in live embryos using lattice light-sheet microscopy. in *Methods in Molecular Biology* vol. 1814 541–559 (Humana Press Inc., 2018).
204. Wan, Y., McDole, K. & Keller, P. J. Light-sheet microscopy and its potential for understanding developmental processes. *Annu. Rev. Cell Dev. Biol.* **35**, 655–681 (2019).
205. Parodi, V. *et al.* Nonlinear optical microscopy: From fundamentals to applications in live bioimaging. *Front. Bioeng. Biotechnol.* **8**, 585363 (2020).
206. Iyer, S., Mukherjee, S. & Kumar, M. Watching the embryo: Evolution of the microscope for the study of embryogenesis. *BioEssays* 2000238 (2021).

207. Kim, J. *et al.* Oblique-plane single-molecule localization microscopy for tissues and small intact animals. *Nat. Methods* **16**, 853–857 (2019).
208. Cutrale, F., Fraser, S. E. & Trinh, L. A. Imaging, visualization, and computation in developmental biology. *Annu. Rev. Biomed. Data Sci.* **2**, 223–251 (2019).
209. Guijas, C., Montenegro-Burke, J. R., Warth, B., Spilker, M. E. & Siuzdak, G. Metabolomics activity screening for identifying metabolites that modulate phenotype. *Nat. Biotechnol.* **36**, 316–320 (2018).
210. Oginuma, M. *et al.* Intracellular pH controls WNT downstream of glycolysis in amniote embryos. *Nature* **584**, 98–101 (2020).
211. Webb, S. E. & Miller, A. L. Calcium signalling during embryonic development. *Nat. Rev. Mol. Cell Biol.* **4**, 539–551 (2003).
212. Atsuta, Y., Tomizawa, R. R., Levin, M. & Tabin, C. J. L-type voltage-gated Ca2+ channel CaV1.2 regulates chondrogenesis during limb development. *Proc. Natl. Acad. Sci. U. S. A.* **116**, 21592–21601 (2019).
213. Nerurkar, N. L., Lee, C. H., Mahadevan, L. & Tabin, C. J. Molecular control of macroscopic forces drives formation of the vertebrate hindgut. *Nature* **565**, 480–484 (2019).
214. Huycke, T. R. *et al.* Genetic and mechanical regulation of intestinal smooth muscle development. *Cell* **179**, 90–105 (2019).
215. Hallou, A. & Brunet, T. On growth and force: Mechanical forces in development. *Development* **147**, dev187302 (2020).
216. Chen, K., Yan, R., Xiang, L. & Xu, K. Excitation spectral microscopy for highly multiplexed fluorescence imaging and quantitative biosensing. *Light Sci. Appl.* (2021) doi:10.1038/s41377-021-00536-3.
217. Peng, X., Huang, X., Du, K., Liu, H. & Chen, L. High spatiotemporal resolution and low photo-toxicity fluorescence imaging in live cells and in vivo. *Biochem. Soc. Trans.* **47**, 1635–1650 (2019).
218. Tamura, T. & Hamachi, I. Recent progress in design of protein-based fluorescent biosensors and their cellular applications. *ACS Chem. Biol.* **9**, 2708–2717 (2014).
219. Pietraszewska-Bogiel, A. & Gadella, T. W. J. FRET microscopy: From principle to routine technology in cell biology. *J. Microsc.* **241**, 111–118 (2011).
220. Greenwald, E. C., Mehta, S. & Zhang, J. Genetically encoded fluorescent biosensors illuminate the spatiotemporal regulation of signaling networks. *Chem. Rev.* **118**, 11707–11794 (2018).
221. Algar, W. R., Hildebrandt, N., Vogel, S. S. & Medintz, I. L. FRET as a biomolecular research tool — understanding its potential while avoiding pitfalls. *Nat. Methods* **16**, 815–829 (2019).
222. Zimmermann, T., Rietdorf, J. & Pepperkok, R. Spectral imaging and its applications in live cell microscopy. *FEBS Lett.* **546**, 87–92 (2003).
223. Gao, L. & Smith, R. T. Optical hyperspectral imaging in microscopy and spectroscopy - a review of data acquisition. *J. Biophotonics* **8**, 441–456 (2015).
224. Elliott, A. D. *et al.* Real-time hyperspectral fluorescence imaging of pancreatic β-cell dynamics with the image mapping spectrometer. *J. Cell Sci.* **125**, 4833–4840 (2012).
225. Wang, Y., Yang, B., Feng, S., Pessino, V. & Huang, B. Multicolor fluorescent imaging by space-constrained computational spectral imaging. *Opt. Express* **27**, 5393–5402 (2019).
226. Song, K. H., Zhang, Y., Brenner, B., Sun, C. & Zhang, H. F. Symmetrically dispersed

spectroscopic single-molecule localization microscopy. *Light Sci. Appl.* **9**, 2047–7538 (2020).
227. Gat, N. Imaging spectroscopy using tunable filters: A review. in *Wavelet Applications VII* (eds. Szu, H. H., Vetterli, M., Campbell, W. J. & Buss, J. R.) vol. 4056 50–64 (SPIE, 2000).
228. Favreau, P. *et al.* Thin-film tunable filters for hyperspectral fluorescence microscopy. *J. Biomed. Opt.* **19**, 011017 (2013).
229. Wachman, E. S., Niu, W. H. & Farkas, D. L. AOTF microscope for imaging with increased speed and spectral versatility. *Biophys. J.* **73**, 1215–1222 (1997).
230. Bei, L., Dennis, G. I., Miller, H. M., Spaine, T. W. & Carnahan, J. W. Acousto-optic tunable filters: Fundamentals and applications as applied to chemical analysis techniques. *Prog. Quantum Electron.* **28**, 67–87 (2004).
231. Frank, J. H. *et al.* A white light confocal microscope for spectrally resolved multidimensional imaging. *J. Microsc.* **227**, 203–215 (2007).
232. Owen, D. M. *et al.* Excitation-resolved hyperspectral fluorescence lifetime imaging using a UV-extended supercontinuum source. *Opt. Lett.* **32**, 3408–3410 (2007).
233. Favreau, P. F. *et al.* Excitation-scanning hyperspectral imaging microscope. *J. Biomed. Opt.* **19**, 046010 (2014).
234. Valm, A. M. *et al.* Applying systems-level spectral imaging and analysis to reveal the organelle interactome. *Nature* **546**, 162–167 (2017).
235. Lewis, S. C., Uchiyama, L. F. & Nunnari, J. ER-mitochondria contacts couple mtDNA synthesis with Mitochondrial division in human cells. *Science* **353**, aaf5549 (2016).
236. Wong, Y. C., Ysselstein, D. & Krainc, D. Mitochondria-lysosome contacts regulate mitochondrial fission via RAB7 GTP hydrolysis. *Nature* **554**, 382–386 (2018).
237. Qin, J. *et al.* ER-mitochondria contacts promote mtDNA nucleoids active transportation via mitochondrial dynamic tubulation. *Nat. Commun.* **11**, 4471 (2020).
238. Olzmann, J. A. & Carvalho, P. Dynamics and functions of lipid droplets. *Nat. Rev. Mol. Cell Biol.* **20**, 137–155 (2019).
239. Tantama, M., Hung, Y. P. & Yellen, G. Imaging intracellular pH in live cells with a genetically encoded red fluorescent protein sensor. *J. Am. Chem. Soc.* **133**, 10034–10037 (2011).
240. Rosselin, M., Santo-Domingo, J., Bermont, F., Giacomello, M. & Demaurex, N. L-OPA1 regulates mitoflash biogenesis independently from membrane fusion. *EMBO Rep.* **18**, 451–463 (2017).
241. Llopis, J., McCaffery, J. M., Miyawaki, A., Farquhar, M. G. & Tsien, R. Y. Measurement of cytosolic, mitochondrial, and Golgi pH in single living cells with green fluorescent proteins. *Proc. Natl. Acad. Sci. U. S. A.* **95**, 6803–6808 (1998).
242. Stryer, L. Fluorescence spectroscopy of proteins. *Science* **162**, 526–533 (1968).
243. Lam, A. J. *et al.* Improving FRET dynamic range with bright green and red fluorescent proteins. *Nat. Methods* **9**, 1005–1012 (2012).
244. Sukenik, S., Salam, M., Wang, Y. & Gruebele, M. In-cell titration of small solutes controls protein stability and aggregation. *J. Am. Chem. Soc.* **140**, 10497–10503 (2018).
245. Sinha, B. *et al.* Cells respond to mechanical stress by rapid disassembly of caveolae. *Cell* **144**, 402–413 (2011).
246. Hoffmann, E. K., Lambert, I. H. & Pedersen, S. F. Physiology of cell volume regulation in vertebrates. *Physiol. Rev.* **89**, 193–277 (2009).

247. Wei, L. *et al.* Super-multiplex vibrational imaging. *Nature* **544**, 465–470 (2017).
248. Power, R. M. & Huisken, J. A guide to light-sheet fluorescence microscopy for multiscale imaging. *Nat. Methods* **14**, 360–373 (2017).
249. Wu, Y. & Shroff, H. Faster, sharper, and deeper: Structured illumination microscopy for biological imaging. *Nat. Methods* **15**, 1011–1019 (2018).
250. Poudel, C. & Kaminski, C. F. Supercontinuum radiation in fluorescence microscopy and biomedical imaging applications. *J. Opt. Soc. Am. B* **36**, A139–A153 (2019).
251. Yan, R., Chen, K. & Xu, K. Tubular ERGIC (t-ERGIC): A SURF4-mediated expressway for ER-to-Golgi transport. *bioRxiv* (2021) doi:10.1101/2021.04.06.438517.
252. Lee, M. C. S., Miller, E. A., Goldberg, J., Orci, L. & Schekman, R. Bi-directional protein transport between the ER and Golgi. *Annu. Rev. Cell Dev. Biol.* **20**, 87–123 (2004).
253. Dancourt, J. & Barlowe, C. Protein sorting receptors in the early secretory pathway. *Annu. Rev. Biochem.* **79**, 777–802 (2010).
254. Gomez-Navarro, N. & Miller, E. Protein sorting at the ER-Golgi interface. *J. Cell Biol.* **215**, 769–778 (2016).
255. Barlowe, C. & Helenius, A. Cargo capture and bulk flow in the early secretory pathway. *Annu. Rev. Cell Dev. Biol.* **32**, 197–222 (2016).
256. Zanetti, G., Pahuja, K. B., Studer, S., Shim, S. & Schekman, R. COPII and the regulation of protein sorting in mammals. *Nat. Cell Biol.* **14**, 20–28 (2012).
257. Brandizzi, F. & Barlowe, C. Organization of the ER-Golgi interface for membrane traffic control. *Nat. Rev. Mol. Cell Biol.* **14**, 382–392 (2013).
258. Kurokawa, K. & Nakano, A. The ER exit sites are specialized ER zones for the transport of cargo proteins from the ER to the Golgi apparatus. *J. Biochem.* **165**, 109–114 (2019).
259. Appenzeller-Herzog, C. & Hauri, H. P. The ER-Golgi intermediate compartment (ERGIC): In search of its identity and function. *J. Cell Sci.* **119**, 2173–2183 (2006).
260. Saraste, J. & Marie, M. Intermediate compartment (IC): from pre-Golgi vacuoles to a semi-autonomous membrane system. *Histochem. Cell Biol.* **150**, 407–430 (2018).
261. Hauri, H. P. & Schweizer, A. The endoplasmic reticulum-Golgi intermediate compartment. *Curr. Opin. Cell Biol.* **4**, 600–608 (1992).
262. Schweizer, A., Fransen, J. A. M., Bachi, T., Ginsel, L. & Hauri, H. P. Identification, by a monoclonal antibody, of a 53-kD protein associated with a tubulo-vesicular compartment at the cis-side of the Golgi apparatus. *J. Cell Biol.* **107**, 1643–1653 (1988).
263. Saraste, J. & Svensson, K. Distribution of the intermediate elements operating in ER to Golgi transport. *J. Cell Sci.* **100**, 415–430 (1991).
264. Bannykh, S. I., Rowe, T. & Balch, W. E. The organization of endoplasmic reticulum export complexes. *J. Cell Biol.* **135**, 19–35 (1996).
265. Klumperman, J. *et al.* The recycling pathway of protein ERGIC-53 and dynamics of the ER-Golgi intermediate compartment. *J. Cell Sci.* **111**, 3411–3425 (1998).
266. Mironov, A. *et al.* ER-to-Golgi carriers arise through direct en bloc protrusion and multistage maturation of specialized ER exit domains. *Dev. Cell* **5**, 583–594 (2003).
267. Presley, J. F. *et al.* ER-to-Golgi transport visualized in living cells. *Nature* **389**, 81–85 (1997).
268. Blum, R., Stephens, D. J. & Schulz, I. Lumenal targeted GFP, used as a marker of soluble cargo, visualises rapid ERGIC to Golgi traffic by a tubulo-vesicular network. *J. Cell Sci.* **113**, 3151–3159 (2000).
269. Marra, P. *et al.* The GM130 and GRASP65 golgi proteins cycle through and define a

subdomain of the intermediate compartment. *Nat. Cell Biol.* **3**, 1101–1113 (2001).
270. Ben-Tekaya, H., Miura, K., Pepperkok, R. & Hauri, H.-P. Live imaging of bidirectional traffic from the ERGIC. *J. Cell Sci.* **118**, 357–367 (2005).
271. Simpson, J. C., Nilsson, T. & Pepperkok, R. Biogenesis of tubular ER-to-Golgi transport intermediates. *Mol. Biol. Cell* **17**, 723–737 (2005).
272. Shomron, O. *et al.* Uncoating of COPII from ER exit site membranes precedes cargo accumulation and membrane fission. *bioRxiv* (2019) doi:https://doi.org/10.1101/727107.
273. Boncompain, G. *et al.* Synchronization of secretory protein traffic in populations of cells. *Nat. Methods* **9**, 493–498 (2012).
274. Westrate, L. M., Hoyer, M. J., Nash, M. J. & Voeltz, G. K. Vesicular and uncoated Rab1-dependent cargo carriers facilitate ER to Golgi transport. *J. Cell Sci.* **133**, jcs239814 (2020).
275. Belden, W. J. & Barlowe, C. Role of Erv29p in collecting soluble secretory proteins into ER-derived transport vesicles. *Science* **294**, 1528–1531 (2001).
276. Mitrovic, S., Ben-Tekaya, H., Koegler, E., Gruenberg, J. & Hauri, H.-P. The cargo receptors Surf4, endoplasmic reticulum-Golgi intermediate compartment (ERGIC)-53, and p25 are required to maintain the architecture of ERGIC and Golgi. *Mol. Biol. Cell* **19**, 1976–1990 (2008).
277. Plutner, H. *et al.* Rab1b regulates vesicular transport between the endoplasmic reticulum and successive Golgi compartments. *J. Cell Biol.* **115**, 31–43 (1991).
278. Tisdale, E. J., Bourne, J. R., Khosravi-Far, R., Der, C. J. & Balch, W. E. GTP-binding mutants of Rab1 and Rab2 are potent inhibitors of vesicular transport from the endoplasmic reticulum to the golgi complex. *J. Cell Biol.* **119**, 749–761 (1992).
279. Stenmark, H. Rab GTPases as coordinators of vesicle traffic. *Nat. Rev. Mol. Cell Biol.* **10**, 513–525 (2009).
280. Sannerud, R. *et al.* Rab1 defines a novel pathway connecting the pre-Golgi intermediate compartment with the cell periphery. *Mol. Biol. Cell* **17**, 1514–1526 (2006).
281. Yin, Y. *et al.* Surf4 (Erv29p) binds amino-terminal tripeptide motifs of soluble cargo proteins with different affinities, enabling prioritization of their exit from the endoplasmic reticulum. *PLoS Biol.* **16**, e2005140 (2018).
282. Otte, S. & Barlowe, C. Sorting signals can direct receptor-mediated export of soluble proteins into COPII vesicles. *Nat. Cell Biol.* **6**, 1189–1194 (2004).
283. Casler, J. C., Papanikou, E., Barrero, J. J. & Glick, B. S. Maturation-driven transport and AP-1–dependent recycling of a secretory cargo in the Golgi. *J. Cell Biol.* **218**, 1582–1601 (2019).
284. Casler, J. C. *et al.* ESCargo: a regulatable fluorescent secretory cargo for diverse model organisms. *Mol. Biol. Cell* **31**, 2892–2903 (2020).
285. Zhao, Y. G. & Zhang, H. Phase separation in membrane biology: the interplay between membrane-bound organelles and membraneless condensates. *Dev. Cell* **55**, 30–44 (2020).
286. Kroschwald, S., Maharana, S. & Simon, A. Hexanediol: a chemical probe to investigate the material properties of membrane-less compartments. *Matters* **3**, e201702000010 (2017).
287. Munro, S. & Pelham, H. R. B. A C-terminal signal prevents secretion of luminal ER proteins. *Cell* **48**, 899–907 (1987).
288. Wilson, D. W., Lewis, M. J. & Pelham, H. R. B. pH-dependent Binding of KDEL to Its Receptor. *J. Biol. Chem.* **268**, 7465–7466 (1993).

289. Bräuer, P. *et al.* Structural basis for pH-dependent retrieval of ER proteins from the Golgi by the KDEL receptor. *Science* **363**, 1103–1107 (2019).
290. Itzhak, D. N., Tyanova, S., Cox, J. & Borner, G. H. H. Global, quantitative and dynamic mapping of protein subcellular localization. *Elife* **5**, e16950 (2016).
291. Raykhel, I. *et al.* A molecular specificity code for the three mammalian KDEL receptors. *J. Cell Biol.* **179**, 1193–1204 (2007).
292. Stephens, D. J., Lin-Marq, N., Pagano, A., Pepperkok, R. & Paccaud, J. P. COPI-coated ER-to-Golgi transport complexes segregate from COPII in close proximity to ER exit sites. *J. Cell Sci.* **113**, 2177–2185 (2000).
293. Mironov, A. A. & Beznoussenko, G. V. Models of intracellular transport: Pros and cons. *Front. Cell Dev. Biol.* **7**, 146 (2019).
294. Allan, B. B., Moyer, B. D. & Balch, W. E. Rab1 recruitment of p115 into a cis-SNARE complex: Programming budding COPII vesicles for fusion. *Science* **289**, 444–448 (2000).
295. Moyer, B. D., Allan, B. B. & Balch, W. E. Rab1 interaction with a GM130 effector complex regulates COPII vesicle cis-Golgi tethering. *Traffic* **2**, 268–276 (2001).
296. Saegusa, K., Sato, M., Morooka, N., Hara, T. & Sato, K. SFT-4/Surf4 control ER export of soluble cargo proteins and participate in ER exit site organization. *J. Cell Biol.* **217**, 2073–2085 (2018).
297. Wang, X. *et al.* Receptor-mediated ER export of lipoproteins controls lipid homeostasis in mice and humans. *Cell Metab.* **33**, 350–366 (2021).
298. Feng, Z., Chen, X., Wu, X. & Zhang, M. Formation of biological condensates via phase separation: Characteristics, analytical methods, and physiological implications. *J. Biol. Chem.* **294**, 14823–14835 (2019).
299. Stephens, D. J. Functional coupling of microtubules to membranes - implications for membrane structure and dynamics. *J. Cell Sci.* **125**, 2795–2804 (2012).
300. Malkus, P., Jiang, F. & Schekman, R. Concentrative sorting of secretory cargo proteins into COPII-coated vesicles. *J. Cell Biol.* **159**, 915–921 (2002).
301. Emmer, B. T. *et al.* The cargo receptor SURF4 promotes the efficient cellular secretion of PCSK9. *Elife* **7**, e38839 (2018).
302. Vorum, H., Hager, H., Christensen, B. M., Nielsen, S. & Honoré, B. Human calumenin localizes to the secretory pathway and is secreted to the medium. *Exp. Cell Res.* **248**, 473–481 (1999).
303. Honoré, B. The rapidly expanding CREC protein family: Members, localization, function, and role in disease. *Bioessays* **31**, 262–277 (2009).
304. Tsukumo, Y., Tsukahara, S., Saito, S., Tsuruo, T. & Tomida, A. A novel endoplasmic reticulum export signal: Proline at the +2-position from the signal peptide cleavage site. *J. Biol. Chem.* **284**, 27500–27510 (2009).
305. Schindelin, J. *et al.* Fiji: An open-source platform for biological-image analysis. *Nat. Methods* **9**, 676–682 (2012).
306. Tinevez, J.-Y. *et al.* TrackMate: An open and extensible platform for single-particle tracking. *Methods* **115**, 80–90 (2017).
307. Gorur, A. *et al.* COPII-coated membranes function as transport carriers of intracellular procollagen I. *J. Cell Biol.* **216**, 1745–1759 (2017).
308. Wang, J. *et al.* Nonradioactive quantification of autophagic protein degradation with L-azidohomoalanine labeling. *Nat. Protoc.* **12**, 279–288 (2017).